ASSIMILATION OF SURFACE WEATHER OBSERVATIONS IN COMPLEX TERRAIN

by

XINGXIU DENG

B.Sc., Nanjing Institute of Meteorology, 1989

M.Sc., Nanjing Institute of Meteorology, 1992

A THESIS SUBMITTED IN PARTIAL FULFILMENT OF THE REQUIREMENTS FOR THE DEGREE OF

DOCTOR OF PHILOSOPHY OF SCIENCE

in

THE FACULTY OF GRADUATE STUDIES

(Atmospheric Science)

THE UNIVERSITY OF BRITISH COLUMBIA

August 2005

Abstract

Present computing power allows fine-resolution numerical weather prediction models to resolve meso-gamma flows within individual valleys. Such resolution is critical for mountainous British Columbia, because the valleys contain most of the population centers, industries, and transportation routes. Accurate high-resolution forecasts depend on accurate initial fields from which to start. To this end, dense local surface weather observations should be utilized to supplement the existing coarse-resolution Eta model analysis, while keeping computational costs of data assimilation reasonable for local mesoscale modeling.

This dissertation develops a technique that allows the creation of a new anisotropic background-error correlation model for complex terrain, which horizontally spreads surface weather observations along circuitous valleys. The technique, called the mother-daughter approach, is based on first-order boundary-layer characteristics in mountainous terrain. The approach is further refined to account for land-sea anisotropy, and to treat mountain-top observations differently from valley observations. The resulting improved analysis from combining the detailed surface analysis with pseudo upper-air data from the Eta model analysis is used to initialize a high-resolution forecast model.

The mother-daughter approaches are tested and compared with two existing methods, using virtual and real observations over different domains in mountainous British Columbia. It is found that the mother-daughter approaches outperform the other methods. The coastline refinement adds value to the original mother-daughter approach in maintaining thermal contrast across coastlines.

Numerical experiments are performed to assess the impacts of assimilating surface observations in complex terrain on subsequent forecasts of near-surface parameters. Better skill in predicting near-surface potential temperature is found when surface information is spread upward throughout the whole boundary layer instead of at only one model level. Experimental results show improvement on subsequent near-surface forecasts of the variables (e.g., temperature and humidity) that are directly assimilated into the model. However, the assimilation forecast run tends to worsen the forecasts of near-surface winds, which were not assimilated. These findings are confirmed by operational runs, and only minor differences are found.

In summary, a method is devised to bring local surface weather observations in complex terrain into a high-resolution forecast model. Suggestions are made to also assimilate surface-wind data.

Table of Contents

List of Tables

List of Figures

List of Abbreviations

Abbreviation	Description
ABL	atmospheric boundary layer
ACARS	Aircraft Communications Addressing and Reporting System
ADAS	ARPS Data Assimilation System
ARPS	Advanced Regional Prediction System
AVN	Aviation
BC	British Columbia
BL	boundary layer
CAPS	Center for Analysis and Prediction of Storms
CMC	Canadian Meteorological Centre
CNRL	CN Railroad
CPRL	CP Rail
CTD	circuitous travel distance
CTRL	control
DA	data assimilation
DEM	Digital Elevation Model
EC	Environment Canada
EDAS	Eta Data Assimilation System
FA	final analysis
FG	first guess
FST	RPN Standard File
FSTG	first guess
GDAS	Global Data Assimilation System
GFS	Global Forecast System
GOES	Geostationary Operational Environmental Satellite
GP	grid point
GVRD	Greater Vancouver Regional District
HYDR	BC Hydro
IAU	incremental analysis updating
IGW	inertial-gravity waves
KF	Kalman filter
mae	mean absolute error
MC2	Mesoscale Compressible Community
MD	mother-daughter
MOF	BC Ministry of Forests

MOT	BC Ministry of Transportation
NAM	North American Mesoscale
NCEP	National Centers for Environmental Prediction
NEXRAD	NEXt-Generation Weather RADar
NWP	numerical weather prediction
NWS	National Weather Service
OI	optimal interpolation
PBL	planetary boundary layer
rmse	root-mean-square error
rmsve	root-mean-square vector error
ROI	radius of influence
RPN	Recherche en Prévision Numérique
RUC	Rapid Update Cycle
SCM	Successive Correction Method
SF	sharing factor
SFC	surface
SLP	sea-level pressure
SSM/I	Special Sensor Microwave/Imager
TIROS	Television and Infrared Observation Satellite
TKE	turbulence kinetic-energy
TOVS	TIROS-N Operational Vertical Sounder
UBC	University of British Columbia
US	United States
USA	United States of America
USGS	United States Geological Survey
UTC	Coordinated Universal Time
VAD	Velocity-azimuth display
WLAP	BC Ministry of Water Land and Air Protection
3D-Var	3-dimensional variational method
4D-Var	4-dimensional variational method

Acknowledgments

I would like to thank my supervisor Dr. Roland Stull for his guidance, encouragement, and invaluable help throughout my studies at the University of British Columbia. I would also like to thank the members of my Ph.D. committee, Dr. William Hsieh and Dr. Ian McKendry for their insightful suggestions and comments.

I am sincerely grateful to Dr. Joshua Hacker at the National Center for Atmospheric Research (NCAR) for his helpful recommendations and advice about this work.

User support for the MC2 model from Stephane Chamberland at RPN/CMC is greatly appreciated.

I would like to thank Dr. Ming Xue and Dr. Keith Brewster for kindly providing me the ARPS5.0.0 (Beta8 version) Data Assimilation System (ADAS), and patiently answering my questions about setting up the ADAS.

Thanks to everyone in Weather Forecast Research Team (WFRT) at UBC for their help and for making each day delightful, particularly Dr. Henryk Modzelewski, George Hicks II and Trina Cannon for their adept computer administration. Special thanks go to Bruce Thomson who spent a lot of time to read the earlier version of this thesis and gave detailed suggestions and comments. Stimulating discussions with John Spagnol and Yongmei Zhou helped to improve this work. Thanks to Trina Cannon for giving free English lessons. I enjoyed the English lessons with Haizhen Sun and Yongmei Zhou.

Finally, I would like to express my love and gratitude to my parents, my husband, and my daughter. Their support, encouragement and understanding kept me going throughout this work.

Support from University Graduate Fellowships is acknowledged.

Grant support came from the Canadian Natural Science and Engineering Research Council (NSERC), the BC Forest Investment Account, Environment Canada (EC & LUTE), and the Canadian Foundation for Climate and Atmospheric Science (CFCAS). Geophysical Disaster CFD Center computers were funded by the Canadian Foundation for Innovation, the BC Knowledge Development Fund, and UBC.

Co-authorship statement

Chapters 3 and 4 (published as a journal paper):

Deng, X. and R. Stull, 2005: A mesoscale analysis method for surface potential temperature in mountainous and coastal terrain. Mon. Wea. Rev., 133, 389-408.

Co-author contributions:

R. Stull - suggested a sharing-factor approach for the original mother-daughter formulation; wrote section 3 called "Topographic anisotropy and boundary layers" in that MWR paper, which coincides with subsection 3.2 (p27-30) in this dissertation; lead researcher for the project and provided funding for X. Deng.

For this manuscript, I coded and tested the original mother-daughter approach, and devised the creation of a new anisotropic background-error correlation model for use in the ADAS Bratseth scheme by applying the sharing factor and the circuitous travel distance from the mother-daughter approach. I refined the sharing-factor equation by including a land-sea factor; designed and performed all of the numerical experiments, and prepared the manuscript.

Chapters 5, 6, and 7 (submitted as a journal paper):

Deng, X. and R. Stull, 2005: Assimilating surface weather observations in complex terrain into a high-resolution numerical weather prediction model. Submitted to Mon. Wea. Rev.

Co-author contributions:

R. Stull - Lead researcher for the project and provided funding for X. Deng.

For this manuscript, I designed and performed all of the numerical experiments; incorporated the assimilation of surface data into the daily, operational forecasting system. I maintained both the regular operational runs and the parallel data-assimilation runs, and prepared the manuscript.

Chapter 1

Introduction and literature review

1.1 Brief introduction to numerical weather prediction

Numerical weather forecasts are made by computers using numerical techniques to solve the fluid-dynamic and thermodynamic equations that govern the atmospheric evolution. From the first operational numerical weather forecasts in the late 1950s, the skill of numerical weather prediction (NWP) has improved steadily. Improvements have come by using much finer numerical resolution, more accurate finite-difference or spectral numerics, improved model physics, and improved initial conditions (Kalnay 2003). The increased availability of atmospheric observations has also helped.

Increasing numerical resolution is extremely computationally expensive. The additional computing resources needed to run a model with doubled horizontal resolution increase by a factor of 2^3. The spatial resolution of NWP models is always limited by computer power. However, the resolution is crucial to the accuracy of a numerical model. Generally speaking, as the resolution increases, the spatial truncation error decreases and the accuracy of the model increases. In order to improve numerical forecasts, NWP has always pushed the limits of available computing resources.

As a result of continuously increased computer power, operational (daily, real-time) model resolution has increased over last 50 years from a horizontal grid spacing of about 400 km in the late 1950s to current ones of order 10 km. For example, the current version of the U.S. National Centers for Environmental Prediction (NCEP) Eta Model is run at a horizontal grid spacing of 12 km, and the current version of the Canadian Meteorological Centre (CMC) short-range regional model is run at 15-km grid spacing. Near future trends will be implementation of regional models with a horizontal grid spacing of order 1 to 5 km in major operational centers.

Meanwhile, real-time NWP has spread from the major operational centers to many regional mesoscale modeling groups (Mass and Kuo 1998). Most of the local mesoscale modeling groups use the NCEP Eta model or Global Forecast System (GFS) analysis as a start point, and do not have a data assimilation procedure of their own. A horizontal grid spacing of less than 10 km is currently employed among some of these groups, such as the University of British Columbia and University of Washington. High-resolution NWP forecasts are useful, such as for local users including air-quality modelers, hydrological

modelers, forest-fire fighters, etc.

Even though the improvement in overall skill of NWP forecasts due to very-high resolution modeling compared to other forecasting approaches (e.g., ensemble forecasting) is still an open question (Mass et al. 2002), there are definitely needs for very-high resolution in mountainous regions or in regions where geographically driven diurnal circulations are important. This has been demonstrated by various studies (McQueen et al. 1995; Doyle 1997; Colle and Mass 1998; Colle and Mass 2000; Rao et al. 1999; Davis et al. 1999).

Obviously, increasing only resolution is not enough to improve the model forecasts. Initial conditions, model physics for very high-resolution grids, and limited predictability also affect model skills. This study addresses the issue of initial conditions.

1.2 Overview of data assimilation

Numerical weather forecasting is an initial-value (and boundary condition) problem. To make a weather forecast, one must start with observations of the real weather. The more accurate the estimate of the current atmospheric state (initial conditions), the higher will be the skill of the NWP forecasts into the future.

Data assimilation (DA) is the sophisticated combination of a numerical model and diverse observations, possibly sampled at different times/intervals and different locations. The purpose of DA is to determine as accurately as possible the state of the atmospheric (or oceanic) flow using all the available information (Talagrand 1997). With the data-assimilation technique, the observations can also be used to improve boundary conditions and to estimate parameters in a physical parameterization scheme.

1.2.1 Types of data assimilation

Depending on whether the forecast error covariance is static or evolving, data-assimilation methods that are commonly used in meteorology can be categorized into two types: traditional and advanced.

Traditional data assimilation works in an intermittent way, and deals with observations in small batches at a given time. It usually begins with an objective analysis from all available information. An initialization step is then performed and the initialized state is used as an initial condition for the next short-term forecast. Output from the forecast are used as a first guess for the next analysis.

This type of data assimilation evolved from a purely space-interpolation method in the late 1940s, to empirical methods, and then to statistics-based approaches (Daley 1991; Kalnay 2003). In the purely space-interpolation method, a polynomial function is usually used to fit a given data set over a region of grid points. The empirical methods, including the Successive Correction Method (SCM) (such as the Cressman scheme) and the Barnes scheme, determine the relative weights for the influence of each observation on a grid point by prescribing an empirical function that decreases with the distance between the

observation and the grid point. In the statistics-based methods, the weights for observation-minus-background increments are dependent upon statistical information about the errors in the background (or first guess) and in the observations.

Optimal Interpolation (OI) (Daley 1991) is a statistical analysis method based on the least-squares estimation. The successive-correction method of Bratseth (1986) was proven to converge to the OI analysis. Let $\mathbf{x}$ represent the state vector of all grid points, and $\mathbf{y}$ represent the vector of all observations. The OI analysis $\mathbf{x}_a$ is then the background $\mathbf{x}_b$ plus a weighted difference between the observation $\mathbf{y}_o$ and the "observed first guess" $H(\mathbf{x}_b)$. The least-squares analysis equations are summarized as

$$\mathbf{x}_a = \mathbf{x}_b + \mathbf{W}(\mathbf{y}_o - H[\mathbf{x}_b]) = \mathbf{x}_b + \mathbf{W}\,\mathbf{d} \tag{1.1}$$

$$\mathbf{W} = \mathbf{B}\mathbf{H}^T(\mathbf{R} + \mathbf{H}\mathbf{B}\mathbf{H}^T)^{-1} \tag{1.2}$$

$$\mathbf{P}_a = (\mathbf{I} - \mathbf{W}\mathbf{H})\mathbf{B} \tag{1.3}$$

where $\mathbf{d}$ is the vector of observational increments or innovations, $\mathbf{B}$ and $\mathbf{R}$ are background error covariance and observational error covariance matrices, respectively. The observational operator H with its linear counterpart of $\mathbf{H}$ transforms the background into the observed first guess. The analysis increments are defined by the differences $\mathbf{x}_a - \mathbf{x}_b$.

The optimal weight matrix $\mathbf{W}$ is obtained by minimizing the analysis error covariance $\mathbf{P}_a$ using a least-squares method under the following assumptions:

- The background and observations are unbiased.
- Observation and background errors are uncorrelated with each other.
- The background is a good approximation of the true state.
- The observational operator can be linearized.

The three-dimensional variational (3D-Var) approach (Bouttier and Courtier 1999; Kalnay 2003) is the variational version of the least-squares analysis. The optimal analysis $\mathbf{x}_a$ is obtained through a variational approach by minimizing a cost function. The cost function of the analysis is defined as the distance between the state vector $\mathbf{x}$ and the background $\mathbf{x}_b$ (weighted by the inverse of the background error covariance $\mathbf{B}$) plus the distance to the observations $\mathbf{y}_o$ (weighted by the inverse of the observational error covariance $\mathbf{R}$):

$$J(\mathbf{x}) = \frac{1}{2}\left[(\mathbf{x} - \mathbf{x}_b)^T\mathbf{B}^{-1}(\mathbf{x} - \mathbf{x}_b) + (\mathbf{y}_o - H(\mathbf{x}))^T\mathbf{R}^{-1}(\mathbf{y}_o - H(\mathbf{x}))\right] \tag{1.4}$$

The 3D-Var solution, through the minimization of the cost function above, is proven to be mathematically equivalent to the OI solution through the least-squares determination of the weight matrix $\mathbf{W}$ (Bouttier and Courtier 1999; Kalnay 2003), as long as the underlying hypotheses (i.e., linearization of the observational operator and Gaussian errors with zero mean) are justified.

One advantage of 3D-Var is the ease to include balance constraints (e.g., geostrophic, hydrostatic) as an extra term in the cost function. These constraints are not appropriate for the analysis of surface observations. Another advantage of 3D-Var is the convenience to directly assimilate data sources (e.g., satellite radiances and radar reflectivities) that

are indirectly related to the model variables. The surface observations considered in this study are all directly related to the model variables; hence, 3D-Var holds no particular advantage.

In OI (Daley 1991), in the Bratseth (1986) scheme, and in 3D-Var method (Laroche et al. 1999; Kalnay 2003), the background error covariance matrix **B** is estimated only once, and is assumed to be statistically stationary. This type of data assimilation is computationally reasonable for local, real-time NWP groups.

Advanced data assimilation with evolving forecast error covariance works in a continuous (or almost continuous) way, and considers observations that are distributed in time. Variabilities in forecast errors are accounted for in this type of data assimilation, which includes the Kalman filter (KF) and four-dimensional variational (4D-Var) methods. Details about various versions of KF method and 4D-Var can be found in Bouttier and Courtier (1999) and Kalnay (2003). Summarized here are the main features of each method.

The KF and its extended version (EKF) (Kalnay 2003; Gauthier et al. 1993) for nonlinear cases consist of two steps: a forecast step and an analysis step. The algorithm in the analysis step is very similar to that in OI [see Eqs. (1.1), (1.2) and (1.3)] except for different notations and terminology. For example, the optimal weight matrix **W** is replaced by the Kalman gain **K**. The essence of the KF or EKF lies in the forecast step, in which the forecast or background error covariance is predicted by the forecast model or tangent linear forecast model, the adjoint model and the system error covariance. The forecast step also advances the forecast from each new analysis to provide a background for next analysis. The computational and storage costs of the KF or EKF are extremely expensive. Even though the forecast error covariance can be predicted explicitly in the KF or EKF, a correct specification of the system error covariance is problematic.

Ensemble Kalman filtering (EnKF) (Houtekamer and Mitchell 1998, 2001), one simplification of the EKF, avoids the estimation of the system error covariance by approximating the forecast error covariance from an ensemble of data-assimilation cycles. Each member of the ensemble data assimilation assimilates the same observations, but with different random perturbations added. More ensemble members usually lead to more statistically significant results. However, there is a trade-off between the number of ensemble members and the computational costs.

The 4D-Var (Rabier et al. 2000) is a simple but important generalization of 3D-Var, which includes the time dimension and a forecast model. The essence of 4D-Var is to minimize the difference between observations and model forecasts over a finite time period, in addition to minimizing the difference between the analysis and background at the beginning of a time interval. If the forecast model is assumed to be perfect (which is not true in reality), then it is used as a strong constraint. When the forecast model is used as a weak constraint, the system error covariance matrix has to be estimated as in KF or EKF.

This type of data assimilation is certainly the direction of the future. But at present, the computational cost for its real-time applications is well beyond what the local modeling groups can afford.

1.2.2 Error covariance

For any of the statistics-based methods, the analysis quality depends crucially on a correct specification of the observation and background error covariance [**B** and **R** in (1.2)], because **B** and **R** determine the magnitude of corrections applied to the background. The observation error variances can be obtained from instrument error estimates. If the measurements are independent, observation-error correlations can be assumed to be zero. Hence, the matrix **R** is often diagonal. This holds true for surface observations. In least-squares analysis algorithms, only the ratio of the observation to background error variances is important. The ratio determines to what degree the analysis will converge toward the observations. Comparatively, the specification of background-error correlations (standardized covariance) is most important, and yet a difficult problem.

Bouttier and Courtier (1999) detailed several reasons for the importance of background-error correlations. Two of them are summarized here: 1) in data-sparse areas, the observation information is spread out based on the spatial structure of background-error correlations; 2) in data-dense areas, background-error correlations controls the smoothing of the observed information in the presence of discrete observations.

Literature shows that there exist several ways to estimate background error covariance. The first method is the observational method (Hollingsworth and Lonnberg 1986, Mitchell et al. 1990), which is also called the innovation method. It is based on the use of innovations (the differences between the short-range forecasts and the observations). Reliable estimates can be obtained only in a dense and large observation network over a long time period under the assumption of uncorrelated observations. This method requires dense observations at each valley and mountain, if it is used in complex terrain.

The second method is to use a lagged-forecast approach [also called the National Meteorological Center (NMC) method] (Parrish and Derber 1992). This approach is achieved by first forming differences between two forecasts valid at the same time, but started from initial conditions at different times. The forecast differences are then assumed to be representative of the forecast errors. But the theoretical foundation of this approach is not clear at present (Bouttier and Courtier 1999). Complex terrain would also complicate this method, as forecast errors arise also from misrepresentation of real terrain in NWP models.

The third way is to employ candidate correlation models defined by analytic functions, such as a Gaussian function (Daley 1991). All the three methods above give stationary background-error correlations. Time- and flow-dependent structure functions can be estimated explicitly by Kalman filter (Gauthier et al. 1993), implicitly by 4D-Var methods (Thépaut et al. 1996), or approximated in the ensemble Kalman filter (EnKF) (Houtekamer and Mitchell 1998, 2001). The computational costs associated with KF, 4D-Var and EnKF are high.

Finally, as pointed out by Bouttier and Courtier (1999), " meteorological common sense can be used to specify error statistics, to the extent that they reflect our a priori knowledge of the physical processes responsible for the errors".

The background error covariances are often assumed to be isotropic in practical implementation of data assimilation (except for computationally expensive KF and 4D-Var).

Isotropy, however, is a questionable assumption for mesoscale analyses or for analyses in mountainous/coastal regions. Therefore, anisotropic covariance models are receiving increasing attention (Benjamin et al. 1991; Desroziers 1997; Purser et al. 2003; Liu and

Xue 2005; Liu et al. 2005). More anisotropic covariance models to account for terrain effects are reviewed in the next section.

1.3 The use of surface observations in complex terrain and related problems

The current global observing system supplements conventional rawinsondes and surface data with various remote sensing and in-situ measurement systems [e.g., wind profilers, improved satellite soundings, Doppler sodars, Doppler lidars, NEXRAD (Next Generation Weather Radar) Doppler radars, ASOS (Automated Surface Observing System), ACARS (Automated Commercial Aircraft Reporting System) and GPS profiles]. Meanwhile, regional surface data are available from many local agencies that deploy surface stations for their own purposes, but which are not included in the routine data assimilation performed at the national weather centers.

Among them, surface observations, being frequent and dense, are valuable data sources for mesoscale data analysis, assimilation and forecasting (Yee and Jackson 1988; Stauffer et al. (1991); Miller and Benjamin 1992; Ruggiero et al. 1996). Ruggiero et al. (2000) demonstrated that a combination of continuous assimilation of satellite image data and intermittent assimilation of hourly surface observations led to a better depiction of circulations caused by cloud-shading contrasts. It was also found that assimilating surface data into NWP models led to significant reduction in the atmospheric boundary layer (BL) modeling errors (Alapaty et al. 2001), from which subsequent air-pollution modeling may benefit considerably.

To extract as much information as we can from all available data sources is one of the challenges in data assimilation. Remotely sensed data such as from radar and satellite have greatly improved the availability and accuracy of 3-D, nearly time-continuous, mesoscale observations. There is now a growing literature on assimilating remotely sensed data into NWP models. Advances here will surely improve short-term forecasts in regions where this data is readily available and accessible.

However, in mountainous regions, satellite and radar data have inherent limitations. Radars have very limited range in complex terrain, such as in mountainous British Columbia (BC), where low-level blocking can be severe. Satellites have difficulty measuring the atmosphere below clouds, which means the BL is often not well sampled. In contrast, surface observations provide direct measurements of surface weather conditions and also allow inference of conditions aloft within the BL.

Assimilating surface observations in complex terrain into NWP models currently remains a relatively unexplored area for improving the initial conditions of NWP models. This is particularly true for mountainous British Columbia, where high-resolution NWP models are needed to resolve small-scale weather in each valley.

This dissertation focuses on assimilating surface weather observations in complex terrain into a very high-resolution NWP model, with emphasis on reducing the near-surface model prediction errors. Several problems arise from assimilating surface observations into NWP models. Problems associated with horizontal and vertical spreading of surface observations are discussed in the next subsection.

1.3.1 Horizontal spreading of surface observations

Horizontal spreading deals with horizontal interpolation of surface observations from irregularly distributed locations to uniform grids. The horizontal spreading of surface observations is often complicated by orographic influences. In BC, surface weather stations are usually located in deep valleys, while few surface stations are located at high elevations, such as at ski areas. Both surface background error covariance and representativeness of surface observations are largely affected by heterogeneous terrain. One observation might be very poorly represented by its neighboring observations, even at very short distance if they are in two different valleys that are separated by a high ridge. An isotropic assumption for the background error covariance (depending on traditional straight-line distance only) is clearly not valid in mountainous regions.

Figure 1.1 illustrates examples of interpolation problems in mountainous regions (in a terrain-following coordinate system). The first example is related to the spreading of valley observation (o1) into the grid points (e.g., B) in the same valley and into the grid points (e.g., A) with differing elevation. Even though the horizontal distance from station o1 to point A is almost the same as that from o1 to point B, the information received at A from o1 should be different from that received at B.

The second example is associated with interpolation of data from a valley (e.g., o2) and along a ridgeline (e.g., o3) that may experience different flow regimes. This means that the information received at point C should be mainly from observation o2, rather than observation o3, even though the horizontal distance from station o2 to point C equals that from station o3 to point C.

The third example is interpolation of data from two adjacent valleys that are separated by high terrain. As illustrated in Fig. 1.1, point B is located in the middle between station o1 and o2. Station o1 and point B are located in the same valley, whereas station o2 is separated from point B by a high ridge. Isotropic background error correlations would result in the same contribution to point B from both observations o1 and o2. This should not be the case, due to blocking by the high ridge (assuming high enough to exceed the BL top). The first two scenarios describe problems regarding elevation differences. The third example describes a problem of valley differences.

A simple solution that includes elevation differences in the correlation model for a 2-D surface analysis is to use a vertical Gaussian decay such as is used in 3-D analyses. One such example is the correlation function used in the Advanced Regional Prediction System (ARPS) (Xue et al. 2000) Data Assimilation System (ADAS) (Brewster 1996).

In recent years, some of the interpolation problems in mountainous regions have been tackled by incorporating terrain effects in different ways into background-error correlation (standardized covariance) model. To study Alpine lee cyclogenesis, Lanzinger and Steinacker (1990) developed an objective analysis scheme that incorporated anisotropic correlation structures due to orography. They used the observational method to derive correlation models with and without mountain barriers. A rapid decrease was observed in the correlations computed from pairs of stations across a mountain barrier. By including the topographic effects, they were able to generate more realistic analyses resolving sharp gradients across major mountain ridges.

In a quadratic horizontal interpolation scheme that was used for temperature analyses in a northern part of Yugoslavia, Vrhovec (1990) introduced a correction to the traditional

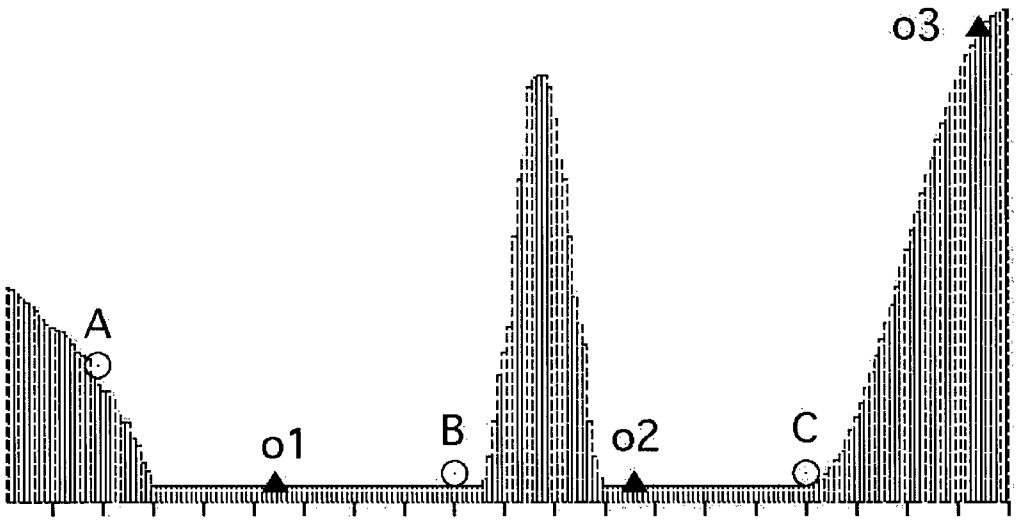

Figure 1.1: Schematic illustration of idealized topography within a 1D domain. Filled triangles indicate observation locations, whereas open circles represent analysis grid points.

straight-line distance between a weather station and an analysis grid point. The correction was based on the accumulated variation of topography between the two points, and also on the atmospheric stability. By doing so, the effective distance is increased and the correlation is reduced, if there is a mountain ridge (relative to the two-point averaged elevation height) between the two points.

Miller and Benjamin (1992) used elevation differences (between an observation station and an analysis grid point) in the correlation function for potential temperature to account for terrain effects.

Most recently (almost concurrent to this thesis work), Myrick et al. (2004) introduced in the ADAS an anisotropic term defined by a negative squared exponential function of the barrier height relative to a predefined scale height. This approach required searching for any barrier directly between each observation location and each analysis point.

Any one of these schemes indeed solved one (but not all) of the interpolation problems in complex terrain, as illustrated above. The method by Myrick et al. (2004) was able to solve the problems associated with both elevation and valley differences. But their method would not be valid when a study region has circuitous valleys, such as in mountainous BC. The topography considered in all of studies mentioned above is much less complicated than that in BC, Canada. BC has a variety of landscapes from seashores, straits, and fjords to mountains and valleys, as can be seen in the satellite image from Terra (Fig. 1.2). Some valleys are narrow and long with kinks and twists (Figs. 1.3 and 1.4). Horizontal spreading of surface observations in such complex terrain requires a new anisotropic parameterization of background-error correlations. This is one of the needs that motivated my research.

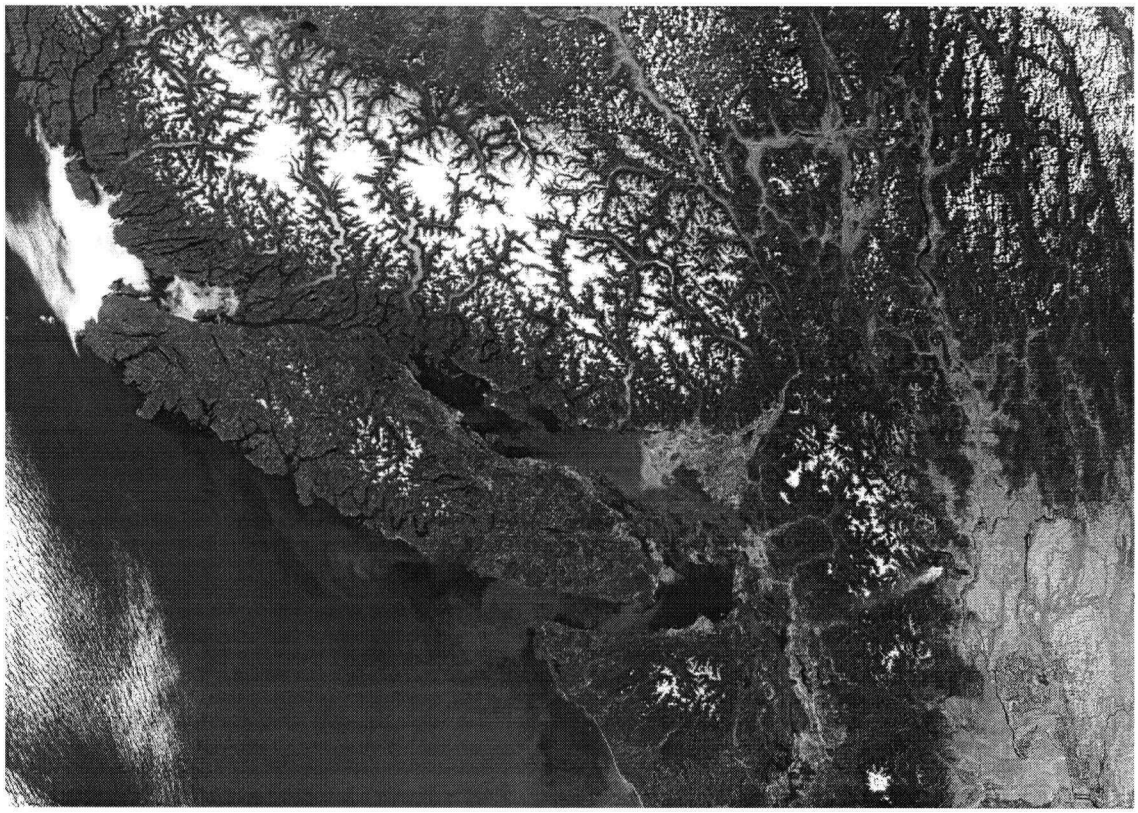

Figure 1.2: Southwestern British Columbia and northwestern Washington as viewed from the Terra satellite.

Figure 1.3: Zoomed picture of Fig. 1.2, showing the Lower Fraser Valley, Coastal Mountains, and neighboring valleys north of Vancouver.

Figure 1.4: A typical narrow valley in the Coastal Mountain Ranges north of Vancouver, as shown in an aerial photo.

1.3.2 Vertical spreading of surface observations

Effective assimilation of single-level data depends on the physically realistic vertical extent over which the data are inserted into the model. Barwell and Lorenc (1985) found that the useful information from single-level aircraft wind data tended to be lost during subsequent forecasts when the information was confined to one model level. By distributing single-level data throughout several model levels, they achieved beneficial effects on subsequent model forecasts. Surface observations are available at only one terrain-following level. Therefore, after the surface observations are analyzed, the surface analysis must be merged properly with upper-air data and/or the 3-D first-guess fields.

In a mesoscale objective analysis using the Barnes (1964) scheme, Yee and Jackson (1988) blended surface and rawinsonde observations in the BL by a simple technique. They first considered only rawinsonde observations to get a background analysis, and then analyzed both surface and rawinsonde observations at the ground level. The differences between the two analyses at ground level were treated as mesoscale signals, which were spread vertically by a linear weighting function of the distance from the ground. But the vertical extent over which the surface data influenced the background rawinsonde-scale analysis was chosen arbitrarily. Benjamin (1989) was able to vertically distribute the influence of surface observations by using a vertical correlation function of the potential temperature difference in an isentropic coordinate system.

Stauffer et al. (1991) investigated methods to best use single-level surface data by assuming that surface wind and mixing ratio observations can be applied throughout the model BL according to idealized BL behavior. Their conceptual BL model, adopted from

Garratt et al. (1982) who formulated an idealized BL model based on observations at the extremely flat locations of Minnesota and Wangara experiment, might not be appropriate for mountainous terrain. Ruggiero et al. (1996) introduced an alternative physical approach. They performed a surface analysis at the lowest-level of model. The surface analysis increments at the lowest level are then used to adjust the other model layers within the BL. This was achieved by integrating the diffusion equations for the analysis increments. However, the simple local turbulent scheme used in Ruggiero et al. (1996) was not able to adequately propagate the analysis deviations at the lowest model layer throughout the BL.

1.4 Objectives of the thesis

The Mesoscale Compressible Community (MC2) model (Benoit et al. 1997; Laprise et al. 1997) has been running daily for eight years at the University of British Columbia (UBC) since 1997. A 256-processor IBM supercomputer purchased in 2001 allows fine-resolution NWP models to almost resolve small mesoscale flows within individual valleys. Such resolution is important for mountainous BC, because in steep mountainous terrain, the valleys contain most of the population centers, industries, and transportation routes. Currently, the daily, real-time forecasts at UBC start with 108-km grid spacing, initialized from the NCEP Eta model analysis, and then one-way nest down to 36, 12, 4, and 2 km.

The two finest grids can resolve different weather conditions in separate neighboring valleys and have the potential to increase the accuracy of point forecasts. These high-resolution forecasts from UBC have been used by regional air-quality, transportation, forestry and other BC agencies. These agencies in turn help by providing a data-rich network of surface weather observations for statistical verification and potential initialization of high-resolution numerical forecasts at UBC. Recently, high-resolution weather forecasts driving air-quality models have also been tested in daily operations at UBC (Delle Monache et al. 2004a,b).

This thesis explores ways to fully utilize dense local surface weather observations, such as are available in mountainous BC, to supplement the existing coarse-resolution 3-D Eta model analysis, while keeping computational cost reasonable for local, real-time NWP forecasting. The new, improved analyses are then used to initialize the high-resolution NWP models. More specifically, the objectives of this thesis are as follows:

- Develop a new anisotropic background-error correlation model for use in horizontally spreading surface weather observations in complex terrain.
- Merge dense local surface weather observations in the form of a detailed 2-D surface-data analysis into the coarse-resolution 3-D Eta model analysis, to create more accurate initial conditions for high-resolution numerical forecasts.
- Examine the impacts of assimilating surface weather observations on subsequent numerical weather forecasts.
- Incorporate this new approach into daily operational forecasting for an independent test.

More details about the MC2 model, the objective analysis tool, and the surface observations are given in Chapter 2. Chapter 3 details the technique that allows the creation of a new anisotropic correlation model for horizontally spreading surface observations in complex terrain. The new approach is then compared with two other existing methods in Chapter 4 through case studies of surface-data analysis in mountainous and coastal terrain. Chapter 5 describes how to merge the detailed surface-data analysis into the coarse-resolution Eta model analysis, and how to initialize a high-resolution model from the resulting improved analysis. In Chapter 6, with case study examples, the new approach is further tested and compared with the other existing methods for a different domain over BC. The impacts of various data-assimilation strategies on subsequent near-surface weather forecasts are also examined. Chapter 7 contains the results from daily, near-real-time operational data-assimilation runs. This is presented as an independent test for the newly developed data-assimilation system that utilizes dense local surface observations in mountainous BC. The summary and discussions are given in Chapter 8.

Chapter 2

Experimental environment

All necessary tools and procedures for the numerical experiments are given in this chapter. This includes the numerical forecast model and domains (section 2.1), the objective analysis tool (section 2.2), surface weather observations (section 2.3) for the case studies and near-real-time operational runs, and statistical verification measures (section 2.4).

2.1 The numerical model and domains

The numerical weather prediction (NWP) model into which the surface observations are assimilated is the Mesoscale Compressible Community (MC2) model version 4.9.1. This model, originally developed by the late André Robert and his colleagues (Robert and Yakimiw 1986), is based on a fully elastic, semi-implicit, semi-Lagrangian approach (Tanguay et al. 1990). MC2 is a nonhydrostatic, primitive-equation model. The model solves the Euler equations on a limited-area Cartesian domain of the polar stereographic projection with time-dependent nesting of the lateral boundary conditions, using the strategy developed by Yakimiw and Robert (1990). An Asselin-Robert time filter (Asselin 1972) is used to control high-frequency time oscillations. This model is one-way self-nested. Namely, nesting values for the coarsest domain often consist of output data obtained from another larger-scale model such as the Eta model. Then, output data from a coarse-mesh run of the MC2 model is used as input to a subsequent run at finer resolution. The MC2 model adopts vertically stretched Gal-Chen terrain-following coordinates to obtain greater resolution close to the surface. The Gal-Chen terrain-following coordinates (Gal-Chen and Somerville 1975) are defined with the following relation:

$$\xi(X, Y, z) = \left[\frac{z - h_0(X, Y)}{H - h_0(X, Y)}\right] H \tag{2.1}$$

where z is geometric height, H is the top of the model atmosphere, ξ is the height in Gal-Chen units of length, and $h_0(X, Y)$ is the topographic height that is a function of the independent variables X and Y.

The MC2 model utilizes the evolving RPN/CMC physics package. A detailed description of the dynamical framework of MC2 is made by Laprise et al. (1997), while a thorough description of the full MC2 model is given in Benoit et al. (1997). That paper was accurate for version 4.1 of the MC2. All the experiments reported here use version 4.9.1. The essential model physics are summarized in Table 2.1.

Table 2.1: The MC2 model physical parameterization schemes

PBL based on 1.5 order TKE (Benoit et al. 1989)
Surface layer based on similarity theory
Force-restore for land surface processes (Deardorff 1978)
Fritsch/Chappel deep convection scheme (Fritsch and Chappell 1980)
Radiation schemes interactive with clouds
(Garand and Mailhot 1990; Fouquart and Bonnel 1980)
Explicit cloud water/ice prediction scheme (Sundqvist et al. 1989)

For this dissertation research, the model is configured with five one-way self-nested grids with horizontal grid spacings of 108, 36, 12, 4, and 2 or 3 km. Figure 2.1 shows the first 4 grids. The configurations of the 108, 36, 12, 4, and 2 km grids are the same as those for current daily forecasts at UBC. The NCEP Eta model analysis and forecasts from the "104" grid (described in more detail in Appendix A) are used as the initial and boundary conditions for the coarsest grid. We start from this Eta forecast because the 104-grid output extends far enough west over the Pacific to reduce upstream boundary errors, and also because this output is continuously available and accessible via Internet in a timely manner.

The 108-km and 36-km meshes have 87 X 71 and 167 X 151 grid points, respectively. These two meshes have 19 layers in the vertical, with the model top at 25 km. The 12-km mesh has 257 X 207 points and 27 layers in the vertical, with the model top at 24 km. The 4-km, 2-km and all the 3-km meshes (Figs. 2.2 and 2.3) have 35 layers (18 below 1500 m) in the vertical, with the model top at 23 km. Figure 2.4 shows the 35 vertically stretched levels for thermodynamic variables. The first "thermodynamic" level is located at 5.3 meters above the model ground, while the first "momentum" level is located at 10.6 meters. The objective analyses of surface potential temperature and specific humidity, described in later Chapters, are performed at the first thermodynamic level.

Some numerical experiments are performed on the bigger 3-km domain (Fig. 2.2). All other data-assimilation (DA) experiments are performed on the smaller 3-km domain (b) (Fig. 2.3) that is centered at Vernon, BC. Near-real-time operational DA runs are performed for the 2-km mesh in Fig. 2.2. For all DA runs on 3-km or 2-km meshes, five grid points are cut from each side of the analysis domains shown in Fig. 2.3 or Fig. 2.2, to reduce the effects of lateral boundary errors. Namely, the domain for DA runs has slightly fewer grid points than the domain for the first guess and analysis.

The 3-km domain in Fig. 2.3 differs from the one in Fig. 2.2 not only in domain locations, but also in the preparation of the initial geophysical surface fields, i.e., topography and landuse data, for historical reasons. The terrain fields for the bigger 3-km domain in Fig. 2.2 were provided and prepared by RPN/CMC using the Barnes (1964) technique. The software package to generate the geophysical fields for the MC2 model was made available by RPN/CMC to UBC, before we started to do case studies in Chapter 6. The terrain elevations for the 3-km domain (b) in Fig. 2.3 were generated by applying a three-point average to the 30-arc-second (approximately 1 km) resolution U.S. Geological Survey (USGS) digital elevation model (DEM). For all grids, terrain smoothing should be applied

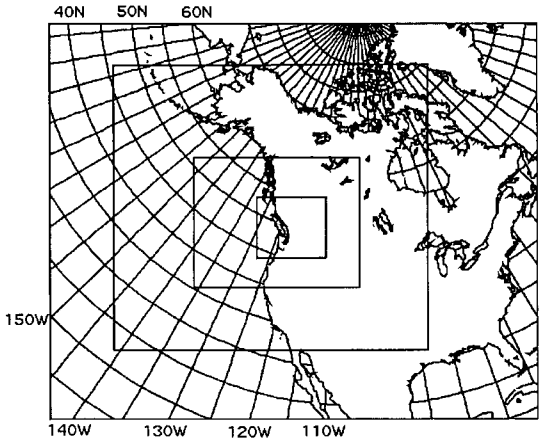

Figure 2.1: MC2 grid domains for $\Delta x = 108$, 36, 12 and 4 km.

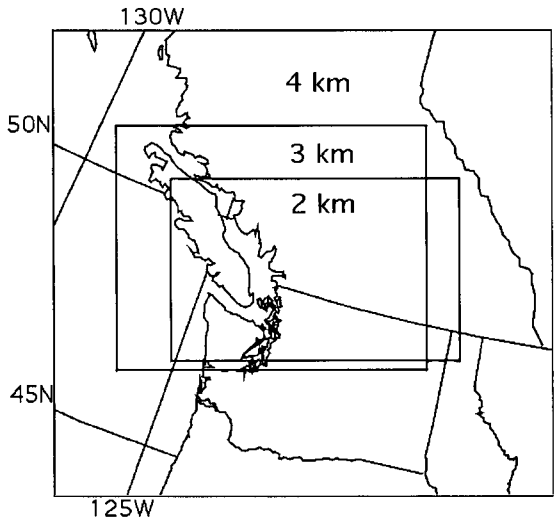

Figure 2.2: MC2 grid domains for $\Delta x = 4$, 3, and 2 km. MC2 4-km output provides nesting files to initialize 2- and 3-km runs. MC2 at 3 km is run to provide first-guess fields for analysis (Chapter 4). MC2 at 2 km is run to provide a reference atmosphere to generate virtual surface observations for analysis and verification (Chapter 4). In Chapter 7, MC2 at 2 km is run to provide first-guess fields for analysis, and also for assimilation runs after analysis. But five grid points are cut from each side of the analysis domain shown here.

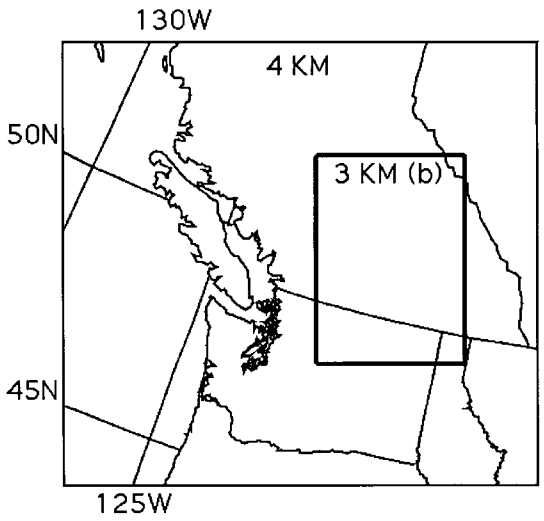

Figure 2.3: Another MC2 grid configuration for $\Delta x = 4$ and 3 km. The 3-km domain (b) is centered at Vernon, British Columbia. MC2 4-km output provides nesting files to initialize the 3-km run. MC2 at 3 km is run to provide first-guess fields for the analysis, and also for assimilation runs after analysis. But five grid points are cut from each side of the analysis domain shown here.

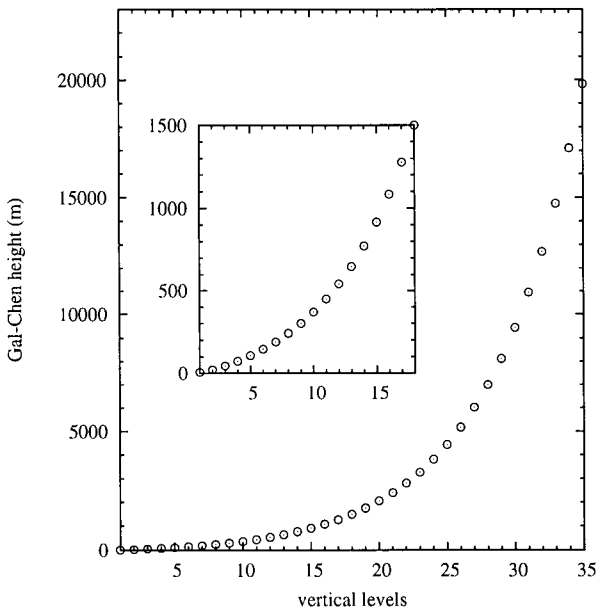

Figure 2.4: Vertical distribution of the computational levels for thermodynamic variables in the MC2 model for the grids having $\Delta x = 4$ km, 3 km and 2 km. Levels are chosen to ensure greater resolution in the bottom part of the troposphere.

to make the terrain-elevation resolution consistent with the horizontal grid spacing. The MC2 considers this modelled elevation to be the surface of the Earth, even though the modelled elevation may be locally very different from the real terrain elevation.

2.2 The objective analysis tool

The Advanced Regional Prediction System (ARPS) (Xue et al. 2000) Data Assimilation System (ADAS) (CAPS 1995, Brewster 1996) in ARPS5.0.0 Beta8 is used as an objective analysis tool. The ADAS employs the successive-correction method of Bratseth (1986), and thus requires less computational time than other advanced methods (i.e., EnKF and 4D-Var). This advantage makes it possible to perform near real-time, high-resolution analyses over most of BC, Canada, using the moderately powerful computers available at UBC.

2.2.1 General descriptions

The ADAS was developed by the Center for Analysis and Prediction of Storms (CAPS) at the University of Oklahoma. The ADAS is a 3-dimensional mesoscale analysis system that ingests and analyzes meteorological data coming from different observational sources including radar, single-level observations (typically surface observations) and multiple-level observations such as upper-air soundings. An ADAS surface-only analysis can be performed quite efficiently. The ADAS is easily implemented. More importantly, the ADAS is attractive for high-resolution analysis as it performs analysis on model levels, rather than on pressure levels.

The ADAS combines observations with a background (first guess) by using the successive-correction method of Bratseth (1986), which gives an analysis that converges to an optimal interpolation (OI) analysis. Like the OI scheme, the Bratseth scheme accounts for the relative error between the observations and the first guess. Different from the OI scheme, this scheme iterates without the inversion of large matrices. Hence, this scheme requires less computer time and memory compared to the OI scheme. This type of scheme has been used successfully in research and operational mesoscale modeling (e.g., Sashegyi et al. 1993; Ioannidou and Pedder 1999; Brewster 1996; Ruggiero et al. 1996, 1999). See section 2.2.2 for more details about Bratseth scheme used in the ADAS.

The ADAS has gained wide usage in research and operational forecasting. Research applications of the ADAS in northwest Utah for a strong cold-front passage (Ciliberti et al. 1999) and sensitivity experiments (Ciliberti et al. 2000) showed that realistic local and mesoscale structures could be analyzed with the aid of local data. Operational applications included short-range weather forecasting support over east-central Florida (Case et al. 2002), weather support for the 2002 Winter Olympics (Horel et al. 2002), and near-real-time applications to complex terrain in the western United States (Lazarus et al. 2002). For applications in complex terrain, Lazarus et al. (2002) introduced into the ADAS a terrain factor for surface data [1]. The terrain factor affects only the analysis in the free atmosphere. More recently, Xue et al. (2003) demonstrated positive impacts of the ARPS data assimilation system on successfully predicting tornadic thunderstorms.

[1]This idea was expanded for 3D data (surface and sounding data) by Keith Brewster (CAPS, 2004, personal communication) in a newer version (ARPS5.1.0)

2.2.2 The objective analysis scheme

The ADAS employs a univariate analysis scheme of a successive-correction method developed by Bratseth [see Bratseth (1986) for more details]. The Bratseth scheme works in an iterative fashion solving for two analysis equations: one for an analysis estimate at the grid point, and the other for an analysis estimate at the observation location.

The desired analysis at the grid point x is given by

$$F_x^A(\mu+1) = F_x^A(\mu) + \sum_{j=1}^{n_{obs}} a_{xj}\left[F_j^O - F_j^A(\mu)\right] \tag{2.2}$$

while the analysis estimate at the observation location i is solved by

$$F_i^A(\mu+1) = F_i^A(\mu) + \sum_{j=1}^{n_{obs}} a_{ij}\left[F_j^O - F_j^A(\mu)\right] \tag{2.3}$$

where F is any meteorological field to be analyzed, μ is the iteration counter, a including a_{xj} and a_{ij} are optimal weights for spreading data, and n_{obs} is the total number of observations. Subscript x indicates an analysis grid point, whereas i, j are indices for observations. Superscripts A, O and B represent the analysis estimate, observation and background, respectively. Initially, $F_x^A(0) = F_x^B$ and $F_i^A(0) = F_i^B$.

The main difference between equations (2.2) and (2.3) lies in the definition of the optimal weights a. The grid-point analysis weight a_{xj} is given by

$$a_{xj} = \frac{\rho_{xj}^B}{m_j} \tag{2.4}$$

and the observation analysis weight a_{ij} is

$$a_{ij} = \frac{\rho_{ij}^B + \delta_{ij}\left(\dfrac{\sigma^O}{\sigma^B}\right)^2}{m_j} \tag{2.5}$$

where ρ_{xj}^B is the spatial correlation of background errors between an analysis grid point and an observation location; while ρ_{ij}^B is the spatial correlation of background errors between two observation locations; $(\sigma^O)^2$ and $(\sigma^B)^2$ are the observation and background error variances, respectively; δ_{ij} is the Kronecker delta (unity for $j = i$); and m_j is a "normalization factor," which is chosen to guarantee fast convergence (Bratseth 1986) as follows

$$m_j = \sum_{k=1}^{n_{obs}} \left| \rho_{jk}^B + \delta_{jk}\left(\frac{\sigma^O}{\sigma^B}\right)^2 \right| = \sum_{k=1}^{n_{obs}} \left|\rho_{jk}^B\right| + \varepsilon^2 \tag{2.6}$$

Here ε^2 is the ratio of the observation error variance to the background error variance. The degree to which the analysis converges toward the observations depends on the error variance ratio ε^2.

Equations (2.4) and (2.5) are simplified forms from the original definitions [Eqs. (15a) and (15b) in Bratseth (1986)] based on following assumptions:

- The observation errors are uncorrelated with the background errors

- The observation errors are uncorrelated with each other
- The background errors are homogeneous
- The observation errors at each observation station are equal

In the ADAS, contributions from different observation types are summed additively, so different observation errors can be specified for different observation types. In this thesis, only surface weather observations are used. The observation errors at each surface weather station are assumed to be equal (i.e., $\sigma_i^O = \sigma_j^O = \sigma_k^O = \sigma^O$).

In the unmodified version of the ADAS, the spatial correlations of the background errors are modeled as Gaussian.

2.2.3 Modifications

ADAS versus MC2 grids

Because ADAS is a component of the ARPS, the analysis was originally designed by CAPS to be performed on the ARPS grid (also called ADAS grid). Their external file conversion program interpolated various NWS/US standard gridded data sets (e.g., RUC, Eta, and AVN, et. al.) to the ADAS grid. The output on the ADAS grid was then used as the background for the ADAS analysis.

In this study, the MC2 model is run to provide the background (also called first guess). For better analysis quality, the MC2 model output are not mapped onto the ADAS grid. Instead, analyses are performed directly on the MC2 grid using MC2 output as first-guess fields. To this end, the ADAS horizontal and vertical grid definitions are modified to match those in the MC2 model; x and y coordinates of the model grid are modified from one-dimension to two-dimensions. Correspondingly, all subroutines related to x and y coordinates are modified. Programs were developed to read first-guess fields in RPN-FST format from MC2 and to write the analyzed fields in FST format.

Quality control

For surface observations, quality-control options include climatological checks, temporal checks, horizontal-consistency checks [Barnes (1964) technique] and observation-to-background difference checks. Climatological checks ensure that observations fall within broadly acceptable meteorological bounds. The temporal checks compare two consecutive hourly surface data and ensure that the difference between hourly changes at an individual station and averaged hourly changes of all stations is less than four standard deviations.

For those portions of our case studies with virtual observations, no quality control is needed. For those case studies with real observations, the horizontal-consistency checks and observation-to-background difference checks are turned off for the following reasons. The Barnes technique does not work well for quality control of fine-resolution data in complex terrain, because any one surface observation might not be represented well by nearby observations at different elevations or on the opposite side of a mountain range. In steep terrain, the observation-to-background difference might be large due to a discrepancy between the actual station elevation and the model grid-point elevation, rather than due to poor quality of the surface observation. We have reduced the ADAS trilinear interpolation

to bilinear when the first-guess fields are interpolated to the observation locations. The ADAS trilinear interpolation algorithm causes large interpolation errors by introducing "free atmosphere" background values (Lazarus et al. 2002); also, the algorithm causes large extrapolation errors for the surface valley stations far below the lowest model level.

Anisotropic correlation function

The ADAS Bratseth scheme works iteratively, updating the first guess using the difference between the observed values and observational estimates derived from the analysis (see section 2.2.2). The optimal Bratseth weights [a_{xj} in (2.4) and a_{ij} in (2.5)] rely on the spatial correlation (ρ) of the background errors (and on the ratio of observation error variance to background error variance). Over flat terrain, a Gaussian function [$G(d)$] is frequently used to smoothly reduce the correlation with distance (d), causing the impact of a single observation to be isotropic in the grid space around the observation [$\rho(d) \propto G(d)$].

In mountainous terrain, this study modifies the Gaussian drop-off to be a function of the circuitous travel distances (s, defined later in section 3.3) from the observation to an analysis point [$\rho(s) \propto G(s)$]. To account for terrain effects, the correlation should be weighted by an anisotropic term (S) that is a function of the difference between elevations of the observation (Z_o) and the analysis point (Z_a). By separating horizontal and vertical effects into two factors, an anisotropic correlation becomes

$$\rho(s) = G(s) \cdot S(Z_o, Z_a) \tag{2.7}$$

One approach for anisotropic objective analysis is to utilize valley masks, within which valley-floor observations can be spread. However, the definition of a valley mask based on absolute terrain elevation alone is problematic, because in steep terrain, a valley floor in one part of the forecast domain might be higher than the ridge top in another. What is needed is a mask based on terrain elevations relative to the observation point, regardless of whether the observation is in a valley or on a mountain slope or ridge top. Also, the word "mask" implies an on/off situation. However, a better approach is to have the observation-increment weight gradually fade to zero as one moves to grid points that are further from the elevation of the observation site, given the uncertainties in boundary-layer characterization.

A mother-daughter (MD) approach is proposed in Chapter 3 to generate the vertical factor (S) and the circuitous travel distances (s) for each observation station. The hypotheses behind the technique are also presented in Chapter 3.

2.3 An overview of surface weather observations

The "Emergency Weather Net Canada", operated and maintained by the Geophysical Disaster Computational Fluid Dynamics Center at UBC, exists to archive and provide timely and comprehensive surface weather observations for western Canada. Hourly data sets are combined in the Emergency Weather Net database from several agencies, including the BC Ministry of Transportation (MOT), BC Ministry of Forests (MOF), BC Ministry of Water Land and Air Protection (WLAP), Greater Vancouver Regional District (GVRD), Environment Canada (EC), BC Hydro (HYDR), CN Railroad (CNRL), CP Rail (CPRL)

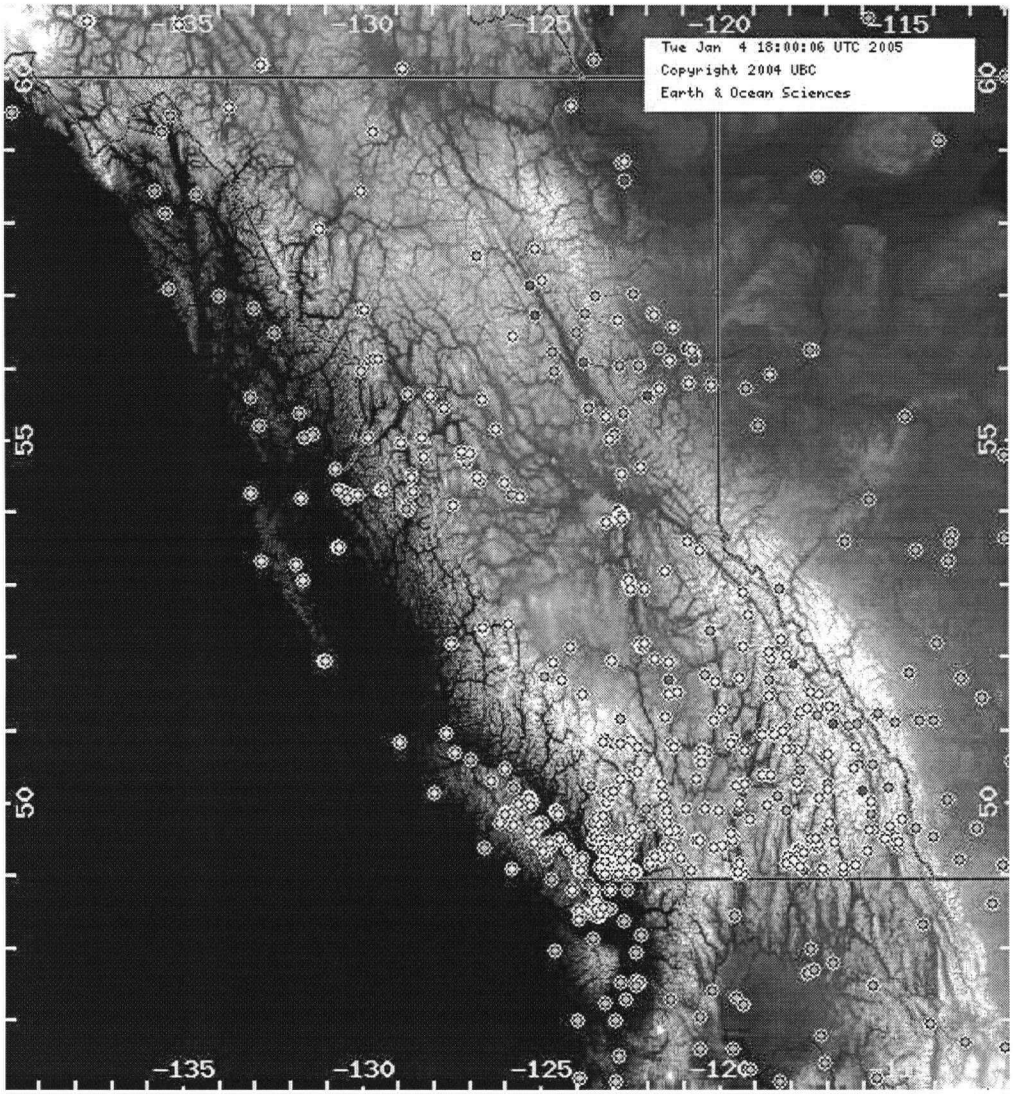

Figure 2.5: A graphic display of surface weather stations over British Columbia and its surroundings from Emergency Weather Net Canada. This image was created by George Hicks, who maintains the Emergency Weather Net Canada database.

and UBC. This real-time weather information system makes it possible to get frequent and dense surface weather observations in BC for the use in data assimilation and analysis/forecast verification as well. Figure 2.5 shows available surface weather stations over BC from Emergency Weather Net Canada for one day recently. There are relatively more observations over the Georgia Basin [i.e., within the bigger 3-km domain and 2-km domain in Fig. 2.2] and Okanagan regions [i.e., center of the 3-km domain (b) in Fig. 2.3]. Dense observations result in more accurate estimates of current atmospheric state, and also provide an opportunity for verification with independent observations. That is why we choose to look at the Georgia Basin and Okanagan regions for the real-observation cases.

Meteorological fields from Emergency Weather Net Canada include surface temperature, relative humidity, mean sea-level pressure (or surface pressure) and wind speed/direction. Observations of cloud cover are not available in the Emergency Weather Net Canada and thus cloud analyses are not performed. Assimilation of the moisture variable such as specific humidity would indirectly change the cloud formation within the model. Precipitation is not considered in this thesis because it is not a boundary-layer process. In addition, there are very few precipitation reports from Emergency Weather Net Canada. Temperature and moisture variables are used for both analysis and verification, while others are used for forecast verification only.

Potential temperature varies smoothly over mountainous terrain when the boundary layer is relatively deep and well mixed (Miller and Benjamin 1992), thus it is chosen as the temperature variable for analysis. For case studies with virtual observations, the potential temperature corresponds to the temperature that a parcel would have if it were moved adiabatically to a reference pressure (i.e., 100 kPa). For case studies with real observations from the Emergency Weather Net Canada (having much fewer surface pressure observations than temperature observations), the potential temperature is the temperature that the air would have if it were brought adiabatically to sea level. The calculations presume a dry adiabatic (no heat exchange) lapse rate of 0.0098 °C/meter. This means that the actual air temperature is the potential temperature minus 0.0098 times the altitude in meters. Potential temperature is also the temperature variable analyzed in the ADAS.

Specific humidity is chosen as moisture variable for analysis and assimilation into the MC2 model for two reasons: 1) the moisture variable in MC2 nesting data is specific humidity, and 2) specific humidity is a continuous variable. Specific humidity is also one of the moisture variables analyzed in the ADAS. To derive specific humidity from relative humidity, the saturation specific humidity is first calculated using the enhanced Teten's formula, as in ARPS (Xue et al. 2000) model. This calculation requires surface temperature and station pressure as input. There are very few reports of station pressure from Emergency Weather Net Canada. In the case of missing station pressure, mean sea-level pressure is used to approximate station pressure according to the altimeter equation (standard atmosphere) for stations with elevations below 500 m.

2.4 Statistical verification measures

To assess the analysis skills of different analysis methods, and to evaluate forecast impacts of assimilating surface observations into the MC2 model, statistical comparisons of analyzed (or modelled) values with observed values are conducted based on following measures.

Let n be the total number of all the available paired data values (one observed, and one analyzed or modelled). The bias, mean absolute error (mae), root-mean-square error (rmse) and root-mean-square vector error (rmsve) are defined as:

$$bias = \frac{1}{n}\sum_{i=1}^{n}(f_{a,i} - f_{o,i}) \tag{2.8}$$

$$mae = \frac{1}{n}\sum_{i=1}^{n}|f_{a,i} - f_{o,i}| \tag{2.9}$$

$$rmse = \left[\frac{\sum_{i=1}^{n}(f_{a,i} - f_{o,i})^2}{n}\right]^{\frac{1}{2}} \tag{2.10}$$

$$rmsve = \left[\frac{\sum_{i=1}^{n}((u_{a,i} - u_{o,i})^2 + (v_{a,i} - v_{o,i})^2)}{n}\right]^{\frac{1}{2}} \tag{2.11}$$

where f is any scalar meteorological field, u and v are the eastward and northward vector wind components, respectively. The subscripts a and o indicate analyzed (or modelled) and observed values, respectively. No single error measure is the best; they all give useful and different information (Wilks 1995). Bias can be either positive or negative. A positive bias indicates a tendency to overestimate that variable. A smaller magnitude of bias, and lower values of mae and rmse (or rmsve), indicate a better analysis or forecast.

Surface-data analyses of potential temperature and specific humidity are performed at the first thermodynamic level. Therefore, bias, mae and rmse of potential temperature and specific humidity are determined for analyzed (or modelled) potential temperature and specific humidity at the first thermodynamic level (5.3 m above model ground) against the observed surface potential temperature and specific humidity, respectively. Error measures of winds are determined for modelled winds at the first momentum level (10.6 m, after rotating to the proper earth coordinates) against the observed surface winds. No height adjustment was conducted for any one of these variables. By choosing potential temperature as the temperature variable, effects of elevation difference are minimized. The errors in the elevation differences between observations and analyses or forecasts are always the same for all the analysis methods or assimilation strategies.

Several other facts must be noted when comparing modeled and observed near-surface weather parameters. Observed values are measured at a specific spot usually in clearings and are mean values over a specified period of time (e.g., hourly or 10 minutes). A surface station might not be representative of the surrounding area. For example, a surface station in forests with its neighboring trees cut might not be representative of its surrounding forests. Modeled values are instantaneous and represent a volume-averaged value. The forecasts will have some statistical errors associated with these facts. Again, these errors are always the same for all assimilation strategies.

Chapter 3

Anisotropic mesoscale surface-analysis method for mountainous and coastal terrain

This chapter presents a technique that allows the creation of a new anisotropic correlation model for objective analysis of surface weather observations in complex terrain. Before detailing the technique, some hypotheses are described, followed by a review of basic concepts of the atmospheric boundary layers (BLs) in mountainous terrain.

3.1 Introduction

Objective analysis transforms information from randomly spaced observing sites into data at regularly spaced grid-points (Krishnamurti and Bounoua 1996). It is often done by optimally combining observations and a short-range NWP forecast, called a first guess (background). Analysis schemes, such as optimal interpolation (OI) (Daley 1991), successive corrections (Bratseth 1986), and 3D variational analysis (Laroche et al. 1999), require the specification of a covariance function to model the spatial correlations of background errors (see Chapter 1). The background error covariance, used to define the optimal weights for data spreading, is often assumed to be isotropic.

As mentioned in Chapter 1, isotropy is a questionable assumption for mesoscale analyses or for analyses in mountainous/coastal regions. Therefore, flow-dependent or anisotropic covariance models are receiving more attention, such as by introducing isentropic (Benjamin et al. 1991) or semi-geostrophic (Desroziers 1997) coordinate transformations in analysis increments. Flow-dependent background-error covariance can also be estimated explicitly by Kalman-filtering (KF), implicitly by 4D variational methods (4D-Var), or approximated in the ensemble Kalman filter (EnKF) (Gauthier et al. 1993; Bouttier 1993; Thépaut et al. 1996; Houtekamer and Mitchell 1998, 2001). But KF, 4D-Var and EnKF are computationally time-consuming. Lanzinger and Steinacker (1990) incorporated anisotropic correlation structures due to orography to resolve sharp gradients across major mountain ridges (Alps, Pyrenees). Miller and Benjamin (1992) used elevation differences in correlation functions to account for terrain effects.

In the mountainous terrain of western North America, many surface observation sites

are located in deep valleys. Both the background error covariance and representativeness of surface observations are affected by heterogeneous terrain. BC has a variety of landscapes from seashores, straits, and fjords to mountains and valleys. Some valleys are narrow and long with kinks and twists. The need for weather data at many sites in a valley is often not matched by the availability of weather stations. Typically, villages are strung along the valley floor, with ski resorts higher up the slopes and reservoirs in tributary valleys. Observations from a surface weather station at one village in the valley is often not representative of conditions up- or down-valley, nor is it representative of conditions on nearby mountain slopes. Similarly, weather observations at ridge top would not be representative of surface weather in the adjacent valley.

This typical scenario stimulates the following question. At locations (in that one valley) distant from the observation station, which of the following better represents the initial air state: 1) the first guess (from a previous high-resolution forecast) or 2) the observations from the distant station? One advantage of the first guess is that the previous, high-resolution forecast already includes terrain-forced mesoscale flows that are dynamically balanced. A disadvantage is that forecast skill decreases rapidly with time due to the nonlinear nature of the atmosphere. An experiment to address this question would be to densely instrument the valley in question, and determine the correlations between all the observations, and between the observations and the first guess. However, it is likely that the conclusions from such a study would apply only to that one valley, and would not apply to other valleys in the same or different mountain ranges. These other valleys have different orientations, lengths, steepness, slopes, locations near or distant from the coast, locations near or distant from the mountain range spine (such as the Rocky Mountains and Coast Mountains), vegetation, and latitude. It might also be risky to apply results from other densely instrumented valleys elsewhere in the world (such as the Mesoscale Alpine Project) to the valleys in BC.

Within the constraints of the present numerical experiments, we hypothesize that in a serpentine valley, the first guess (from a fine-resolution NWP model) is better than a distant observation from the same valley, in the absence of dense intravalley observations. This hypothesis herein is referred to as the intravalley decorrelation assumption. An extension of this hypothesis treats two valleys separated by a high ridge, and herein is referred to as the intervalley decorrelation assumption. If there is an observation in only one valley, then the first guess in the noninstrumented valley represents the air state better than the observation from the other valley.

The intravalley and intervalley decorrelation hypotheses are implemented within the ADAS Bratseth scheme (see section 2.2) for data assimilation in complex terrain. The intravalley assumption uses a Gaussian drop-off with distance from the observation, but using distance that is measured along the circuitous path of the valley. The intervalley assumption uses an anisotropic term that reduces data spreading into terrain of differing elevation. The horizontal $[G(s)]$ and vertical $[S(Z_o, Z_a)]$ factors included in the anisotropic correlation function [see (2.7) in Chapter 2] correspond to the implementation of the intravalley and intervalley assumptions, respectively.

A mother-daughter (MD) approach is proposed in section 3.3 as a convenient, iterative way to calculate both the vertical effect (S) and circuitous travel distance (CTD) (s). The vertical effect is introduced via a "sharing factor" (SF); namely, the fraction of information shared between an observation and analysis grid point (GP). This approach is based on

first-order boundary layer (BL) characteristics in mountainous terrain, described next.

3.2 Topographic anisotropy and boundary layers

3.2.1 First-order boundary layer characteristics in mountainous terrain

Atmospheric BLs always contain air of lower potential temperature than the air higher in the free atmosphere, because the average troposphere is stably stratified (Stull 1988, 2000). Between the BL and free atmosphere is a strongly stable layer that caps the BL. Trapped in the BL below this cap are pollutants, humidity, and heat released from the surface.

In steep mountainous terrain such as in western Canada and USA, the ridge heights above valley floors are frequently the same order as BL depths. To a zeroth order, the turbulent and advective communication of physical, dynamic, and chemical states between one valley and the other depends greatly on whether the BL is shallower than the surrounding ridges. For shallow BL situations, tracers emitted into one valley BL are unlikely to reach neighboring valleys, due to blocking by mountains. For situations with BLs deeper than ridges, BL air can mix between neighboring valleys.

To a first order, the BL top (z_i) is often not level over complex terrain. Observations show a variety of behaviors, ranging from BLs that follow the topography to BLs that seem relatively level (Lenschow et al. 1979; De Wekker et al. 1997; Kalthoff et al. 1998; Kossmann et al. 1998). These observational studies showed that the BL top tends to be more terrain-following in the morning, and becomes less terrain-following (or more level) in the afternoon. Stull (1992) identified four archetypical BL-top characteristics (Fig. 3.1). Gravitational forces tend to make a level BL top (Fig. 3.1c), much like an ocean surface that is level over undersea mounts. Other factors including entrainment, advection, and friction tend to make a terrain-following top (Fig. 3.1b). Daytime anabatic circulations and venting effects can cause the BL-top to exaggerate the topographic relief (Fig. 3.1a). In the case of strong anabatic circulations, the up-slope winds converge at the mountain crests, which induce upward motion and possible cloud formation over the mountain tops. In such a case, the mountain and cloud venting processes might transport aerosols above the convective BL top, as shown in De Wekker et al. (2004). They identified the difference between aerosol-layer and convective BL heights based on lidar measurements on 30 July 1997, and found that the BL heights are more terrain-following and lower than the nearly level aerosol-layer heights. Some Bernoulli and mountain-wave effects can cause contra-terrain following (Fig. 3.1d). If the Froude number $Fr << 1$ (i.e., the airflow is subcritical), the air will flow around the mountain. Contra-terrain following BL top is possible for supercritical flow (i.e., $Fr >> 1$), where the air flows over the mountain and accelerates. See Stull (1998a) for a similarity-theory analysis of the competing factors. This study focuses on the level and terrain-following cases (Fig. 3.2).

BL parameterizations in NWP models are usually based on theories developed for flat prairies, and thus do not provide information on levelness of the BL top in steep mountainous terrain within first guess fields for use during data assimilation. Nor are observations of BL depth usually available at every surface weather station. In an attempt to compensate for the lack of information, we develop a background error correlation (ρ)

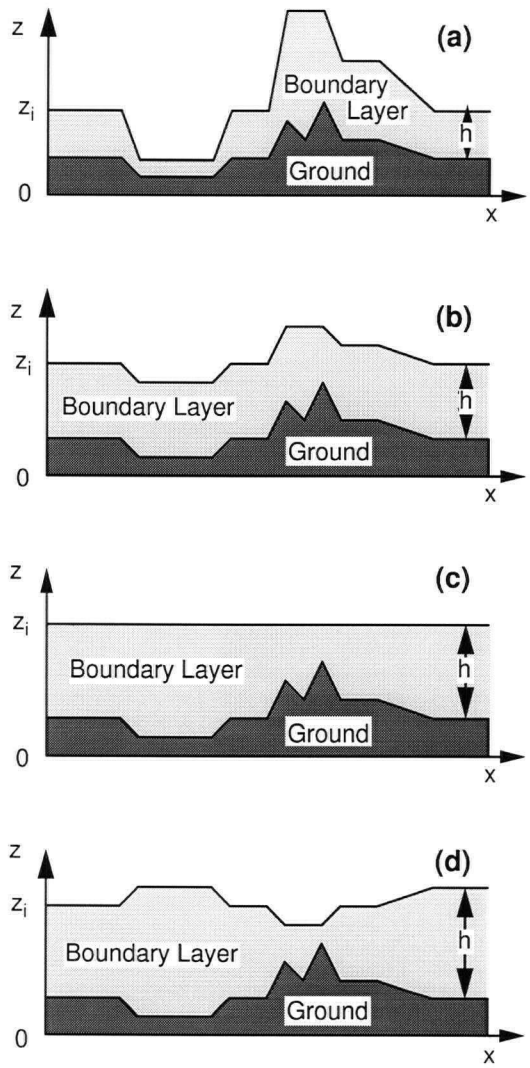

Figure 3.1: Archetypical categories of mixed-layer-top levelness (after Stull 1992). (a) Hyper-terrain following; (b) terrain following; (c) level; (d) contra-terrain following.

that includes weighting factors for both level-top and terrain-following BL effects. Namely, we define the sharing factor SF [S in (2.7)] during one iteration (from a source GP to one of its neighboring GPs) by

$$S_{od}(\nu+1) = S_{om}(\nu) \cdot W_{TFBL}(\nu+1,\nu) \cdot W_{LTBL}(\nu+1) \tag{3.1}$$

where subscript o represents the observation, subscripts m and d represent a GP (mother) and its neighboring GP (daughter), respectively. Weights W represent the portions of the SF associated with terrain-following BLs (TFBLs) or "level-top" BLs (LTBLs). The spreading iteration counter is ν.

3.2.2 Parameterization of terrain-following and level-top BL contributions

Let Z be the elevation. Approximate the terrain-following BL effects on the SF, from one mother GP during iteration ν to a neighboring daughter GP at iteration $\nu+1$, by:

$$W_{TFBL}(\nu+1,\nu) = 1 - \left[\frac{|Z_m(\nu) - Z_d(\nu+1)|}{zref1}\right]^a \tag{3.2}$$

for $|Z_m(\nu) - Z_d(\nu+1)| < zref1$; otherwise $W_{TFBL} = 0$. The terrain-following BL-depth parameter is $zref1$, while parameter a controls the analysis decorrelation rate.

For illustration, suppose that $zref1 = 1$ km and $a = 1$. Let the weather station be collocated with a model GP (the first mother GP) at the base of linearly sloping terrain (Fig. 3.2a) such that each successive daughter GP is higher up the slope: $z(\nu) = 0$, 0.5, 1.0, 1.5 km... for $\nu = 0$, 1, 2, 3.... The iteration counter (ν) coincides with each successive daughter GP. The resulting sequence of weights from (3.2) is $W_{TFBL} = 1.0$, 0.5, 0.5, and 0.5. These weights accumulate multiplicatively via the iteration given by (3.1). Considering only terrain-following effects, $S(0) = 1$, $S(1) = 0.5$, $S(2) = 0.25$, and $S(3) = 0.125$. An outcome is that the GP at $Z = 1.5$ km has nonzero SF, for the case of a terrain-following 1-km-thick BL, where turbulence can mix valley variables up the mountain slope.

Similarly, we can define a level-top BL weight by

$$W_{LTBL}(\nu+1) = 1 - \left[\frac{|Z_o - Z_d(\nu+1)|}{zref2}\right]^b \tag{3.3}$$

for $|Z_o - Z_d(\nu+1)| < zref2$; otherwise $W_{LTBL} = 0$. The level-top BL-depth parameter is $zref2$, while parameter b controls the analysis decorrelation rate.

For illustration with the same sloping GPs as in the previous example, suppose that $zref2 = 1$ km and $b = 1$. The resulting sequence of weights from (3.3) is $W_{LTBL} = 1.0$, 0.5, 0., and 0. These weights accumulate multiplicatively via iteration as in (3.1). If we neglect the terrain-following effects, $S(0) = 1$, $S(1) = 0.5$, $S(2) = 0.$, and $S(3) = 0$. There is a different outcome in this case; the GP at $Z = 1.5$ km has zero SF, because it is above the level BL top (Fig. 3.2b). At all higher-elevation GPs, the SF is also zero. Those points higher on the mountain are assumed to be in a different air mass than the valley station. It is worth noting that $zref2$ is essentially the BL depth at the observation location.

These illustrations, albeit somewhat primitive, demonstrate that the basic BL characteristics can be parameterized in a way that allows anisotropic correlations to be created, as shown next.

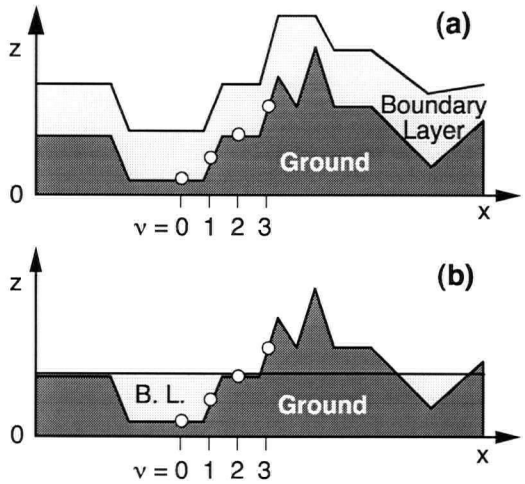

Figure 3.2: Shallow boundary layers in steep terrain, for (a) a terrain-following boundary layer and (b) a level-top boundary layer blocked by mountains. White dots represent surface grid points. The iteration counter is ν that coincides with each successive daughter grid point. The lowest grid point at $\nu = 0$ is collocated with the surface weather station.

3.3 The mother-daughter (MD) approach

This section uses the analogy of mothers spawning daughters, granddaughters and more distant generations to parameterize the preferential spread of information from an observation point to neighboring grid points and on to more distant grid points. Suppose that the amount of information that a mother GP transfers to each daughter GP is reduced by the elevation difference between them, based on the BL weighting functions just described.

First consider a surface observation that happens to lie directly on a model GP. The fraction of information shared between the observation and any analysis point is called "sharing factor" (SF), which ranges between 0 and 1. Let subscripts o, m and d represent an observation, a mother GP and a neighboring daughter GP, respectively. The iterative MD approach is expressed by

$$S_{od}(\nu+1) = S_{om}(\nu)\left\{1 - \left[\frac{|Z_m(\nu) - Z_d(\nu+1)|}{zref1}\right]^a\right\}\left\{1 - \left[\frac{|Z_o - Z_d(\nu+1)|}{zref2}\right]^b\right\} \quad (3.4a)$$

$$\text{if} \quad |Z_m(\nu) - Z_d(\nu+1)| < zref1 \quad \text{and} \quad |Z_o - Z_d(\nu+1)| < zref2$$

$$S_{od}(\nu+1) = 0 \quad \text{if} \quad |Z_m(\nu) - Z_d(\nu+1)| \geq zref1 \quad \text{or} \quad |Z_o - Z_d(\nu+1)| \geq zref2 \quad (3.4b)$$

where ν is iteration counter; Z is elevation; and a, b, $zref1$, and $zref2$ are free parameters. The iteration starts with $S_{om}(0) = 1$ at the surface observation location. As previously discussed, the first and second bracketed terms in Eq. (3.4a) contain the terrain-following [W_{TFBL} in Eq. (3.2)] and level-top [W_{LTBL} in Eq. (3.3)] BL effects, respectively.

The surface observation is treated as the first mother, who has daughters at each of her eight neighboring GPs. This is the first iteration ($\nu = 1$). These daughter SFs are

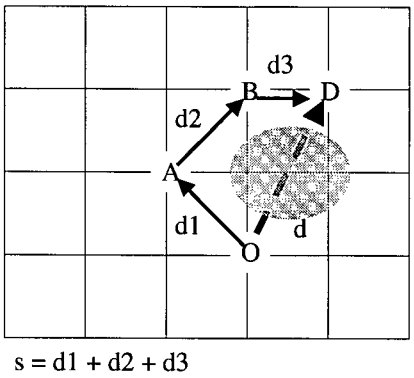

Figure 3.3: Schematic of the straight-line horizontal distance (d) and the circuitous travel distance ($s = d1 + d2 + d3$) from the observation location O to the grid point D, after the third iteration. The grid point D received the most contribution in its sharing factor from the grid point B, while the grid point B received the most contribution from the grid point A that received the most contribution from the observation O. This illustrates a situation such as when a mountain (indicated by shading) lies between O and D.

calculated by applying (3.4) to every mother-daughter pair. The circuitous travel distance (CTD) from the observation to a neighboring daughter GP, after $\nu = 1$, is equal to the straight-line horizontal distance if the SF at that daughter GP is not zero. For zero SF, the CTD is assigned a large value ($s = 1.0e5$ km), so that $\rho(s)$ in (2.7) is zero due to the Gaussian drop-off. Namely, the observation has no influence on that GP.

Next, every daughter becomes a mother and has her own eight daughters around her, and so on. Around any daughter might be several mothers who contribute different SFs to that daughter, but only the biggest SF (among all values from neighboring mothers and the value from the previous iteration) is kept. Thus, Eq. (3.4) has to be applied successively to every GP within a gradually enlarged subdomain centered at the observation location. This process is computationally expensive, as demonstrated later in section 4.3. From the second iteration onward, the CTD from the observation to any daughter GP is found by accumulating the incremental path segments from each successive mother to the daughter GP. Usually there are many different paths from the observation to a distant GP, but the path saved is the one that contributes the most to the sharing factor at that daughter GP. Figure 3.3 illustrates an example for the CTD (s) from the observation location O to GP D after the third iteration. From the daughter GP D, each previous mother was the GP at B, then A, and finally the observation point O.

To illustrate calculations of the SFs and CTDs, consider a surface station that happens to lie directly on a model GP at (x, y) = (7, 5) (Figs. 3.4 and 3.5, indicated by a solid triangle). Horizontal grid spacing is 3 km. Initially, the SF is 1.0 at the observation location, and zero elsewhere (left-hand panel of Fig. 3.4a). The CTD is initially 0 km at the observation point and 1.0e5 km otherwise (right-hand panel of Fig. 3.4a).

The SFs and CTDs after the first iteration are shown in Fig. 3.4b. The CTD for a daughter GP remains 1.0e5 km if its SF is 0. Thus, the CTD (s) from the observation to the GP at (8, 5) is 1.0e5 km, even though the straight-line horizontal distance (d) is 3 km. A daughter GP with nonzero SF has finite CTD [e.g., $s = d \approx 4.2$ km for GP (6, 6)].

In the second iteration, each daughter becomes a mother and has her own eight daughters around her, yielding 25 (8+16+1) daughters after $\nu = 2$ (Fig. 3.4c). The GP of the

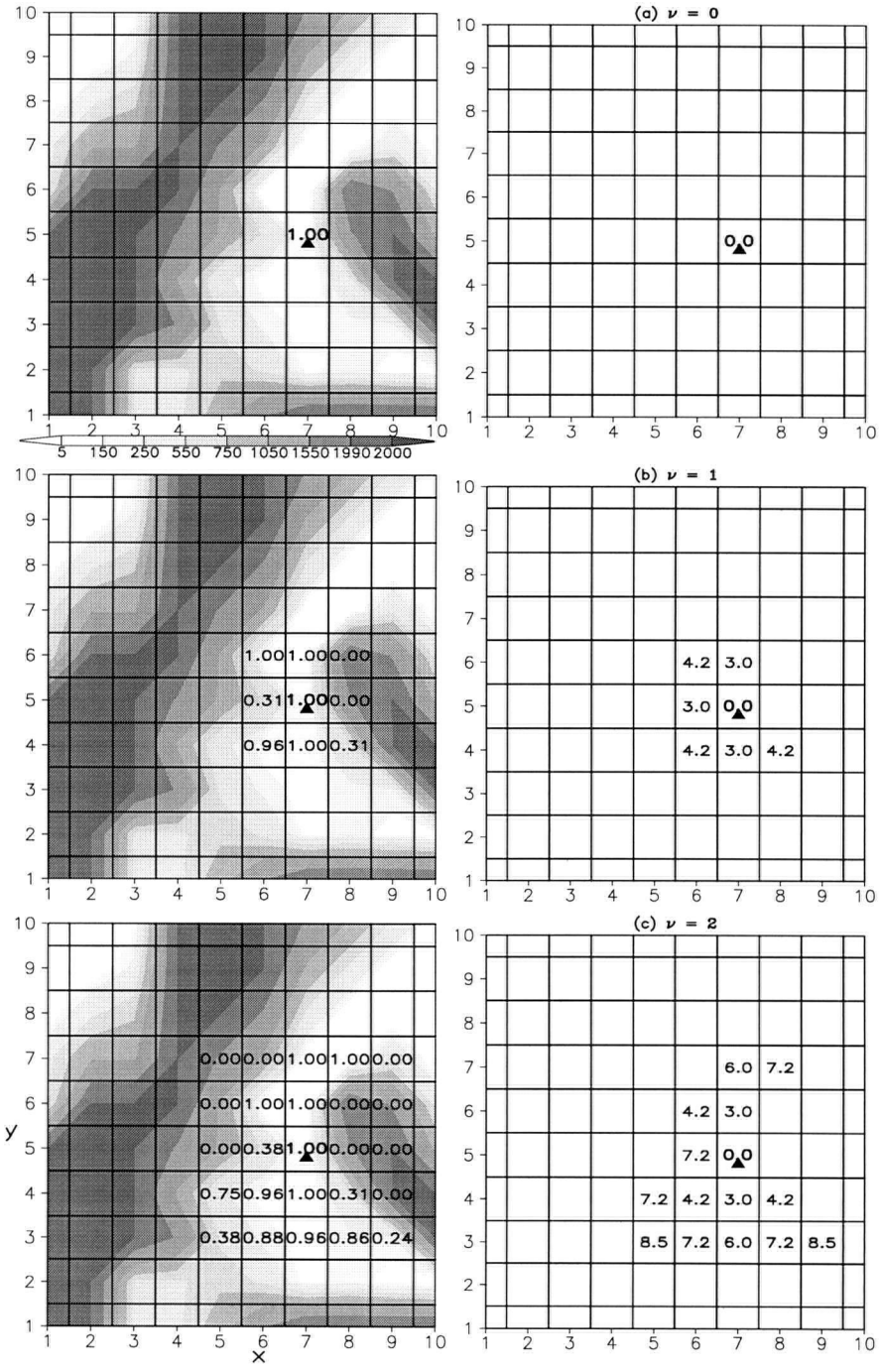

Figure 3.4: (left column) Printed values of the sharing factors (zeroes are not printed except when they first appear in an iteration; darker shading indicates higher elevations) and (right column) circuitous travel distance (km) (large values of 1.0e5 are not printed). (a) iteration counter $\nu = 0$; (b) $\nu = 1$; (c) $\nu = 2$. The observation is indicated by a solid triangle at $(x, y) = (7, 5)$. Grid spacing is 3 km. The parameters used are $a = 2$, $b = 2$, $zref1 = 750$ m, and $zref2 = 750$ m. Grid cells along the outside edge are cut off in this plot but are really the same size as all other grid cells.

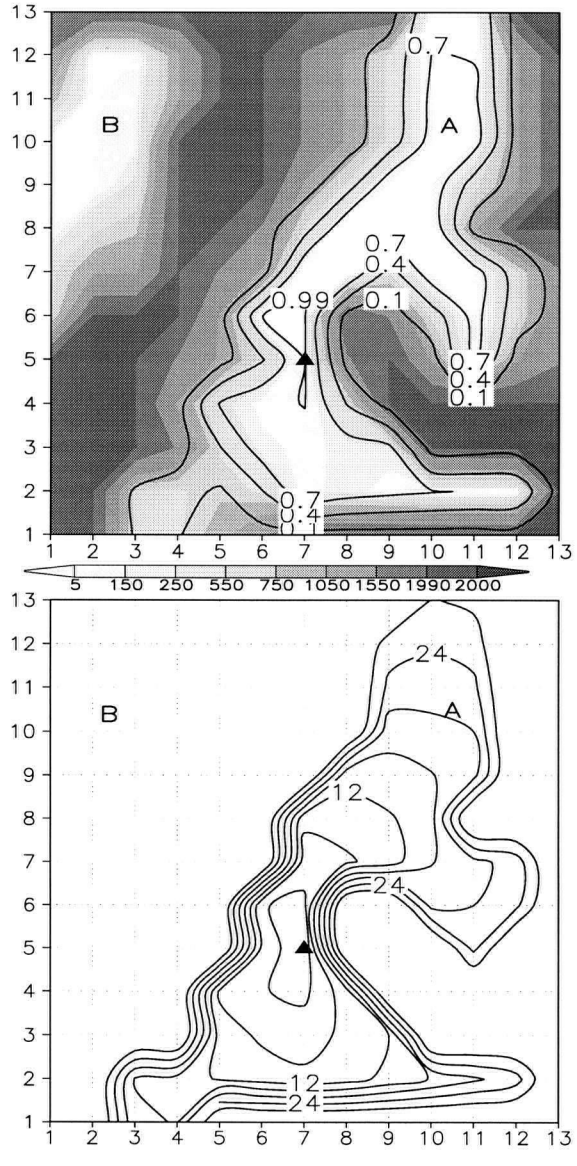

Figure 3.5: (top) Sharing factor isopleths (thin lines, after a Gaussian drop-off with standard deviation of 30 km) and (bottom) the circuitous travel distance (km) for an idealized observation in the valley A within a horizontal domain that spans 36 km x 36 km with a grid increment of 3 km. Terrain elevations (m) are shown by shading in the top plot. Darker shading indicates higher elevations, with a maximum terrain-height difference of 2000 m. The observation is indicated by a solid triangle at $(x, y) = (7, 5)$. The parameters used are $a = 2$, $b = 2$, $zref1 = 750$ m, and $zref2 = 750$ m.

first mother can also be a daughter GP of any grid point surrounding her, but the SF of the first mother is left unaffected as the biggest SF is kept during iteration.

This process is repeated until $|S_{od}(\nu+1) - S_{od}(\nu)| < 0.01$ for all GPs. The final SFs (S_{od}) and CTDs (s) are used in (2.7) to determine the anisotropic correlation function [$\rho(s)$]. Figure 3.5 shows the end results for this hypothetical station, using a Gaussian drop-off with standard deviation of 30 km. The observation information is spread along the Valley A where the observation is located. The valley B, disconnected from the Valley A, is unaffected, even though it is relatively close to the observation.

To examine the subtleties of the CTD, consider GP (6, 5) in Fig. 3.4. After $\nu = 1$, $S \approx 0.31$ and $s = 3$ km (Fig. 3.4b). Obviously, the SF comes from the first mother (i.e., the observation). After $\nu = 2$, $S \approx 0.38$ and $s \approx 7.2$ km (Fig. 3.4c). Now the largest SF comes from a second-generation mother GP (6, 4). The CTD ($s \approx 7.2$ km) equals the sum of $d \approx 4.2$ km between the observation and the second-generation mother GP (6, 4), plus $d = 3$ km from GP (6, 4) to the target GP (6, 5).

Parameters a and b in (3.4) control SF reduction by the mother-daughter GP elevation difference. As a and b are reduced from 4 toward 1, the terrain effects on the analysis increase. The optimal values of a, b, $zref1$, and $zref2$ can be obtained by analyzing a subset of the available observations, and verifying against the remaining observations for a substantial period of daily analyses, assuming a dense observation network. As mentioned before, $zref2$ is essentially the BL depth at the observation location. It is shown in Appendix C that analysis results are far more sensitive to $zref2$ than to $zref1$.

3.4 Application of the MD approach in the real world

In the previous section, the MD approach was presented for an idealized surface observation that was collocated with a GP of an idealized domain. In this section, several issues are discussed when the MD approach is applied to real observations within a real analysis/forecast domain of a NWP model.

As mentioned before, the topographical height in the NWP model can be locally very different from the real terrain height, due to the smoothing of topographical height for the NWP model. This means that any one modelled valley can be different from the corresponding real valley both in the width and depth. Figure 3.6 shows a cross section of the smoothed and unsmoothed topographic heights along 50.08 °N cutting through the MC2 2-km domain. When the MD approach is used in a real analysis/forecast domain, the model topographic height must be used. Thus, an observation is spread along the model-resolved valley, not the real valley [this implies that higher grid resolution (i.e., $\Delta x < 5$ km) is preferred for the MD approach]. Elevation of the model surface may be very different from the elevation of any weather station within the domain.

Also, most real weather stations do not happen to be collocated with any GP of the analysis/forecast domain. For the case of a surface weather station that is not collocated with a model GP, the station is first approximated as being collocated at the nearest neighboring model GP that has the minimum elevation difference between them.

Figure 3.7 illustrates an example with two observation stations (Os and Od) that are not collocated with any model GP. In this example, Os is a source observation location, which is approximated as being collocated at grid point C, one of the neighboring model

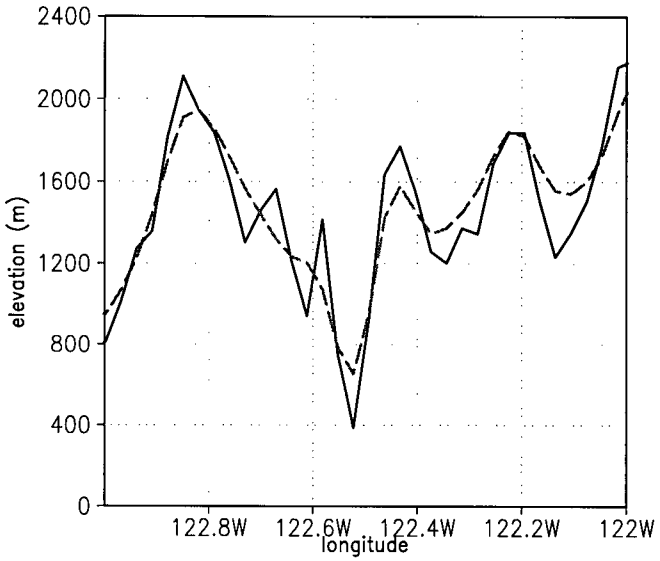

Figure 3.6: Cross section of the unsmoothed (solid line) and smoothed (dashed line) topographic heights along 50.08 °N cutting through the MC2 2-km domain (Fig. 2.2). The unsmoothed topographic heights are closer to the real terrain.

GPs with minimum elevation difference between Os and GP C. The sharing factor at Os is 1.0. The sharing factor at GP C is first approximated by a Gaussian drop-off of elevation difference between Os and GP C with a standard deviation of 1500 m. Then the iterative MD approach starts at GP C as described in the previous section.

The end results are the sharing factors at every model GP for the source observation Os. When the surface observations are not collocated with any model GP, the spatial correlation between an observation location and another [ρ_{ij}^B in (2.5)] is determined by the sharing factor at that other observation location. To calculate the sharing factor between the source observation location (i.e., Os in Fig. 3.7) and another observation location (i.e., Od in Fig. 3.7), an approximation from GP D to Od (same as that from Os to GP C) is made. The spatial correlation between Os and GP D is an example of ρ_{xj}^B in (2.4), whereas the spatial correlation between Os and Od is an example of ρ_{ij}^B in (2.5).

Let S_{OD} and s_{OD} be the SF and CTD between Os and GP D respectively; S_{OO} and s_{OO} be the SF and CTD between Os and Od respectively. The spatial correlation between Os and GP D (ρ_{OD}) is parameterized by:

$$\rho_{OD} = G(s_{OD}) \cdot S_{OD} \tag{3.5}$$

and the spatial correlation between Os and Od (ρ_{OO}) is

$$\rho_{OO} = G(s_{OO}) \cdot S_{OO} \tag{3.6}$$

where

$$S_{OO} = S_{OD} \cdot \exp(-\frac{1}{2}\frac{|\Delta Z_{Dd}|^2}{\bar{h}^2}) \tag{3.7}$$

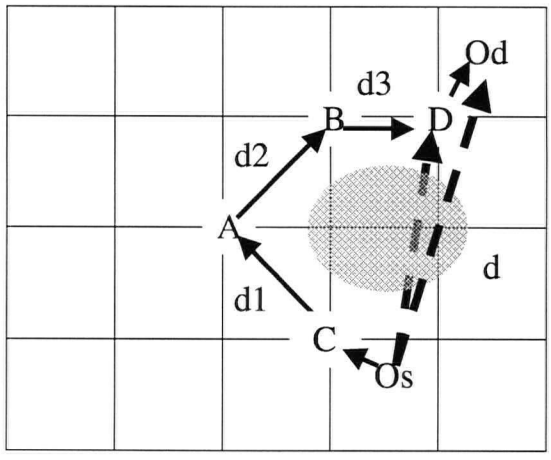

Figure 3.7: Schematic of the straight-line horizontal distances (d, as shown by dashed lines) and the circuitous travel distances (CTDs) from the source observation location Os to the grid point D and another observation location Od, after the third iteration. The grid point D received the most contribution in its sharing factor from the grid point B, while the grid point B received the most contribution from the grid point A that received the most contribution from the grid point C. The source observation Os is approximated as being collocated at the neighboring grid point C with minimum elevation difference between them. The grid point D is the neighboring grid point of Od with minimum elevation difference between them. The CTD from Os to the grid point D is $rs + d1 + d2 + d3$, whereas the CTD from Os to Od is $rs + d1 + d2 + d3 + rd$. This illustrates a situation such as when a mountain (indicated by shading) lies between Os and D.

and $s_{OD} = rs + d1 + d2 + d3$, $s_{OO} = rs + d1 + d2 + d3 + rd$ (see Fig. 3.7), ΔZ_{Dd} is the elevation difference between GP D and Od, and $\bar{h} = 1500$ m.

The SFs at the model GPs for one observation are dependent upon the elevation of that observation station and the elevations of the model GPs. Hence, the SFs at the model GPs for one observation station are independent of the SFs at the model GPs for another observation station. The MD approach can be used to generate stencils of different SFs and CTDs at the model GPs for different surface observation stations. The SFs and CTDs are then used to create the anisotropic spatial correlations between one observation and all model GPs and other observation locations [see (2.7), or (3.5) and (3.6)]. The values of optimal weights for spreading data in the ADAS Bratseth (1986) scheme are modified through the spatial correlations [see (2.4) and (2.5)]. The ADAS Bratseth scheme then combines multiple observations to determine the analysis at any grid point.

For a surface observation network, the observation stations and their elevations are relatively fixed even though the weather reports vary with time. For fixed GPs and observation locations within a model domain, the SFs and CTDs for each observation station can be determined once, outside of the daily data-assimilation process. The resulting SFs and CTDs are saved as a fixed file, which can be applied unchanged for each day's analysis to efficiently determine the correlations in the ADAS Bratseth scheme. In the presence of temporally missing observations, a flag (i.e., -999.) can be assigned to the missing observations. If a new station is added latter to the observation network, the new SFs and CTDs must be calculated and appended to the fixed file before the new observation can be used

in the analysis.

Although these results are incorporated into the ADAS in this study, the main ideas can be used in any objective analysis scheme in which the background error correlations depend on observation-to-gridpoint distances.

3.5 Refinements of the MD approach

3.5.1 Refinement for coastal terrain

Many coastal mountain regions, such as southwestern BC, contain complicated straits and fjords where thermal contrasts exist between land and water. The sea-breeze driven by a land-sea thermal contrast contributes to the recirculation and trapping of air pollution during anticyclonic synoptic episodes. Accurate land-sea thermal contrast in analysis and forecasts is of critical importance for air pollution studies.

To consider land-sea contrasts, Hessler (1984) estimated two correlation functions from surface-temperature statistics near the Baltic Sea. Between pairs of sea stations or pairs of land stations, he approximated correlations by $\exp(-0.08d^{0.13})\cos(0.4d)$, where d is the straight-line distance between two stations. Between sea and land stations, he used $\exp(-0.29d^{0.06})\cos(0.2d)$.

This work introduces a similar approach by including an additional factor to the sharing factor parameterization (i.e., the third term in brackets on the right-hand side):

$$S_{od}^{LS}(\nu+1) = S_{om}^{LS}(\nu)\left\{1-\left[\frac{|Z_m(\nu)-Z_d(\nu+1)|}{zref1}\right]^a\right\}\left\{1-\left[\frac{|Z_o-Z_d(\nu+1)|}{zref2}\right]^b\right\} \cdot\left\{1-\frac{|LS_o-\overline{LS_d(\nu+1)}|}{K_{LS}}\right\} \tag{3.8}$$

for $|Z_m(\nu)-Z_d(\nu+1)| < zref1$ and $|Z_o-Z_d(\nu+1)| < zref2$; otherwise $S_{od}^{LS}(\nu+1)=0$. The land-sea mask LS_o at the observation location is equal to one for a land observation and zero for a water observation. The land-sea mask $\overline{LS_d}$ at a daughter GP is similar, but averaged over the nine GPs immediately around and including the daughter GP. The average allows gradual transition of the SFs across the coastlines in an attempt to partly account for sea/land breeze effects. The coastline refinement does not consider subgrid lakes, as the land-sea mask data for MC2 are either one (land) or zero (water). Parameter K_{LS} controls the degree of the decorrelation between land stations and analysis points over water, or between water stations and analysis points over land; K_{LS} was subjectively set to 1.0 for the case studies in section 4.3 and for the near-real-time operational tests in Chapter 7.

Ideally, the location of the land-sea mask should shift as the sea/land breezes evolve every day, however this work neglects this shift. This allows a computationally efficient constant land-sea mask that still captures first-order effects.

The SFs from the MD approach, both before and after the shoreline refinement, are illustrated in Fig. 3.8 for two observations over the real terrain of Vancouver, Canada, and its surroundings. One observation is on land (the Lower Fraser Valley) and the other

is on water (the Georgia Strait). After refinement, the information from a land (water) observation is spread mostly within land (water) area, as desired.

3.5.2 Refinement for mountain-top observations

Surface weather stations are usually located in valleys. But, there are some surface stations located at high elevations in mountains, such as at ski areas and in subalpine forest ecosystems. The MD approach presented in section 3.3 is good for surface observations in valleys, but could be problematic for mountain-top observations. The MD approach is not able to spread information from a mountain-top observation to the grid points of surrounding mountain tops. This is particularly true if the observation is located at the top of a very steep mountain. The spreading to the surrounding mountain tops is desired for two reasons. During shallow cold-air pooling events, the high-mountain tops are all penetrating into the free atmosphere where they would experience the same weather. Second, during deep BL events with BL top above the mountain top, vigorous turbulence would also cause mixing across the valleys. Therefore, the MD approach is further refined to allow such spreading by treating mountain-top observations differently than valley observations.

The modified SF for a mountain-top observation is proposed as follows:

$$S_{od}^{MT} = S_{om}^{MT}\left\{1 - \left[\frac{|Z_o - Z_d|}{zref2}\right]^b\right\} \tag{3.9}$$

for $|Z_o - Z_d| < zref2$; otherwise $S_{od}^{MT} = 0$. The superscript MT indicates mountain-top observations; S_{om}^{MT} is the sharing factor at the mountain-top observation location, which is 1.0. The SF at any surrounding GP depends upon the elevation difference between the observation and the GP, and upon the level-top BL depth parameter $zref2$. No iteration is needed.

Now the question is: how to distinguish a mountain-top observation from a valley observation? A simple approach is taken here. Firstly, the model topographic heights are smoothed by the Barnes (1964) method (see Appendix B). The shape factor [R_v in Eq. (B.2)] of the empirical Gaussian weights is taken as 90 km, which is the same as the horizontal correlation length scale for the first Bratseth pass used in the surface data analysis (see Chapter 4). Secondly, the standard deviation (σ_Z) of the difference between the model terrain height and the smoothed model terrain height is calculated within a region of (-R_v, +R_v). If Z_s is the smoothed model terrain height, then the height of BL top (Z_{BL}) can be approximated by:

$$Z_{BL} = Z_s + max(0., zref2 - \sigma_Z) \tag{3.10}$$

where $zref2$ is the level-top BL-depth parameter in (3.4) and (3.9).

If the unsmoothed terrain height for any GP is above the approximated BL height Z_{BL}, then the GP is assumed to be in the free atmosphere, and is treated as a mountain-top location. The approximation of Z_{BL} is crude, but provides a simple and effective way to distinguish mountain-top observations from valley observations. As mentioned in section 3.4, in the case of an observation that is not collocated with any model GP, the station is first approximated as being collocated at whichever nearest neighboring model GP has the minimum elevation difference between them. In such a case, the elevation of the nearest

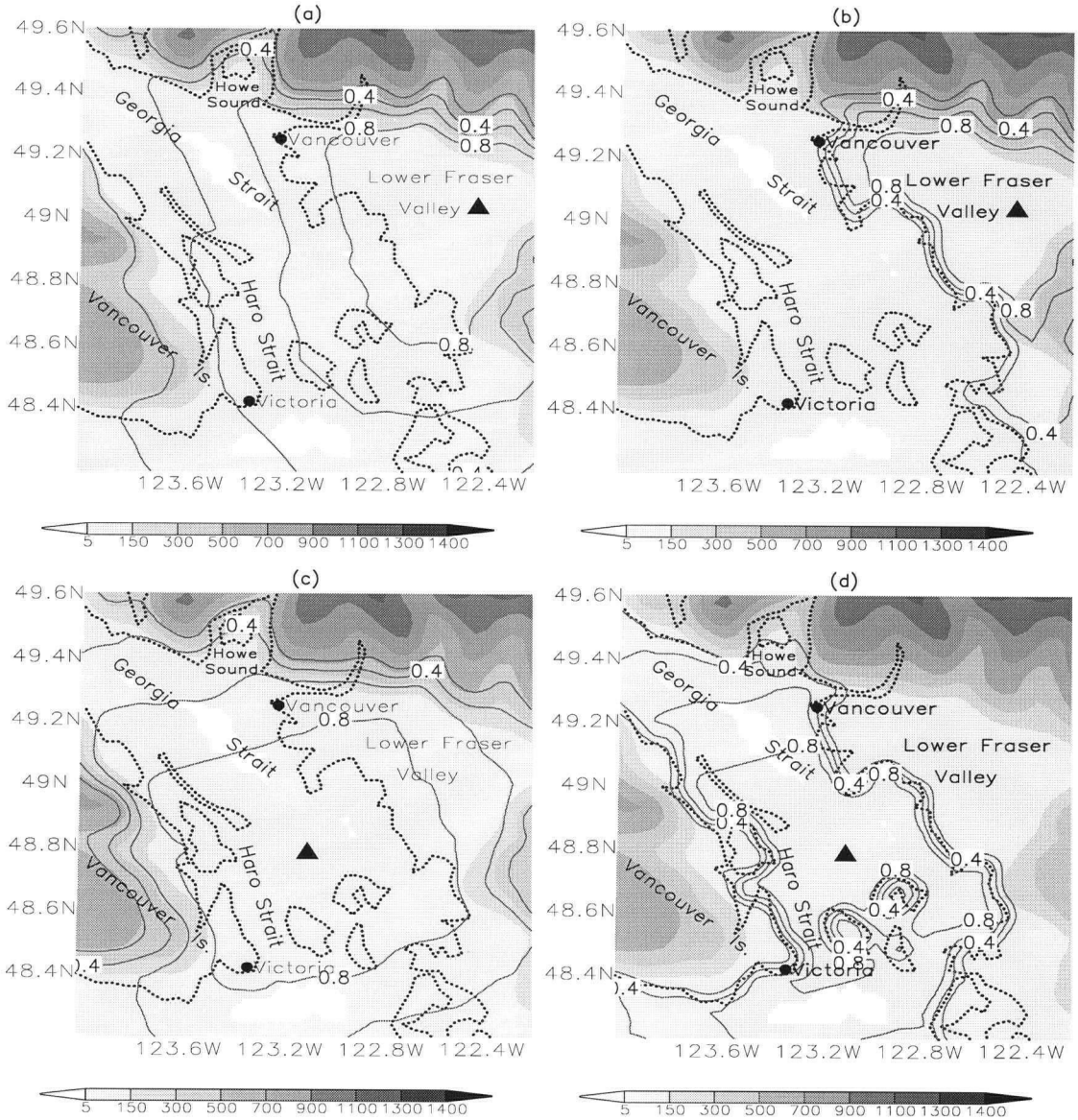

Figure 3.8: Sharing factors (solid lines) after a Gaussian drop-off with standard deviation of 90 km. The dotted lines indicate coastlines and islands. The observation station is shown by a solid triangle. (a) Results from the mother-daughter approach before coastline refinement for an observation over land in the Lower Fraser Valley just east of Vancouver; (b) Same as (a), except with land-sea contrasts included. (c) Same as (a), except for an observation over water (a location called the Georgia Strait); (d) Same as (c), except with land-sea contrasts included. Terrain elevations in meters, shown by gray shading, are from the smoothed terrain data used in the MC2 model (see section 2.1) at a grid spacing of 3 km. Darker shading indicates higher elevations, with a maximum terrain-height difference of 1217 m. The parameters used are: $a = 2$, $b = 2$, $zref1 = 750$ m, $zref2 = 750$ m.

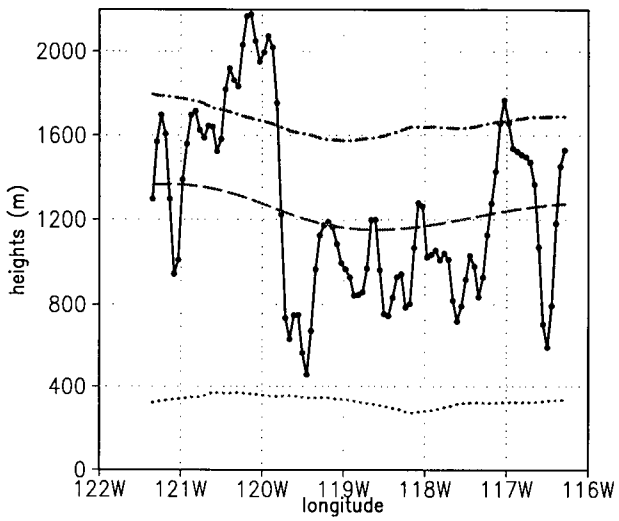

Figure 3.9: Cross section of the model topography (solid line), the smoothed model topography (dashed line), the approximated height of BL top (dot dashed line) and the standard deviation of the difference between the model topography and the smoothed model topography (dotted line). The cross section is along 49.0 °N cutting through the domain shown in Fig. 3.11. Any surface station located above the dot dashed line will be treated as a mountain-top station. The same is true for GPs. The regions where the solid line is above the dot dashed line are considered to be mountain-top locations.

neighboring model GP is compared with Z_{BL}. Any surface weather station that is above Z_{BL} is treated as a mountain-top station, whereas any surface station that is below Z_{BL} is treated as a valley station. The SF for a mountain-top station is obtained through (3.9), whereas the SF for a valley station is calculated via (3.4).

Figures 3.9 and 3.10 are cross sections of the model topography, the highly smoothed model topography (Z_s), the approximated height of BL top (Z_{BL}), and σ_Z. The former one is along 49.0 °N cutting through the domain shown in Fig. 3.11. The later one is along 50.08 °N, cutting through the domain shown in Fig. 3.12. Any surface station or GP located above the dot dashed Z_{BL} line will be treated as a mountain-top station or GP.

The model topography and the difference between the model topography and the approximated height of BL top are shown in Figs. 3.11 and 3.12 for the 3-km domain (b) in Fig. 2.3 and the 2-km domain in Fig. 2.2, respectively. Any surface station that is located in the darkly shaded areas in the bottom plots of Figs. 3.11 and 3.12 will be treated as a mountain-top station.

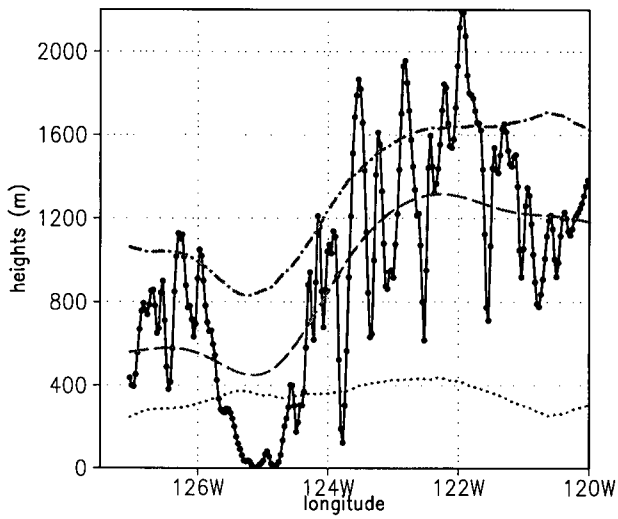

Figure 3.10: Same as Fig. 3.9, but the cross section is along 50.08 °N cutting through the domain shown in Fig. 3.12.

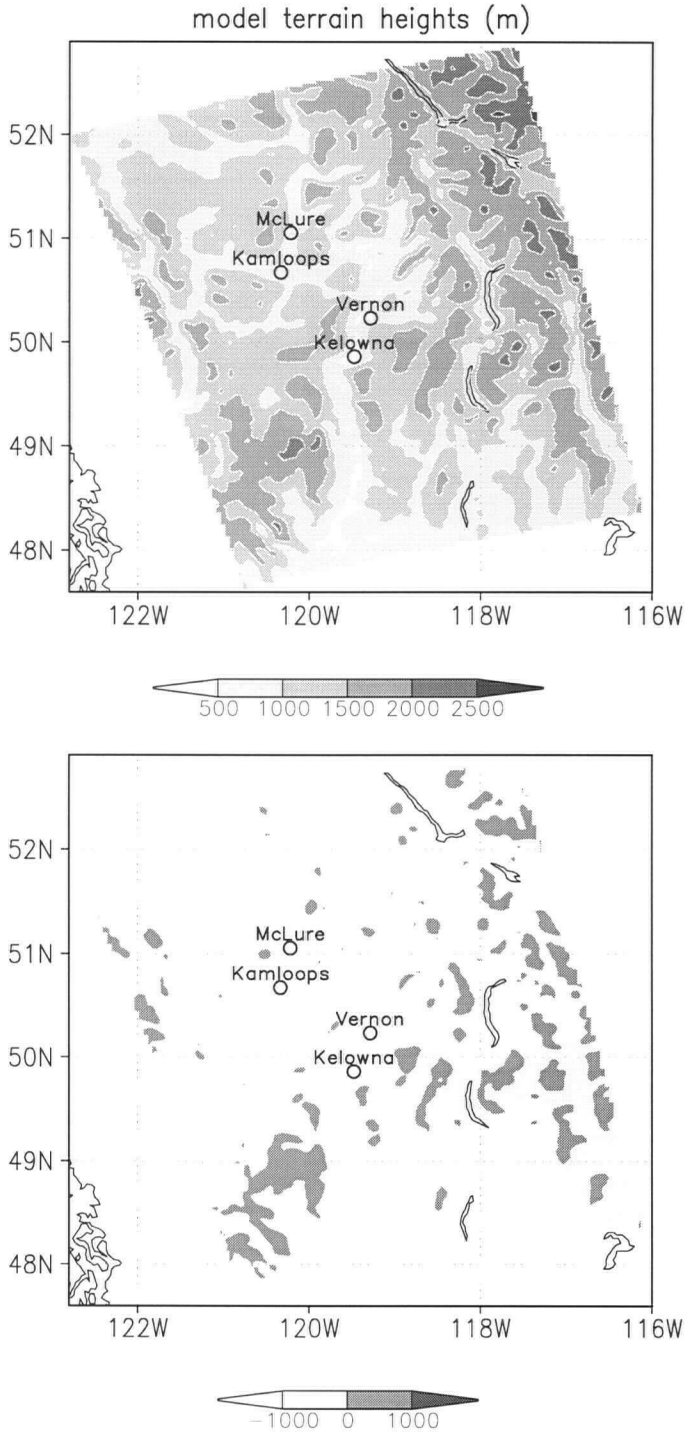

Figure 3.11: (top) The model topography (darker shading indicates higher elevations). (bottom) The difference between the model topography and the approximated height of BL top (any station located in the darkly shaded areas will be treated as a mountain-top station). This is for the 3-km domain (b) in Fig. 2.3. Open circles represent towns. Solid lines delineate lakes.

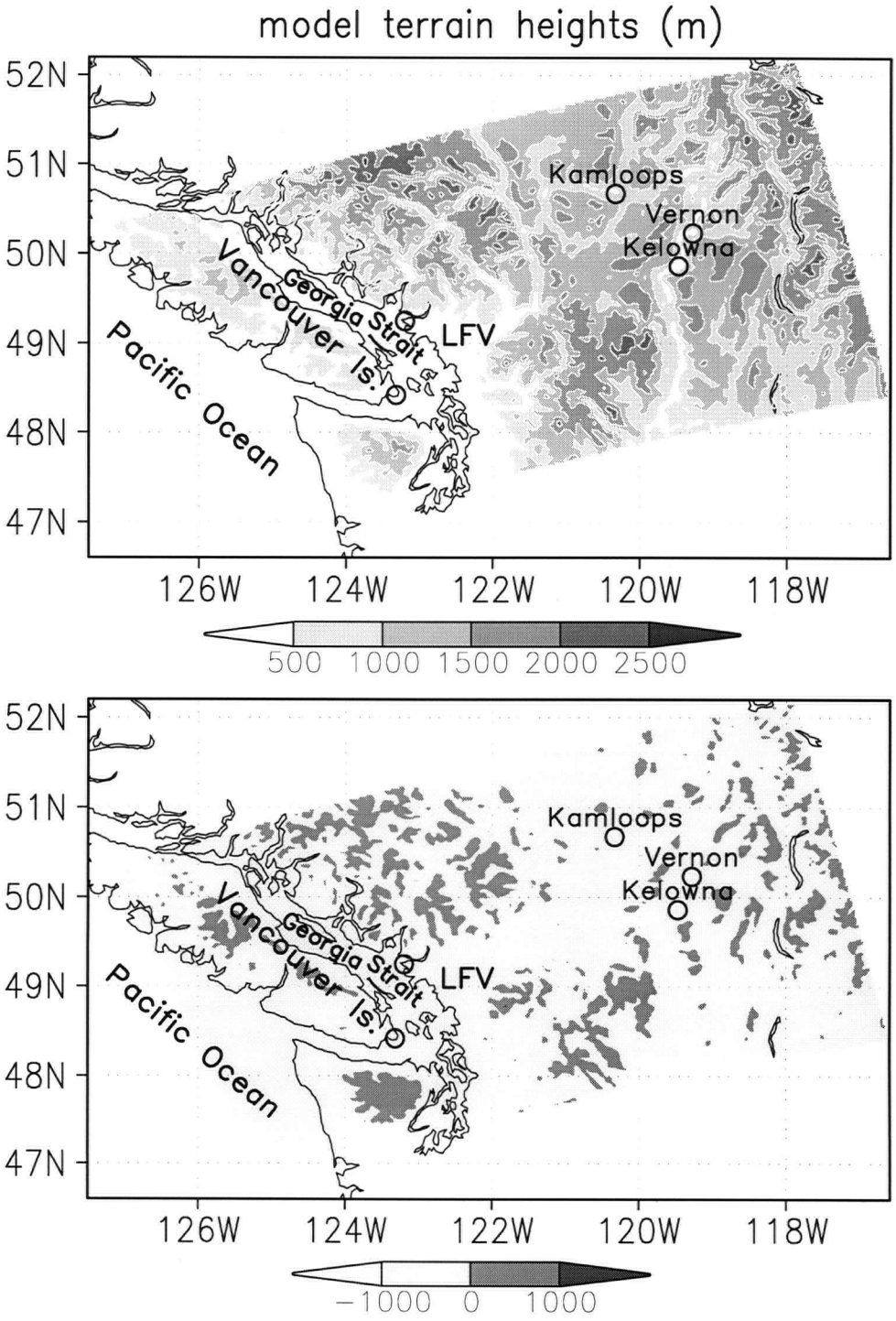

Figure 3.12: (top) The model topography (darker shading indicates higher elevations). (bottom) The difference between the model topography and the approximated height of BL top (any station located in the darkly shaded areas will be treated as a mountain-top station). This is for the 2-km domain in Fig. 2.2. Open circles represent towns. The open circle within LFV (Lower Fraser Valley) indicates Vancouver, while the open circle in Vancouver Island indicates Victoria.

Chapter 4

Case study tests of surface-analysis methods in mountainous/coastal terrain

4.1 Analysis methods

Five different analysis methods (Table 4.1) are compared. GAUSS, the native method in the ADAS (ARPS5.0.0 Beta8), includes terrain effects with a Gaussian function of elevation difference (Δz) between the GP and observation station, and with horizontal Gaussian decay to define the region of influence. In method TERR_DIFF, the Miller and Benjamin (1992) terrain-difference algorithm is added to the ADAS, but slightly modified from the original correlation function [1] for potential temperature.

In the mother-daughter (MD) method, the SFs from Eq. (3.4) are used to replace the Gaussian elevation term in GAUSS. MD further differs from GAUSS and TERR_DIFF by using the CTD (s), rather than the straight-line horizontal distance (d), in the horizontal part of the correlation function. This effectively limits the region of influence in complex terrain and restricts valley observation information to follow the valleys around the ridges, while reducing spread over the ridge top. Similarly, ridge-top information follows ridges, with little spread into valleys.

The MD_LSMG method is the same as MD except that land-sea anisotropy is included in the SFs (section 3.5.1). In method MD_MT, the sharing factors are from the mother-daughter approach after mountain-top refinement (section 3.5.2), which treats mountain-top observations differently from valley observations. For valley observations, s is the CTD as for method MD , whereas $s = d$ for mountain-top observations.

Unless stated specifically, the horizontal correlation length scale (R_h) is 90 km for the first and second Bratseth passes, 60 km for the third pass, and 30 km for the fourth and fifth passes.

The utilities of the MD approach and its refinements are demonstrated in the following sections for surface potential-temperature analyses in different regions. Virtual and real observations are used in numerical-experiment case studies for mountainous and coastal terrains in southwestern BC.

[1] $\exp(-|d|^2/2r^2)/(1+K_z\cdot|\Delta z|^2), r = 300\ km, K_z = 7\times10^{-7}\ m^{-2}$

Table 4.1: Analysis methods to be tested with numerical experiments, where R_h and R_z are correlation length scales in the horizontal and vertical, respectively, which define the regions of influence; d_{ij} and Δz_{ij} are straight-line horizontal distance and elevation difference between an analysis grid point and the observation station, respectively; K_z is a coefficient. s_{ij} is the circuitous travel distance from the observation to an analysis grid point determined in the mother-daughter program; S_{od} is the sharing factor at an analysis grid point, which represents how much the analysis grid point shares the observation information; S_{od}^{LS} is the same as S_{od} except that the former is from the mother-daughter approach with coastline refinement; S_{od}^{MT} is the sharing factor from the mother-daughter approach with mountain-top refinement. In this study, R_h is 90 km for the first and second iteration, 60 km for the third iteration, 30 km for the fourth and fifth iteration, during the ADAS assimilation cycle.

Method	**Correlation function (ρ)**
GAUSS	$\exp(-\frac{1}{2}\frac{\lvert d_{ij}\rvert^2}{R_h^2}) \cdot \exp(-\frac{1}{2}\frac{\lvert \Delta z_{ij}\rvert^2}{R_z^2})$
TERR_DIFF	$\exp(-\frac{1}{2}\frac{\lvert d_{ij}\rvert^2}{R_h^2})/(1 + K_z \cdot \lvert \Delta z_{ij}\rvert^2)$
MD	$\exp(-\frac{1}{2}\frac{s_{ij}^2}{R_h^2}) \cdot S_{od}$
MD_LSMG	$\exp(-\frac{1}{2}\frac{s_{ij}^2}{R_h^2}) \cdot S_{od}^{LS}$
MD_MT	$\exp(-\frac{1}{2}\frac{s_{ij}^2}{R_h^2}) \cdot S_{od}^{MT}$

4.2 Experiments using virtual observations

"Fraternal-twin" experiments are used first to evaluate the MD approaches in mountainous terrain. In fraternal-twin experiments, the "truth" and "analysis" models are similar, but not identical (Arnold and Dey 1986). The truth model (MC2 at 2-km grid spacing) is first integrated 12 h to generate a reference "truth" atmosphere. To generate a different first guess, the analysis model (MC2 at 3-km grid spacing with radiation turned off to purposely introduce errors) is integrated 12 h with the same boundary conditions, but started from perturbed initial conditions. Amplitudes of random perturbations for temperature (u wind, v wind, logarithm of pressure perturbation, specific humidity) are 5.0 °C (5.0 knots, 5.0 knots, 0.0005, 0.005 kg kg^{-1}). A dynamic initialization algorithm built into MC2 is activated for the 3-km run to remove spurious gravity waves excited by the added perturbations.

The fraternal-twin experiments are performed for 7-8 March 2003, characterized by an Arctic outbreak, when cold shallow air masses from northern Canada swept into the valleys in BC.

The MC2 runs consist of five self-nested grids with grid spacings of 108, 36, 12, 4, and 2 or 3 km (see Figs. 2.1 and 2.2). The Eta analysis and forecasts from NCEP, valid at 0000 UTC 7 March 2003, are used as the initial and boundary conditions for the coarsest grid. The MC2 at 2 km is started at 1200 UTC 7 March from MC2 4-km output, and integrated 12 h to generate the truth atmosphere, from which virtual surface observations are extracted. To simplify the problem and avoid complexity added by observations at the first stage, all virtual observations are assumed to be perfect, with zero observation error. Namely, the ratio of observation-error variance to background-error variance is zero. Observation errors will be considered for real observations later in this chapter and Chapters 6 and 7. The MC2 at 3 km is also started at 1200 UTC 7 March, but from the randomly perturbed output of the 4-km run, and integrated 12 h to provide a first guess. The analyses are performed at the lowest terrain-following model level of the MC2 3 km at 0000 UTC 8 March.

Figure 4.1 shows six virtual surface stations, all of which are placed in real valleys using the truth-model-resolved real topography for British Columbia. Stations o1 (elevation 920 m) and o2 (elevation 536 m), located in different valleys, are used for analysis. Station o1 is in the Elaho River Valley, and o2 is in the Lillooet River Valley. These two valleys are very narrow and deep with steep ridges and glacier-clad mountains on both sides, as shown in the aerial-reconnaissance photos (Figs. 1.4 and 4.2). Four stations (b1, b2, b3, and b4) in the Lillooet River Valley are used for verification. These stations are selected to evaluate the impact of observation o1 on the neighboring Lillooet River Valley. Elevations for stations b1, b2, b3 and b4 are 894, 881, 765, and 830 m, respectively.

4.2.1 Impact of a single valley surface observation

For objective analysis, the interpolated first guess is usually subtracted from the observation to give an "observation increment", which is then analyzed to produce "analysis increments" (AIs) at the GPs. The analysis at each GP is then the first guess plus the analysis increment. The AIs produced from the data at o1 show how data are spread to surrounding GPs.

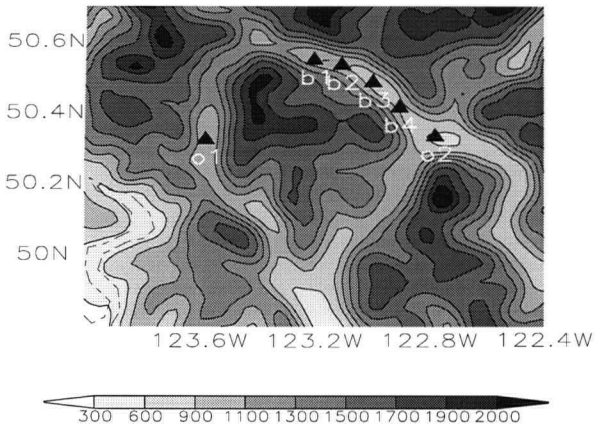

Figure 4.1: Virtual surface observation stations, indicated by solid triangles, used in the analysis and verification. The stations are positioned at the truth-model terrain height in the Coast Mountains north of Vancouver. Station o1 (50.326 °N, 123.578 °W) is near the mouth of the Elaho River. Station o2 (50.3344 °N, 122.767 °W) is near the town of Pemberton. Terrain elevations (m) are from the truth model. Darker shading indicates higher elevations, with a maximum elevation difference of 2055 m in this figure.

Figure 4.2: A narrow valley (the Lillooet River Valley mentioned in this chapter) in the Coastal Mountain Ranges north of Vancouver, as shown in an aerial photo.

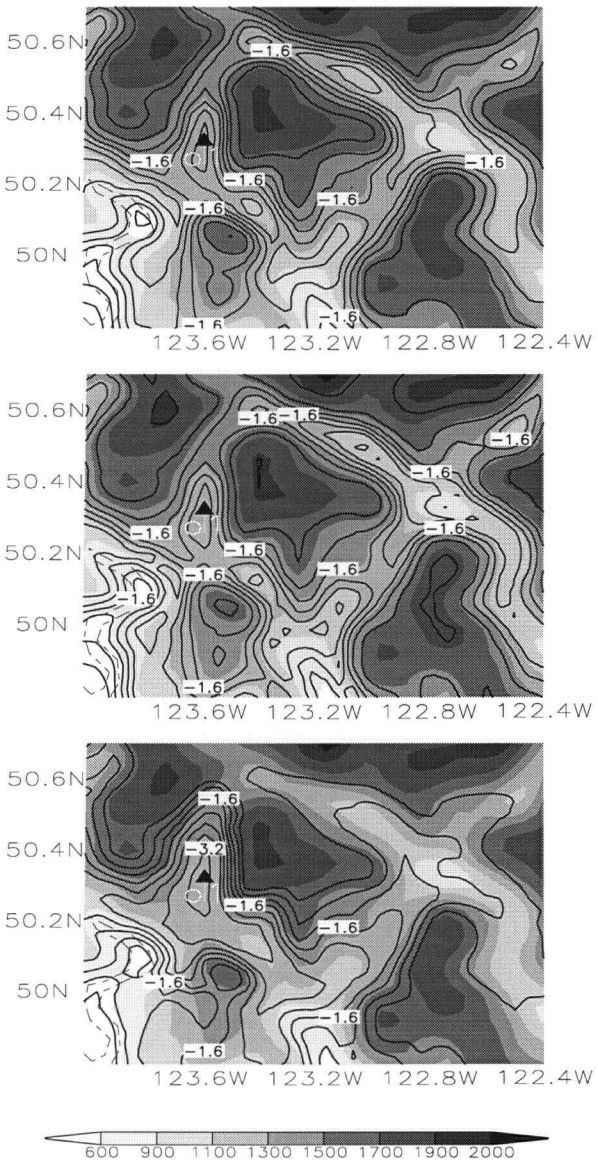

Figure 4.3: Analysis increments (isopleths) for potential temperature at the lowest model level in response to a single surface potential-temperature observation at station o1 indicated by a solid triangle. Contour interval is 0.3 K. Darker shading indicates higher elevations, with a maximum elevation difference of 1940 m, which is less than that in Fig. 4.1 because of the smoothed terrain used in the NWP model. (top) GAUSS, (middle) TERR_DIFF, (bottom) MD.

Figure 4.3 shows the impact of o1 on the GP analysis. The observation increment is -3.35 K. The Bratseth analysis is confined to a single pass for convergence in the presence of a single perfect observation. All the analysis methods show that the observation mostly influences the valley GPs.

GAUSS and TERR_DIFF both yield large AIs in valleys disconnected from the Elaho River Valley, even though both valleys may not necessarily share the same air mass. The Lillooet River Valley (containing b1, Fig. 4.1) is such an example. In MD, the large AIs are in the Elaho River Valley (containing o1), with much smaller values in the Lillooet River Valley, as desired.

4.2.2 Impact of two surface observations from different valleys

The analysis at one GP using observations from adjacent but disconnected valleys, where each valley contains a different meteorological regime, is a typical problem in complex terrain. To examine this, consider two observations in different valleys (stations o1 and o2 in Fig. 4.1). The observation at o1 is 3.35 K colder than the first guess, while the observation at o2 is 3.36 K warmer. Four stations (b1, b2, b3, and b4) in the Lillooet River Valley are used to verify the analyses.

First, only the observation at o2 is used. To evaluate different analysis methods, the GP analyses are interpolated to the four verifying stations (not collocated with any GP) by cubic polynomial interpolation. The root-mean-square error (rmse) between the observations and analyses at those sites are calculated. For comparison purposes, the parameters for GAUSS (R_z = 500 m), TERR_DIFF (K_z = 7.0 x 10^{-6} m^{-2}) and MD (a = 2, b = 2, $zref1$ = 750 m, $zref2$ = 750 m) are chosen so that the three methods produce similar rmses. The values of these parameters are kept fixed for all subsequent experiments throughout this dissertation.

Rmses for GAUSS, TERR_DIFF, and MD are 0.6179, 0.6468 and 0.6559 K, respectively. Rmses for these three methods are slightly greater than that between the observations and the first guess, which is 0.5395 K. The analyses and the first guess versus the observations for the three methods are shown in the left-hand panel of Fig. 4.4. It is evident that the three methods produce similar analyses.

The observations from both sites (o1 and o2) are then used to produce an analysis. While the same set of observations at b1, b2, b3, and b4 are used for verification. The additional observation at o1 has a negative impact on both the GAUSS and TERR_DIFF analyses (see the right-hand panel of Fig. 4.4). Rmse increases to 2.1464 K for GAUSS and 2.4380 K for TERR_DIFF. However, in MD, the additional observation at o1 has a minor impact on the analyses at the verifying stations, as desired because the two valleys with observations are not strongly coupled. The slight influence from the added observation reduces the rmse to 0.4807 K. The rmse with two observations is reduced about 11% from the first guess.

4.2.3 Impact of a single mountain-top surface observation

In complex terrain, most surface observation sites are located in populated valleys. There are, however, some surface stations located at high elevations in the mountains, such as at

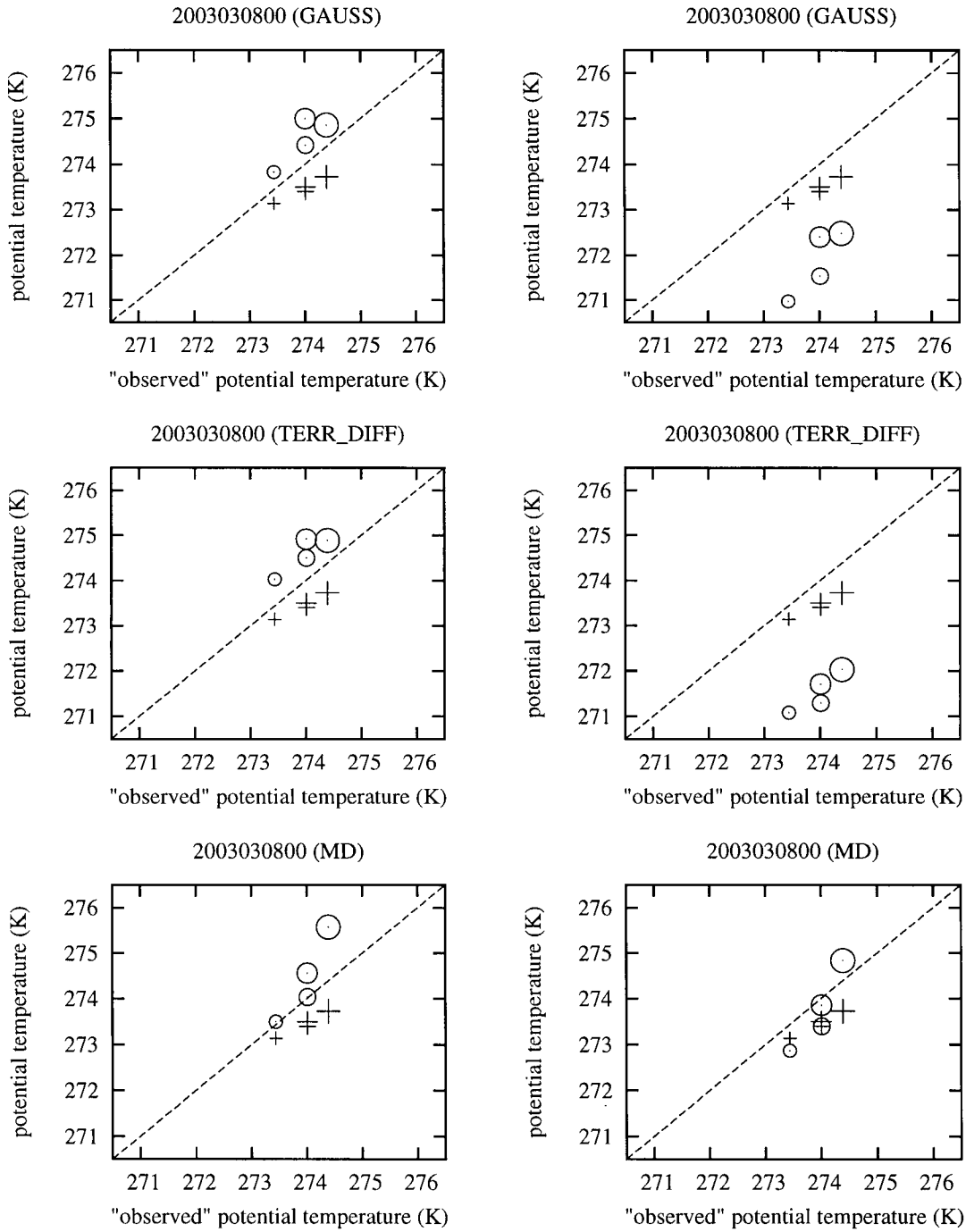

Figure 4.4: Analysis, indicated by a circle, and first guess, indicated by a plus, vs observation. (left column) Observation at o2 only is used in the analysis. (right column) Observations at both o1 and o2 are used in the analysis. (top) GAUSS; (middle) TERR_DIFF; (bottom) MD. The four points (circles or pluses) correspond to the four verifying stations b1-b4.

ski areas and in subalpine forest ecosystems. This subsection examines the analysis impact of a single mountain-top observation.

Figure 4.5 shows the AIs produced by o3 (elevation: 1954 m). The observation increment is -1.56 K. As desired, all methods produce minimal spread into valley GPs, with MD producing very small spread into the valleys.

For GAUSS and TERR_DIFF, the observation increment is spread to all of the surrounding high mountains, including those separated by deep valleys. In MD, the observation corrects the first guess only for those GPs on the same mountain as o3. The GAUSS and TERR_DIFF analysis increments in Fig. 4.5 look more realistic than the unrefined MD for two reasons. During shallow cold-air pooling events, the high-mountain tops are all penetrating into the free atmosphere, where they would experience the same weather. Second, during deep BL events with BL top above the mountain top, vigorous turbulence would also cause mixing across the valleys.

To allow such spreading, the MD approach was refined to spread free-atmosphere mountain-top observations differently than valley observations (see section 3.5.2). The AIs produced by o3 from method MD_MT (the MD after mountain-top refinement) are shown in Fig. 4.6. The MD approach after mountain-top refinement now spreads the mountain-top observation increment to all of the surrounding high mountains, while gives very small spread in the valleys. The amount of spread to neighboring mountain tops is not uniform, but still decreases horizontally with the usual Gaussian drop-off.

Table 4.2 lists the normalized rmses (nrmses) between different sets of the virtual surface observations (see Fig. 4.7) and the analyses using the different methods, when only the single mountain-top observation o3 is used to produce an analysis. The observation increment is -1.56 K. The second column in Table 4.2 indicates that methods MD and MD_MT produce very small spread [namely very small correction applied to the first guess (FSTG)] from the mountain-top observation into valleys as expected. As shown in the third column, methods GAUSS and TERR_DIFF reduce rmses from the first guess by spreading the observation increment into surrounding high mountains. Method MD produces identical rmse as the first guess. While allowing spread into the surrounding high ridges, method MD_MT reduces the nrmse from 1.0 to 0.1633, compared to method MD.

Table 4.3 lists the verification summary when the three observations (two valley observations o1 and o2, and one mountain-top observation o3) are used to produce an analysis. The verification is done for independent valley observations (b1, b2, b3 and b4) and mountain-top observations (m1, m2 and m3) shown in Fig. 4.7. The GAUSS and TERR_DIFF analyses degrade the first guess and have nrmses greater than 1.0. The analysis from method MD is better than the first guess. Method MD_MT has minimum nrmse and thus produces the best analysis.

4.3 Experiments using real observations

The MD approaches are tested with real observations in the coastal terrain of the Georgia Basin, BC, in this section, and with real observations in the inland mountainous region (see section 6.1). Hourly surface observations are from the Emergency Weather Net Canada (described in section 2.3). The higher density of observations over the Georgia Basin (Fig. 4.8) allows us to withhold some stations for verification (Table 4.4). The land-sea

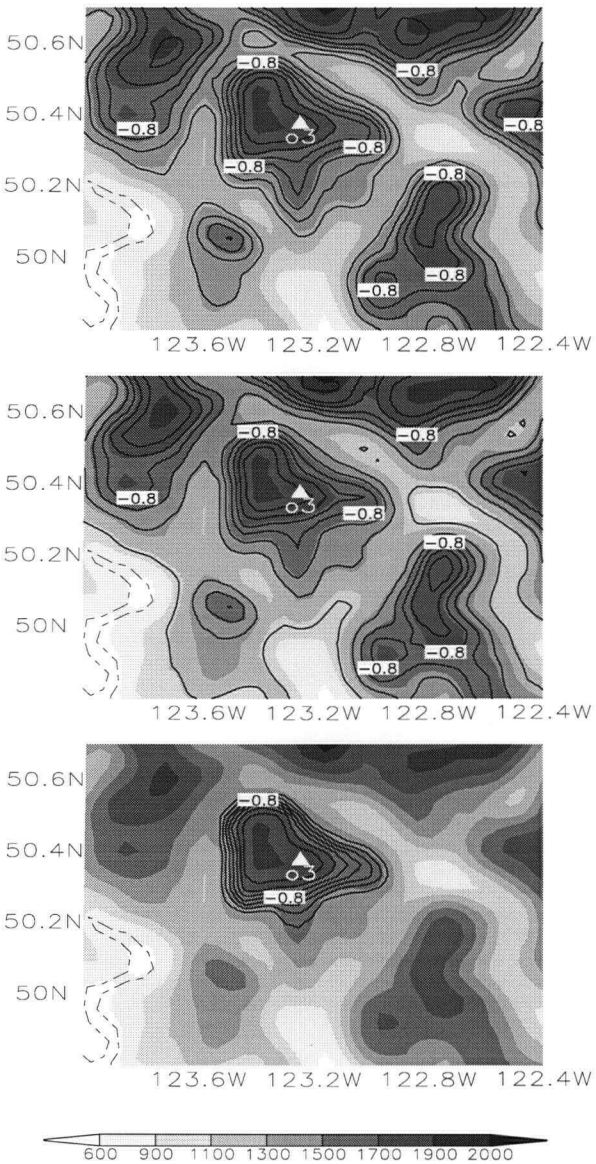

Figure 4.5: Analysis increments (isopleths) for potential temperature at the lowest (terrain-following) model level in response to a single mountain-top observation at o3, indicated by a white solid triangle. Contour interval is 0.2 K. Darker shading indicates higher elevations (m). (top) GAUSS; (middle) TERR_DIFF; (bottom) MD.

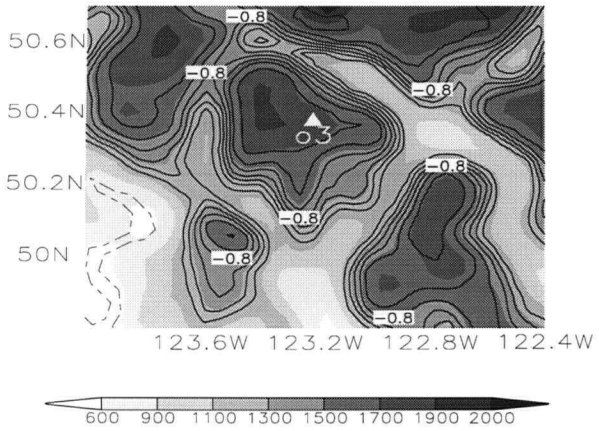

Figure 4.6: Analysis increments (isopleths) from method MD_MT for potential temperature at the lowest (terrain-following) model level in response to a single mountain-top observation at o3, indicated by a white solid triangle. Contour interval is 0.2 K. Darker shading indicates higher elevations (m).

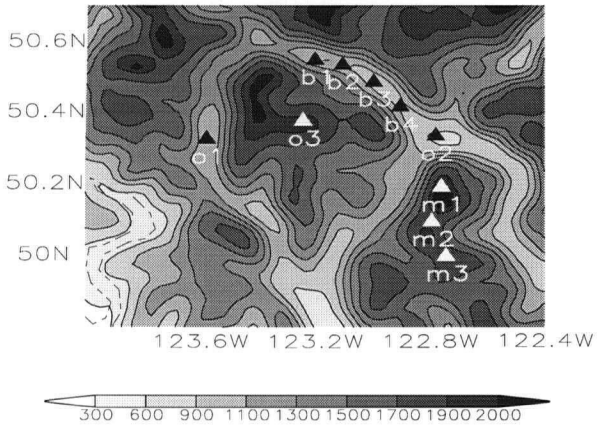

Figure 4.7: Virtual surface observation stations, indicated by solid triangles, used in the analysis and verification. The stations are positioned at the truth-model terrain height in the Coast Mountains north of Vancouver. Station o1 (50.326 °N, 123.578 °W) is near the mouth of the Elaho River. Station o2 (50.3344 °N, 122.767 °W) is near the town of Pemberton. Station o3 (50.3773 °N, 123.2363 °W) is over the mountain top. Terrain elevations (m) are from the truth model. Darker shading indicates higher elevations, with a maximum elevation difference of 2055 m in this figure.

Table 4.2: The normalized root-mean-square errors (nrmses) between the analyses and observations for different sets of the verification stations. One set is the valley observations (b1, b2, b3 and b4); the other is the mountain-top observations (m1, m2 and m3). The analyses were produced when only the single mountain-top observation o3 is used. The observation stations are shown in Fig. 4.7. Nrmse is rmse for each method normalized by the rmse of the first guess (FSTG). Smaller nrmse corresponds to better analyses. Nrmse close to 1.0 indicates very small correction to the first guess from the observations.

Method	**Verified against b1, b2, b3 and b4**	**Verified against m1, m2 and m3**
FSTG	1.0	1.0
GAUSS	1.1025	0.2745
TERR_DIFF	1.4061	0.2143
MD	1.0009	1.0
MD_MT	1.0026	0.1633

Table 4.3: Same as Table 4.2, but for all of the verification stations (the valley stations b1, b2, b3 and b4, and the mountain-top stations m1, m2 and m3). The analyses were produced using two observations (o1 and o2) in different valleys and one mountain-top observation o3.

Method	**Verified against b1, b2, b3, b4, m1, m2 and m3**
FSTG	1.0
GAUSS	1.7593
TERR_DIFF	1.9668
MD	0.9720
MD_MT	0.4147

mask is based on the model-resolved coastlines. The ratio of observation-error variance to background-error variance is set to 0.08 as in Miller and Benjamin (1992). The low observation-to-background error implies that the observations are heavily weighted. The value of the ratio (0.08) is used throughout this dissertation whenever real observations are used in numerical experiments.

A 3-4 February 2003 case, characterized by a strong ridge over the Georgia Basin, is used to examine if weak land-sea thermal contrasts can be properly analyzed. Figure 4.9 shows the evolution of potential temperatures for several surface stations on land and water during 0000-1200 UTC 4 February 2003. In late afternoon at 0000 UTC (1600 PST), all land stations except Vancouver INTL ARPT were slightly warmer than the water stations. After a transition period from 0100 to 0300 UTC, all land stations were colder than the water stations. Land-sea thermal contrast is the most prominent in early morning at 1200 UTC (0400 PST).

The Eta analysis and forecasts from NCEP, valid at 0000 UTC 3 February 2003, are used to drive the coarsest grid (108-km grid spacing), which in turn drives grids of 36, 12, 4, and 3 km. MC2 at 3 km provides first-guess fields, and is started at 1200 UTC 3 February from MC2 4-km output. Analyses are performed every hour from 0000 to 1200 UTC 4 February, by blending hourly surface observations with the first guess at the lowest terrain-following model level valid at the same time. The hourly analyses are not incorporated into the forecast cycle; thus, each analysis is independent of past observations. Eight stations are used for analysis and eleven others for verification (Table 4.4), but the available number of reporting stations varies with the analysis time (Table 4.5).

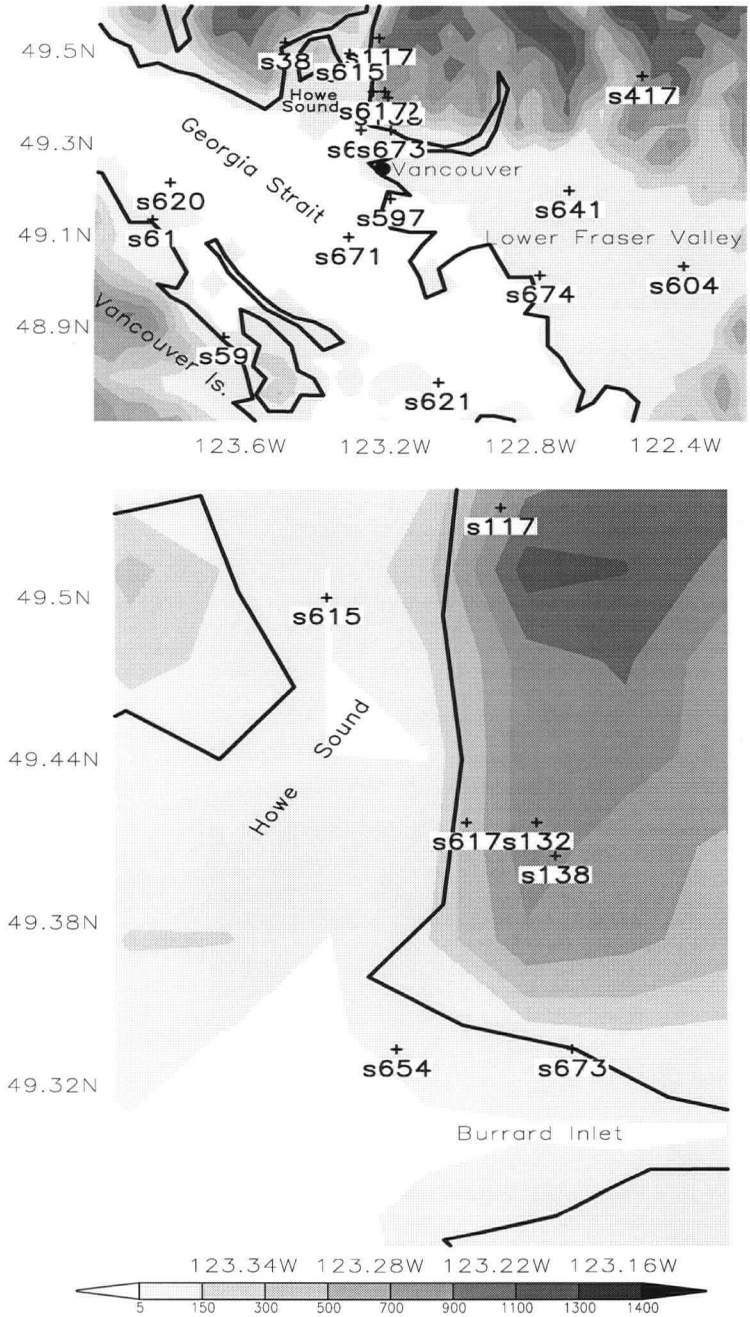

Figure 4.8: The northern half of the Georgia Basin area. The surface stations are shown by pluses, below which are station IDs. Station information is in Table 4.4. The bottom plot is zoomed to the top center of the top plot. Terrain elevation (m), indicated by shading, are from unsmoothed terrain data resolved by the NWP model at 3-km grid spacing. Darker shading represents higher elevations, with a maximum elevation difference of (top) 1374 m and (bottom) 1200 m.

Table 4.4: Surface stations for analysis and verification. Station IDs are from the Emergency Weather Net database. For the land-sea (LS) mask, 1 stands for land and 0 corresponds to ocean or water. The first eight stations are used for analysis, while the rest are used for verification.

Full name	**Station ID**	**Lat (°N)**	**Lon (°W)**	**Elev (m)**	**Agency**	**LS**
Port Mellon	38	49.5228	123.4822	3.	WLAP	1
MT Strachan	132	49.4167	123.2000	1420.	MOT	1
Gold CK.	417	49.4472	122.4750	794.	HYDR	1
Abbotsford ARPT	604	49.0333	122.3667	58.	EC	1
Saturna Island	621	48.7833	123.0500	24.	EC	0
Pitt Meadows	641	49.2000	122.6833	5.	EC	1
Point Atkinson CS	654	49.3333	123.2667	35.	EC	0
Nanaimo ARPT	582	49.0500	123.8667	28.	EC	1
Crofton	59	48.8803	123.6458	20.	WLAP	0
Harmac Pacific	61	49.1353	123.8475	23.	WLAP	0
Deeks Peak	117	49.5333	123.2167	1280.	MOT	1
MT Strachan Precip	138	49.4044	123.1911	1220.	MOT	1
Vancouver INTL ARPT	597	49.1833	123.1833	2.	EC	1
Pam Rocks	615	49.5000	123.3000	10.	EC	0
Discovery Island CS	617	49.4167	123.2333	15.	EC	1
Entrance Island	620	49.2167	123.8000	3.	EC	0
Sand Heads CS	671	49.1000	123.3000	15.	EC	0
West Vancouver	673	49.3333	123.1833	178.	EC	1
White Rock	674	49.0167	122.7667	13.	EC	1

Table 4.5: Number of reporting stations for analysis and verification at each analysis time on 4 Feb 2003.

	No. of stations	
Time (UTC)	**Analysis**	**Verification**
0000	8	11
0100	8	11
0200	8	11
0300	8	11
0400	4	7
0500	7	11
0600	6	11
0700	7	11
0800	7	11
0900	7	11
1000	7	11
1100	7	11
1200	7	11

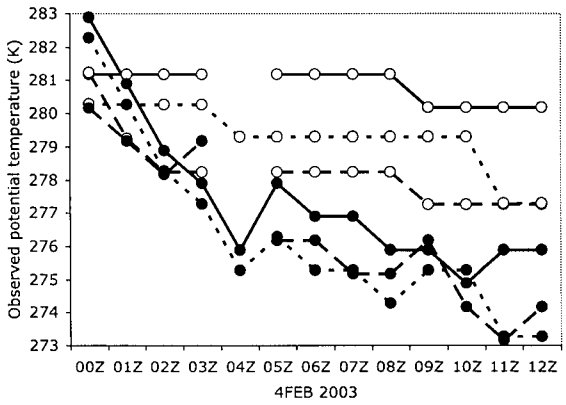

Figure 4.9: Observed potential temperature (derived from observed temperature) for stations over water (lines with open circles) and over land (lines with filled circles) during 0000 UTC-1200 UTC 4 Feb 2003. Stations over water are Entrance Island (620, solid line), Pam Rocks (615, dashed line), and Sand Heads CS (671, dotted line). Stations over land are West Vancouver (673, solid line), Vancouver INTL ARPT (597, dashed line) and White Rock (674, dotted line). Breaks in the graph denote periods for which no observations were reported. 0000 UTC (00Z) corresponds to 1600 PST (late afternoon), and 1200 UTC (12Z) is 0400 PST (early morning).

Figure 4.10 shows time series of the first guess (FSTG) or the analyzed potential temperature and observations for one water station (Entrance Island) and one land station (White Rock), separately. The 3-km run produces a good first guess for White Rock from 0300 to 1200 UTC 4 February, but underpredicts the potential temperatures for Entrance Island. The analyses from four methods (not including MD_MT because there are no mountain-top stations in this data set) show more agreement with the observations than the first guess. Comparatively, MD and MD_LSMG both produce better analyses than GAUSS and TERR_DIFF. MD_LSMG is superior in maintaining the thermal contrast between Entrance Island and White Rock. Figure 4.11 further demonstrates advantages of MD_LSMG, based on separate averages from three land and three water stations. Averaging all land stations, including the slope stations, makes the land-water contrast very small. However, advantages of MD_LSMG can be seen from separate averages of all water stations and all land stations except the slope stations (not shown).

As mentioned before, the land-sea thermal contrast in early morning at 1200 UTC is the most prominent during the study period. Observed potential temperatures at 1200 UTC 4 February 2003 are presented in Fig. 4.12, which shows thermal gradients across coastlines (i.e., relatively cold over the Lower Fraser Valley and warm over the Strait of Georgia). High potential temperatures are also observed over the mountain slopes north of Vancouver.

Figure 4.13 shows how much the analysis from each of the four methods corrects the first guess by assimilating surface potential temperature observations. Methods GAUSS and TERR_DIFF exhibit similar results: over-correction for observed potential temperature less than 278 K (mostly stations along coastlines over the Lower Fraser Valley) and under-correction for observed potential temperature greater than 278 K (stations over the

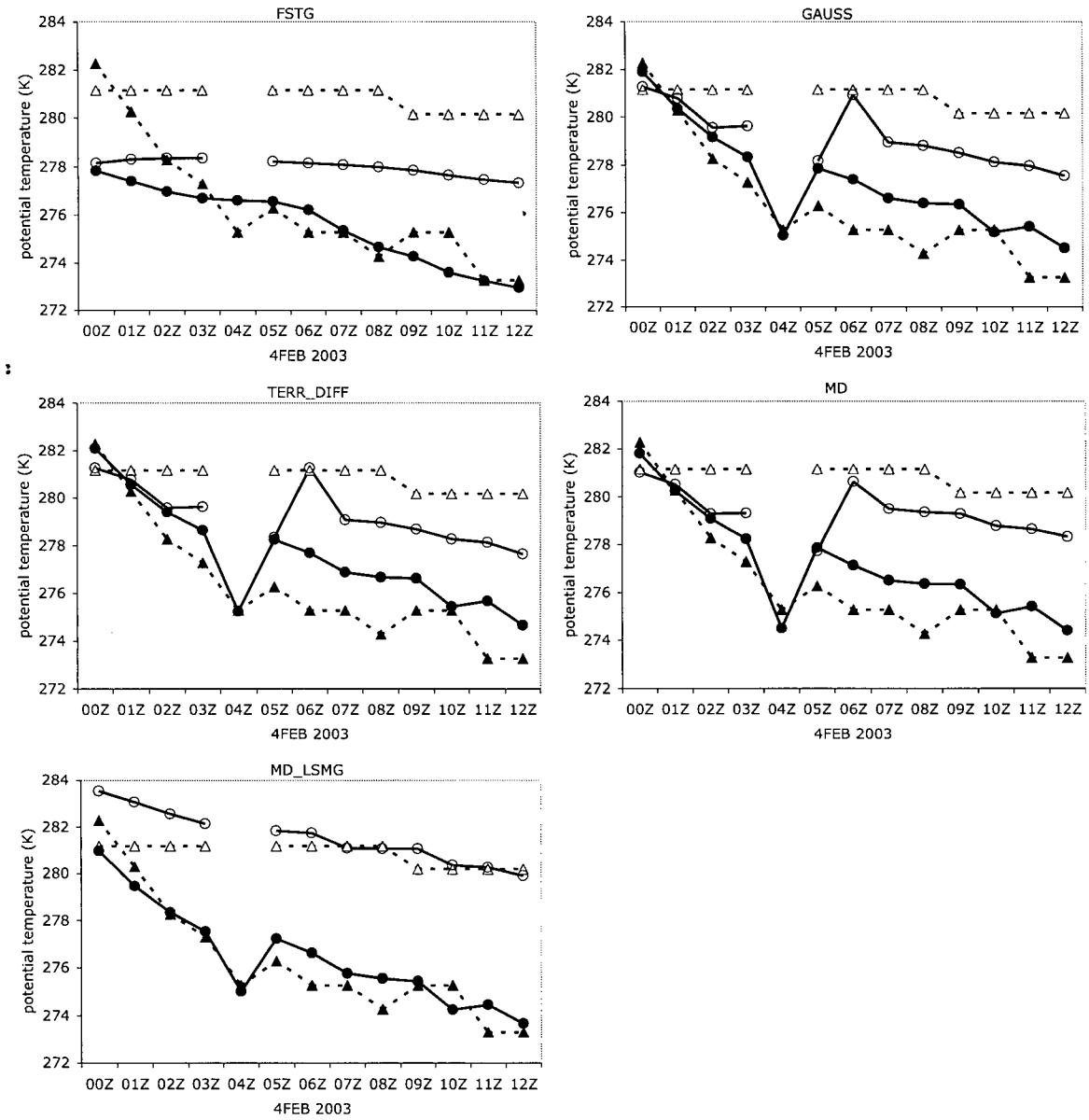

Figure 4.10: Time series of observed potential temperature and the [first guess (FSTG) or analyzed] potential temperature from four analysis methods for two stations. Observations at Entrance Island over water: dashed line with open triangles. Observations at White Rock over land: dashed line with solid triangles. Analyses at Entrance Island: solid line with open circles. Analyses at White Rock: solid line with filled circles. Analyses are better when the solid lines are closer to the respective dashed lines.

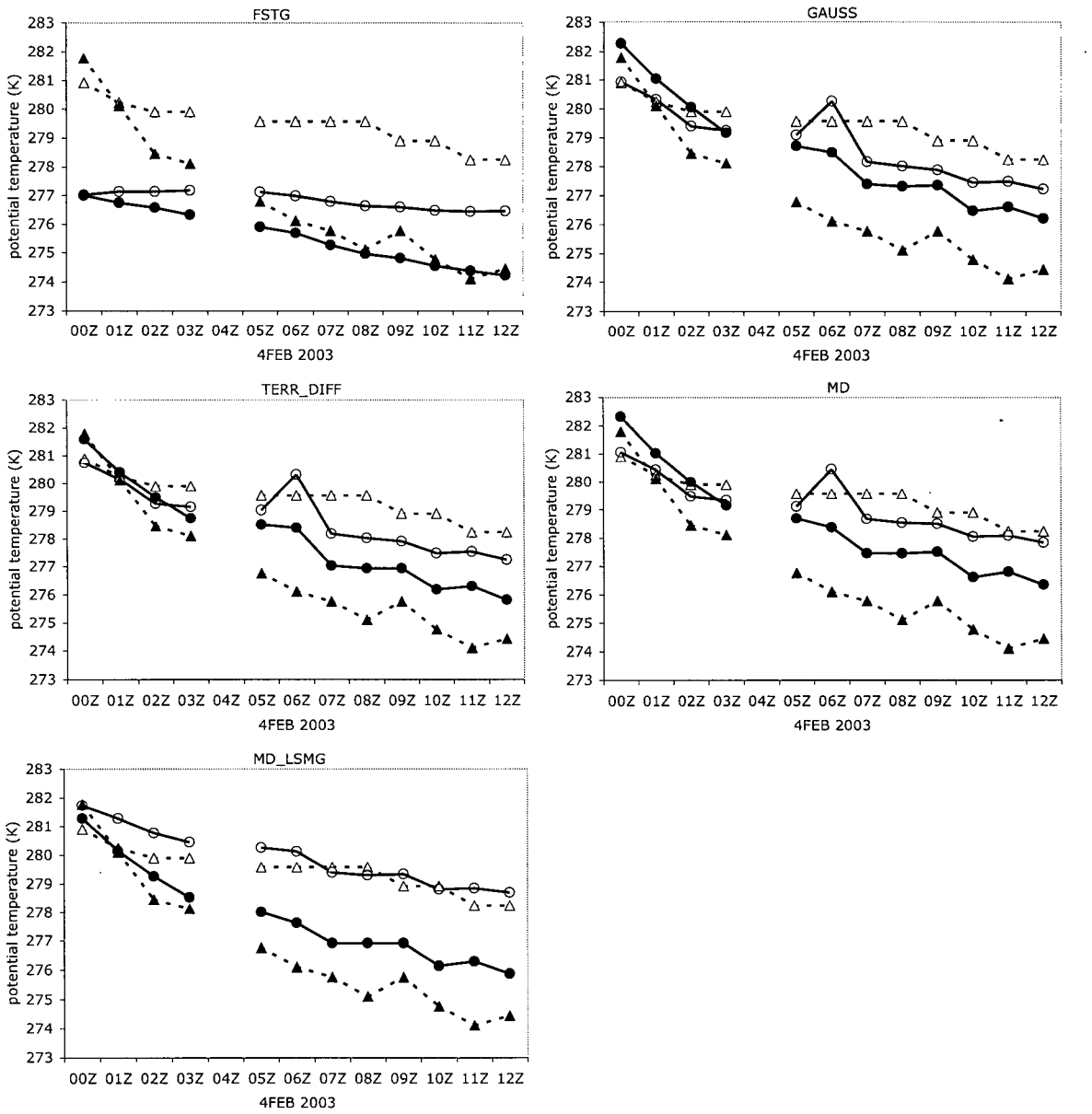

Figure 4.11: Time series of averaged potential temperature of three stations over water and land, respectively. The three stations over water, used for the average, are Entrance Island, Pam Rocks and Sand Heads CS. West Vancouver, Vancouver INTL ARPT and White Rock are the three stations used for the average over land. Observations and analyses over water are denoted by the dashed line with open triangles and the solid line with open circles, respectively. Observations and analyses over land are represented by dashed line with solid triangles, and solid line with filled circles, respectively. FSTG stands for the first guess. Closer correspondence between the solid and dashed lines indicate a better analysis.

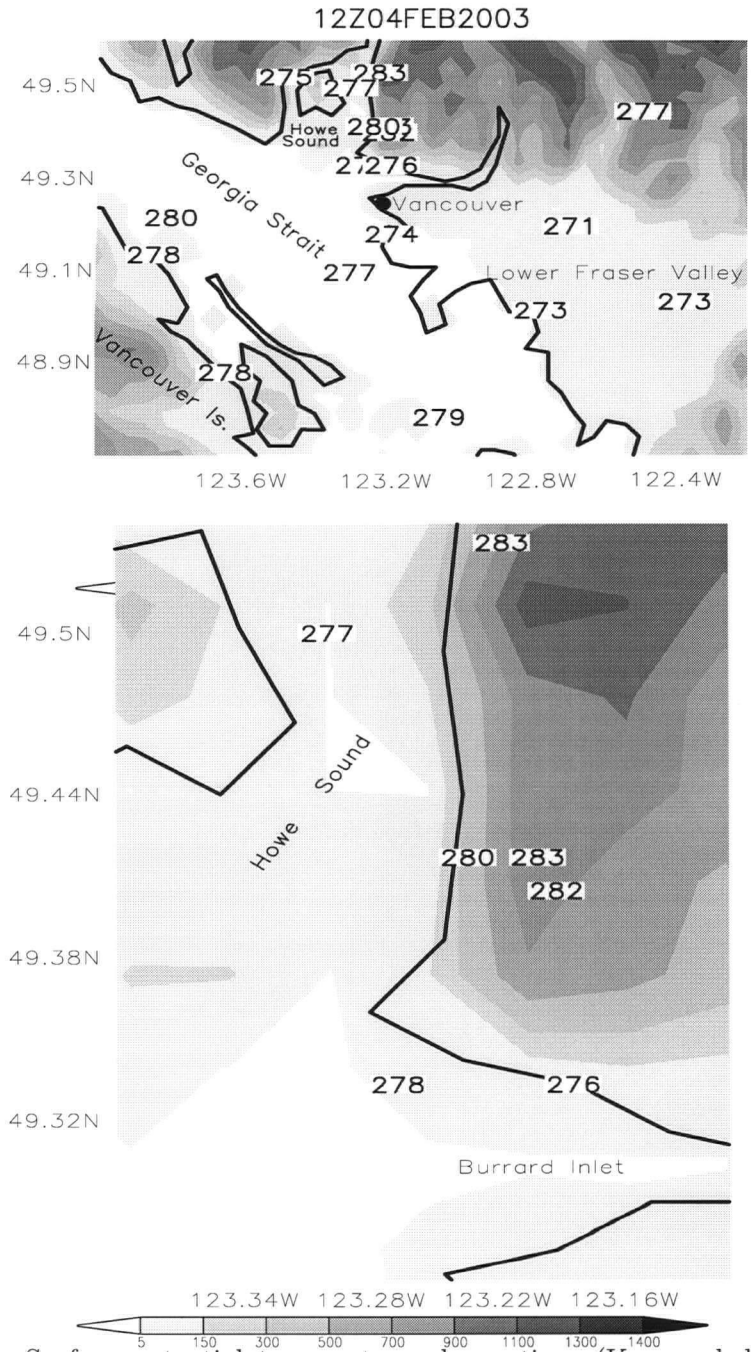

Figure 4.12: Surface potential temperature observations (K; rounded to be integer for plotting) over the Georgia Basin area at 1200 UTC 4 Feb 2003. The corresponding station IDs can be found in Fig. 4.8. The bottom plot is zoomed to the top center of the top plot. Higher elevations are shaded darker (see gray reference bar in units of meters).

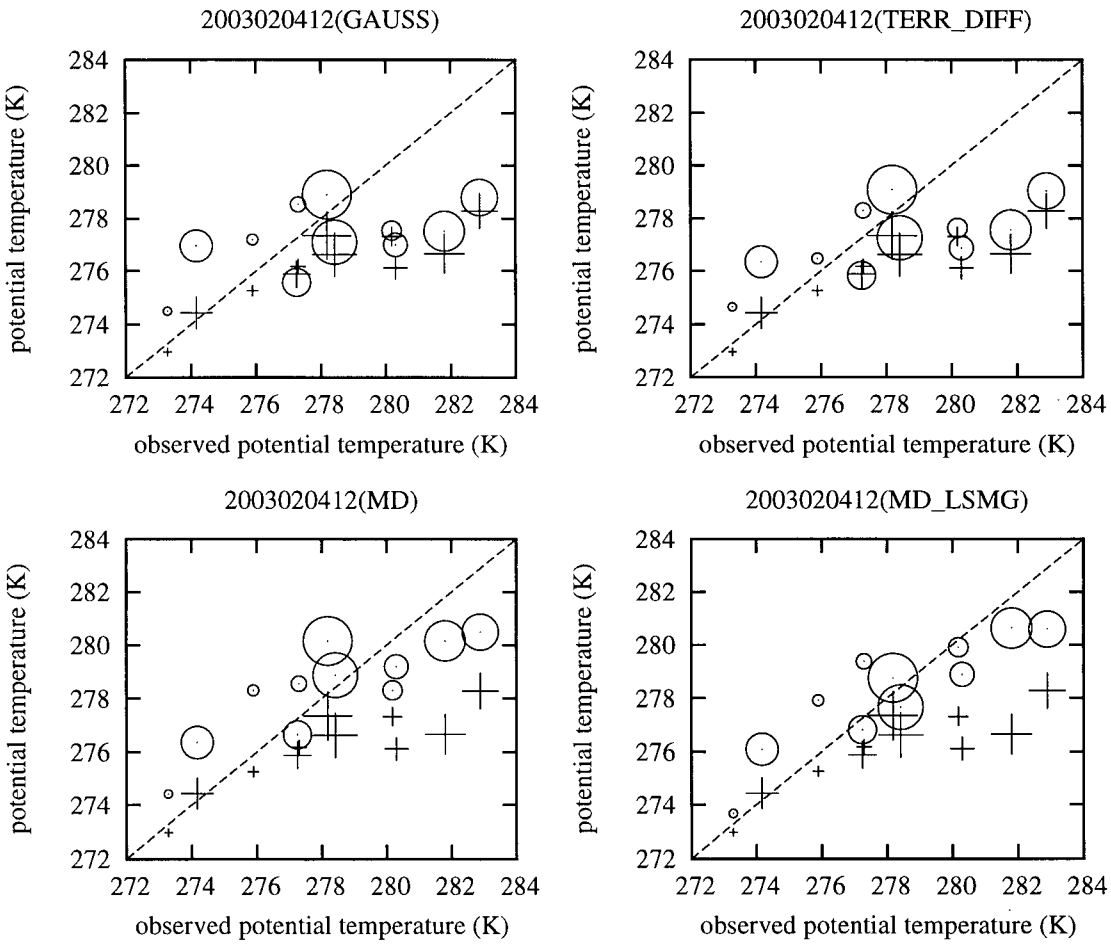

Figure 4.13: The first guess, indicated by a plus, and analysis, indicated by a circle, from each of the four methods (GAUSS, TERR_DIFF, MD, MD_LSMG), vs observation. Perfect analysis is along the diagonal. The size of circles and pluses is increased with the following sequence of stations: s674, s673, s671, s620, s617, s615, s597, s117, s138, s61, s59. See station locations in Fig. 4.8.

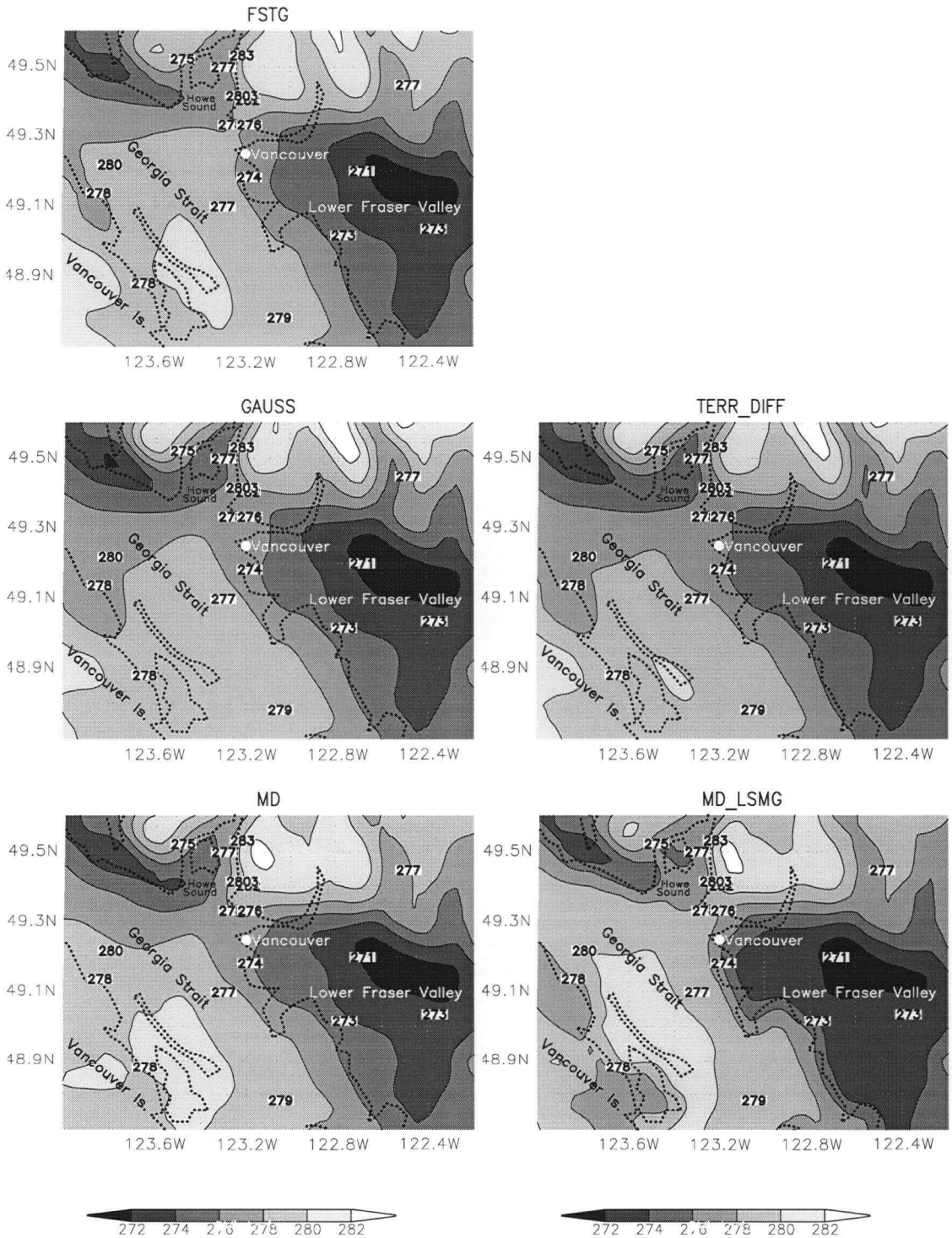

Figure 4.14: The first guess (FSTG) and analyzed potential temperature (K) from each of the four analysis methods (GAUSS, TERR_DIFF, MD, and MD_LSMG), as shown by shading. Darker shading indicates colder temperatures. Superposed are observed potential temperatures as shown by digital values for all stations. The analyzed and observed potential temperature are available at 1200 UTC 4 Feb 2003.

Table 4.6: Verification of analyzed potential temperatures in terms of bias, mean absolute error (mae), and normalized root-mean-square error (nrmse) for all reporting verification stations during the analysis period from 0000 UTC to 1200 UTC 4 Feb 2003. N equals number of stations times the number of observation times. Nrmse is rmse (root-mean-square error) for each method normalized by the rmse of the first guess (FSTG). Percent improvement of the rmse is with respect to FSTG.

Method	**N**	**Bias (K)**	**Mae(K)**	**Nrmse**	**Percent improvement**
FSTG	139	-2.6832	2.7624	1.	0
GAUSS	139	-0.5625	1.7565	0.6610	34
TERR_DIFF	139	-0.6401	1.6482	0.6317	37
MD	139	0.2344	1.3069	0.4943	51
MD_LSMG	139	-0.0051	1.1956	0.4433	56

mountain slopes of West Vancouver or over the Georgia Strait). Compared to GAUSS and TERR_DIFF, results from method MD show more agreement with observed potential temperature greater than 278 K. This reveals that MD accounts for terrain effects better than GAUSS and TERR_DIFF. Method MD_LSMG gives better analyses than MD, with reduced differences between the analyses and observations for almost all stations. Comparatively, the mother-daughter approaches (both MD and MD_LSMG) produce better analysis results than GAUSS and TERR_DIFF. MD_LSMG is superior in maintaining thermal contrasts across coastlines (for example, the coastline between the Georgia Strait and the Lower Fraser Valley), as can be seen in Fig. 4.14, which shows a better defined warm band over the Georgia Strait from MD_LSMG than from FSTG and any other analysis methods including GAUSS, TERR_DIFF, and MD.

To gain further insight into the performance of each analysis method, it is useful to look at the verification statistics for the whole analysis period. As shown in Table 4.6 and in Fig. 4.15, all methods improve FSTG as measured by bias, mean absolute error (mae) and normalized root-mean-square error (nrmse). TERR_DIFF is slightly better than GAUSS, with smaller mae and nrmse. MD is better than GAUSS and TERR_DIFF, and MD_LSMG is the best. Percentage improvement of rmse over FSTG is below 40% for GAUSS and TERR_DIFF, but above 50% for MD and MD_LSMG. Compared to MD, MD_LSMG gains 5% more improvement.

To compare computational efficiency, each method is executed on one processor of a High-Performance Computing Linux Super-Cluster, with 1 GHz Pentium III CPU. The

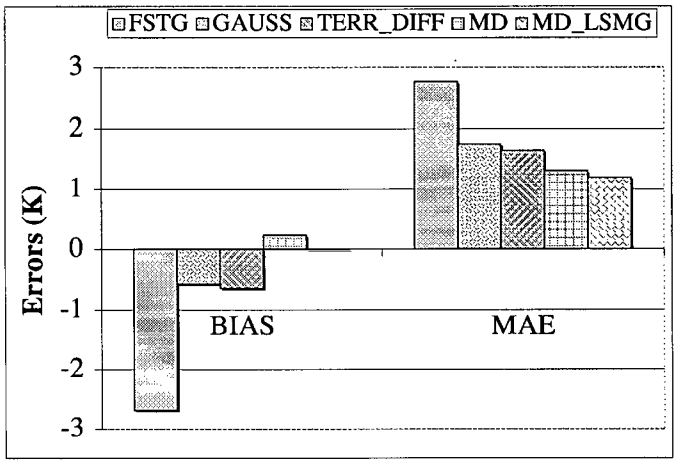

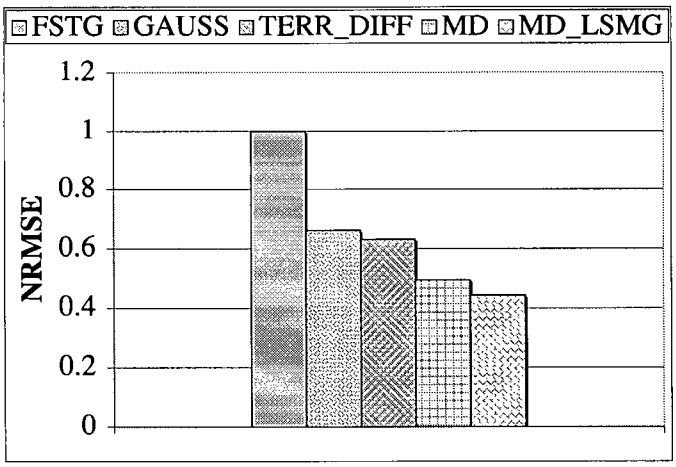

Figure 4.15: Verification of analyzed potential temperatures in terms of bias, mean absolute error (mae), and normalized root-mean-square error (nrmse) for all reporting verification stations during the analysis period from 0000 UTC to 1200 UTC 4 Feb 2003. Nrmse is rmse (root-mean-square error) for each method normalized by the rmse of the first guess (FSTG).

results from a surface-only analysis at 0100 UTC 4 February 2003 are presented in Table 4.7. For the purpose of computational comparison, all 169 available temperature observations are used within a domain having 257 x 205 = 52685 GPs, with 3-km grid spacing. The execution time for GAUSS is slightly less than that for TERR_DIFF. The execution time for the MD approach is split into two parts: 1) the calculation of the SFs (which needs to be done only once for each surface station within an analysis domain, as mentioned in section 3.3) and 2) the application of the SFs during the analysis (which is repeated for each analysis). Part 1 of both MD and MD_LSMG is computationally more expensive compared to GAUSS and TERR_DIFF, while part 2 is nearly the same as TERR_DIFF. MD_LSMG is computationally cheaper than MD, because adding land-water contrasts limits the region of influence and hence speeds computation. The timing for part 1 is done without limiting the observation's influence region. Thus, the computational costs are affected by the domain size.

To eliminate the domain-size effect, the SFs are re-calculated within a prescribed influence region (a square here) of the observation. The radius of the circle inscribed in the square was set to 300 km, which is slightly greater than the radius of influence (ROI; 273.14 km) calculated in the ADAS based on R_h for the first pass. Now the execution time for calculating the SFs is reduced 36.5% for MD and 33% for MD_LSMG [see item ($\star$) in Table 4.7].

Table 4.7: Execution time in seconds for each analysis method on one processor of a High-Performance Computing Linux Super-Cluster, with 1 GHz Pentium III CPU. The results are obtained from a surface-only analysis at 0100 UTC 4 Feb 2003, when all 169 observations are used for analysis within a domain of 257 x 205 grid points, with 3-km grid spacing. The parameters used in the mother-daughter approach are: $a = 2$, $b = 2$, $zref1 = 750$ m, and $zref2 = 750$ m. For the two MD approaches, item 1 is the one-time setup cost without limiting search radius, item 2 is the execution time for its application to this test domain, item $\star$ is also the one-time setup cost but with limiting search radius to 300 km.

Method		**Execution time (s)**
GAUSS		22.99
TERR_DIFF		28.12
MD	(1)	3902.03
	(2)	29.96
	($\star$)	2476.80
MD_LSMG	(1)	2833.89
	(2)	29.93
	($\star$)	1897.60

Chapter 5

Methodology for Assimilating Surface Observations into NWP models

5.1 Combination of surface and upper-air data

Dense surface observations are valuable data sources for mesoscale data assimilation (Stauffer et al. 1991; Ruggiero et al. 1996, 2000). However, surface observations are available at only one terrain-following level. Meanwhile, major operational centers generate 3-D meteorological analyses daily by assimilating many types of measurements. One example is the Eta model analysis from NCEP (see Appendix A). This chapter describes how to effectively combine dense local surface data with a coarser, 3-D analysis from major operational centers.

5.1.1 Surface-data analysis

Surface observations are first analyzed by using the MD approach in conjunction with the ADAS to generate a surface-data analysis (see Chapters 2, 3, and 4). This is done by optimally combining surface observations and the first guess. The first guess is a previous forecast (on the lowest terrain-following level) from the MC2 model at 3-km grid spacing (or 2-km grid spacing for operational runs in Chapter7).

5.1.2 Upper-air analysis

The Eta model analysis from NCEP (see Appendix A) is used to provide pseudo upper-air data. The input fields for MC2 nesting runs (e.g., 3-km grid) need to be on terrain-following model levels. To obtain an upper-air analysis on the terrain-following MC2 3-km (or 2-km) model levels, the Eta model analysis is interpolated horizontally to 108 km and vertically to the MC2 108-km model levels, and MC2 108 km is integrated for 1 h. The 0-h and 1-h output from the MC2 108 km are used as initial and boundary conditions to drive MC2 36 km, which in turn drive 12, 4, and 3 km (or 2 km). MC2 3-km (or 2-km) output on terrain-following levels at 0 h are the upper-air data that are used below. By doing this, horizontal interpolation is gradual from coarse grid to finer grids, and

vertical interpolation is done at the terrain-following coordinate except the one from the Eta model analysis (pressure levels) to the MC2 108-km model levels. Therefore, interpolation errors particularly associated with the interpolation from pressure levels to terrain-following levels are minimized. Also, assimilating this interpolated Eta data makes it effective to incorporate all the satellite, radar, aircraft and rawinsonde data that were assimilated by NCEP.

5.1.3 Combination schemes

Now we have a surface-data analysis, an upper-air analysis, and the 3-D first guess from a previous MC2 3-km (or 2-km) forecast. The three sources of data are on the MC2 3-km (or 2-km) model levels. As mentioned in Chapter 1, there is a need to spread single-level surface information upward into several model layers. Two schemes are proposed below to combine the three data sources at the times when there are analyses, to form a final analysis that can be used to initialize the data-assimilation (DA) runs. The two schemes are based on the following assumptions, similar to the ones made by Yee and Jackson (1988):

- Surface observations are important in describing atmospheric state in the atmospheric boundary layer (BL).
- Coarser, 3-D analyses from major operational centers are important in providing information for atmospheric state above the BL.

The first scheme (SIGM) uses a sigmoidal function to influence the background above the lowest model level by vertically spreading the analysis increments from the lowest model level. The scheme assumes that the analysis increments at the lowest model level apply to the whole BL, considering similar forecast errors in the BL. Above the BL top, the final analysis is a weighted average of the MC2 first guess and the pseudo upper-air data interpolated from the NCEP Eta model analysis. A transition zone exists near the BL top. The BL depth used in this scheme is diagnosed from the first guess by Stull's transilient turbulence theory (TTT) mixing-potential approach (Stull 1993; Stull 1998b).

Let h be the BL depth, Z_g be the height of the grid point above the ground level, SG_{sa} and SG_{ua} be sigmoidal functions for surface analysis increments and upper-air analysis increments, respectively, then

$$SG_{sa}(r,k) = \mathrm{sgm}\left[\frac{h(r) - Z_g(r,k)}{K_t}\right] \tag{5.1}$$

$$SG_{ua}(r,k) = \mathrm{sgm}\left[\frac{Z_g(r,k) - h(r)}{K_t}\right] \tag{5.2}$$

where $\mathrm{sgm}(x) = 1/(1+\exp(-x))$, and parameter K_t (taken as 10. m here to restrict the influence of surface data within the BL) controls the sharpness of the sigmoidal functions near the BL top. Subscripts sa and ua represent the surface analysis and upper-air analysis, respectively. Indexes r and k correspond to horizontal position and vertical level. A boundary condition is applied at the lowest model level: $SG_{sa}(r,1) = 1.0$ and $SG_{ua}(r,1) = 0.0$. The two sigmoidal functions are illustrated in Fig. 5.1.

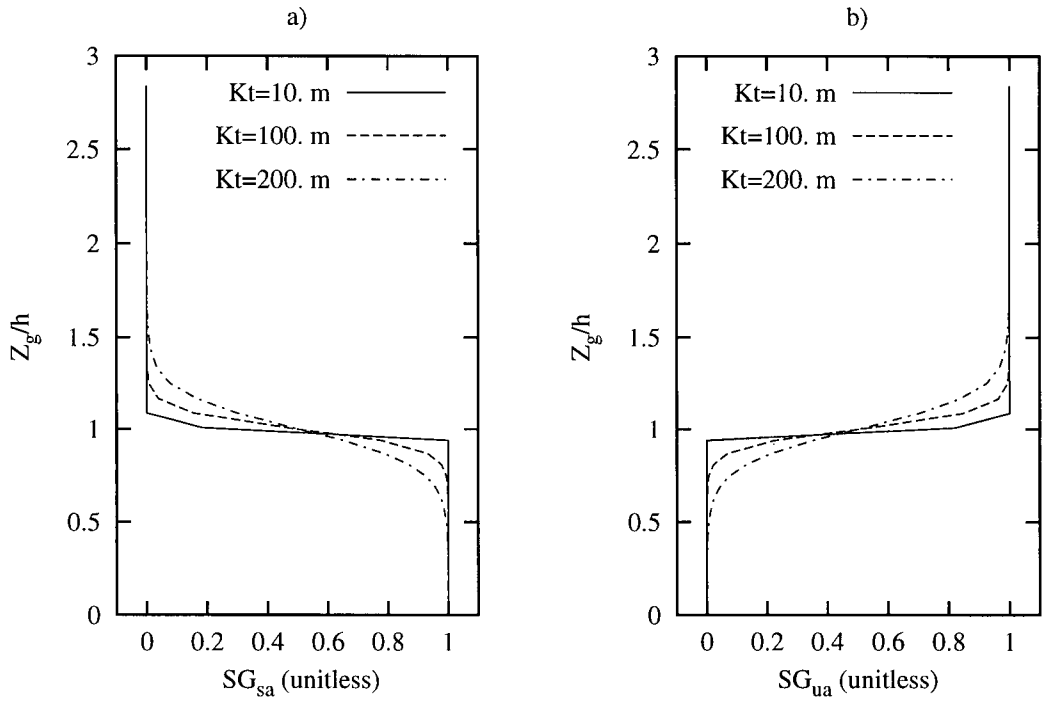

Figure 5.1: Illustration diagrams of the sigmoidal functions for a) surface analysis increments; b) upper-air analysis increments.

Let F be an analysis variable. The final analysis of F becomes

$$\begin{aligned} F^A(r,k) =& F^B(r,k) + SG_{sa}(r,k)\left[F^{SA}(r,1) - F^B(r,1)\right] \\ &+ SG_{ua}(r,k)W_{ua}(k)\left[F^{UA}(r,k) - F^B(r,k)\right] \end{aligned} \tag{5.3}$$

where superscripts A, B, SA and UA represent the final analysis, the background, surface analysis and upper-air analysis, respectively. Weights W_{ua} in (5.3) depend on the ratio of error variances of upper-air analysis and the background:

$$W_{ua}(k) = \frac{1}{1 + \left[\dfrac{\sigma^{UA}(k)}{\sigma^B(k)}\right]^2} \tag{5.4}$$

As the upper-air analysis is obtained by interpolating the Eta analysis to the MC2 3-km (or 2-km) model levels, the error variance for the upper-air analysis is assumed to be the same as that for the background: $\sigma^{UA}(k) = \sigma^B(k)$.

The second scheme is a profile (PROF) method, where potential temperature and specific humidity at the lowest model level are assumed to be mixed uniformly within the BL, so the potential temperature and specific humidity analysis at the lowest model level are applied to the whole BL. This assumption works well for unstable mixing layer, or stable mixed layer when strong winds, strong turbulence and weak surface cooling are present (Stull 1988). This assumption is not valid if a very stable layer exists near the

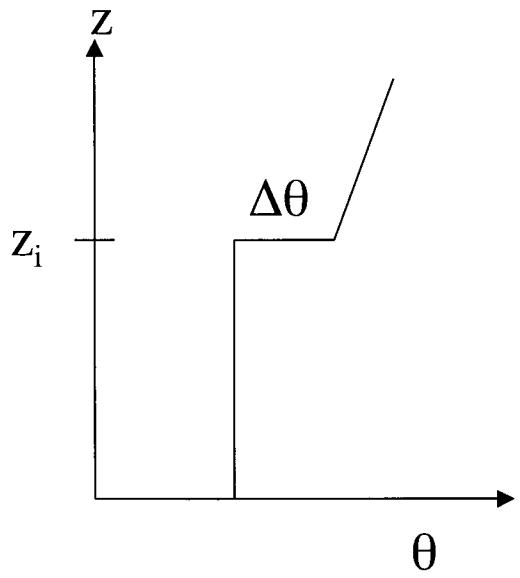

Figure 5.2: Illustration of a slab idealization of the mixed-layer potential temperature profile.

ground. In this thesis work, observations valid at 0000 UTC (1600 PST) are analyzed and assimilated into the NWP model. Above the BL top, the final analysis is a weighted average of the first guess and upper-air data as in SIGM. BL height is diagnosed from a profile method (described below) based on a slab idealization of the mixed layer (Stull 2000). A jump ($\Delta\theta$) of potential temperature at the entrainment zone is taken as 1.5 K. Figure 5.2 illustrates a slab idealization of the mixed layer.

In the profile method, the analyzed potential temperature at the lowest model level $\theta^{SA}(1)$ is compared with the potential temperature profile of the upper-air analysis (θ^{UA}) at successively higher grid points. When $\theta^{SA}(1) - \theta^{UA}(1) > -1.5$ K, the BL height Z_i is the height of the model level k at which the criterion of $\theta^{UA}(k) - \theta^{SA}(1) \geq 1.5$ K is first met. When $\theta^{SA}(1) - \theta^{UA}(1) \leq -1.5$ K, Z_i is assumed to be 300 m, which represents shallow BLs with cold-air pooling.

5.2 Insertion technique

The objective analysis procedures described in section 2.2 do not provide mass and motion fields that are in optimal balance to initiate a forecast. If the analysis is used directly as an initial condition, the initial imbalance between mass and motion fields can excite large, spurious inertial-gravity waves (IGWs). To reduce the effects of initial imbalances, a separate initialization step is usually utilized after analysis. According to Haltiner and Williams (1980): "The objective of an initialization procedure is to prepare gridpoint data with which the model can integrate forward in time with a minimum of noise and maximum accuracy of the forecasts of the meteorological scales that the model is designed to simulate." There are many initialization methods, such as damping techniques, static

initialization, normal-mode initialization, dynamic initialization and Newtonian relaxation. More details about these methods can be found in Haltiner and Williams (1980), and Kalnay (2003).

An explicit initialization process after analysis has become less popular recently, because alternative approaches have been developed. One approach is the incremental analysis updating (IAU) developed by Bloom et al. (1996). IAU combines aspects of the intermittent and continuous approaches, i.e., the analyses are intermittent, but the analysis increments are used as constant forcings in model's prognostic equations over an assimilation period centered on an analysis time (Bloom et al. 1996). Hence, in IAU, the analysis increments are incorporated gradually into a model, without the use of an explicit initialization process.

Once the final analysis is obtained as proposed in the previous section, incremental analysis updating (IAU, similar to Bloom et al. 1996) is used here to insert the final analysis increments (the differences between the final analysis and the first guess) into the MC2 model. A schematic of the data assimilation using the IAU technique is shown in Fig. 5.3.

In the MC2 model, different terms of the prognostic equations are combined during the numerical integration using a process-splitting method (Bergeron et al. 1994). The prognostic equation for any variable ψ can be expressed in symbolic form by

$$d_t\psi = \mathbf{L}(\psi) + \mathbf{R}(\psi) + \mathbf{E}(\psi) + \mathbf{P}(\psi) + \mathbf{H}(\psi) + \mathbf{T}(\psi) \tag{5.5}$$

where d_t is a total derivative, $\mathbf{L}(\psi)$ is the linear part of the gravity and elastic waves, and $\mathbf{R}(\psi)$ represents all the other dynamic terms. The $\mathbf{E}(\psi)$ term represents the nesting of the model variables with the driving model values near the lateral boundaries, $\mathbf{P}(\psi)$ are the physical parameterizations acting in the vertical, $\mathbf{H}(\psi)$ is horizontal diffusion, and $\mathbf{T}(\psi)$ is an Asselin-Robert time filter.

With the process-splitting method, the model first solves for ψ, retaining only the first two terms on the right-hand side of Eq. (5.5). This value of ψ is then corrected successively, retaining each of the other terms one at a time. It was convenient to incorporate the IAU technique into the MC2 model because of this process-splitting method. The analysis increments are applied over a data assimilation window as a constant forcing term after the physical parameterizations in the vertical, but before the treatment of horizontal diffusion and the Asselin-Robert time filter.

IAU is implemented in the MC2 model largely following from the existing ARPS Data Analysis System (ADAS) incremental analysis updating (IAU) scheme (Brewster 1996, 2003a,b), which is based on the IAU approach by Bloom et al. (1996). Parallelization of IAU uses the software architecture of the MC2 model. Applications of the ADAS IAU scheme for data assimilation (particularly of Radar data) to a storm-scale numerical model have employed a constant time weighting over a 10-min window (Brewster 2003b; Xue et al. 2002; Yoo et al. 2002a;Yoo et al. 2002b).

5.3 Time-lines of data assimilation

A schematic diagram illustrating model time-lines of MC2 self-nesting cascade runs and the data assimilation runs at 3-km grid spacing is shown in Fig. 5.4. The coarsest grid at 108-km grid spacing is started from the Eta analysis at 0000 UTC on day 1, while each

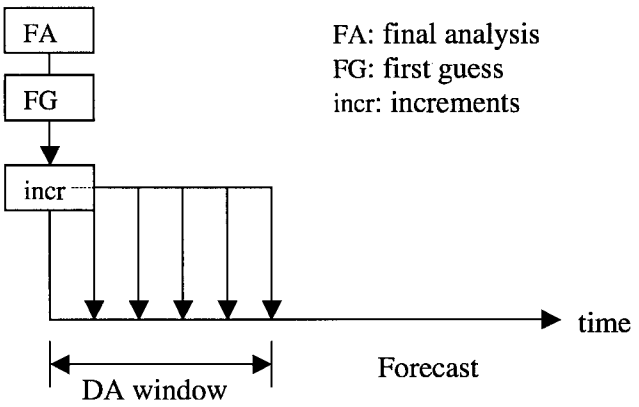

Figure 5.3: Schematic diagram illustrating data assimilation using the incremental analysis updating (IAU) technique. The analysis increments (incr) are the differences between the final analysis (FA) and the first guess (FG).

of the finer grids is started 3 hours later than the previous grid. A control run (CTRL) at 3-km grid spacing is started at model-time 1200 UTC on day 1 and is integrated 36 h. The CTRL run provides its 12-h output as a first guess for the surface data analysis and the final analysis at 0000 UTC on day 2.

A surface data analysis is obtained by optimally combining the first guess and surface observations at 0000 UTC on day 2. The surface data analysis and the Eta analysis valid at 0000 UTC on day 2 are merged by the schemes proposed in section 5.1.3 to produce a new final analysis. All data-assimilation (DA) runs incorporating final analysis increments are started at model-time 0000 UTC on day 2 and are integrated for 24 h. Same lateral boundary conditions from the MC2 4-km output are used for the DA runs and the CTRL run. Verification of subsequent forecasts at the lowest model level is performed during a 24 h forecast period for DA runs and is compared with the verification of CTRL run during 13-36 h forecast period from 0000 UTC on day 2 to 0000 UTC on day 3. This implies a 12-h difference in the forecast length between the CTRL and DA forecasts. But both forecasts are available at the same time. Tests are made for one case to start the CTRL run also from 0000 UTC on day 2 as for the DA run but without including new observations. Minor differences are found between the CTRL forecasts started from 1200 UTC on day 1 and those started from 0000 UTC on day 2.

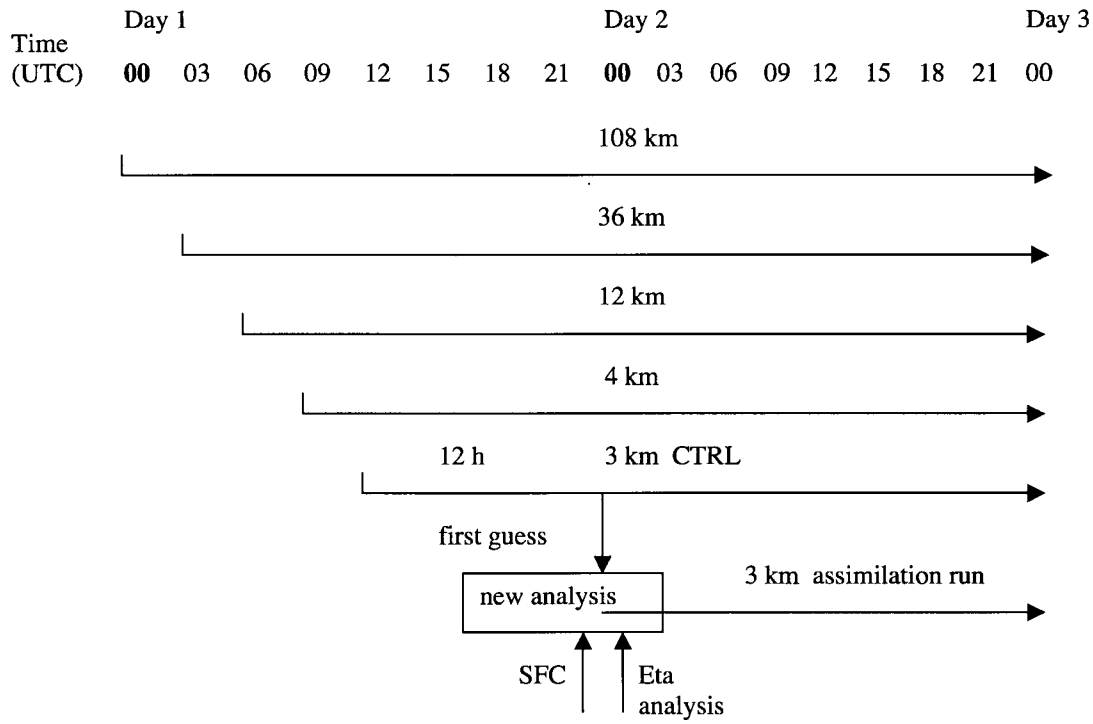

Figure 5.4: Schematic diagram illustrating model time-lines of the MC2 self-nested grids, the 3-km CTRL run, and the 3-km assimilation runs. MC2 4-km provides boundary conditions for the 3-km CTRL run and the 3-km assimilation runs. SFC indicates surface data.

Chapter 6

Case study tests of assimilating surface observations in complex terrain

In this chapter, case study tests of data assimilation (DA) are conducted for the 3-km domain (b) (see Fig. 2.3). This region is selected because of the relatively high density of surface observations and comparatively small domain size (allowing fast computations).

Numerical experiments are performed for the 29-30 July 2003 case when a large forest fire occurred near McLure, BC. The weather situation during 29-30 July 2003 was characterized by fair weather associated with a 50-kPa ridge over Southern BC, allowing the boundary-layer processes to play a dominant role.

The Eta analysis and forecasts from NECP, valid at 0000 UTC 29 July 2003, are used to drive the coarsest grid (108-km grid spacing), which in turn drives grids of 36, 12, 4, and 3 km. The MC2 3-km run is started at 1200 UTC 29 July from the MC2 4-km output, and provides its 12-h output as the first guess for the analysis at 0000 UTC 30 July. Surface analyses are performed at 0000 UTC 30 July by blending hourly surface observations with the first guess at the lowest terrain-following model level valid at the same time. The Eta analysis valid at 0000 UTC 30 July is used to generate pseudo upper-air data. A final analysis at 0000 UTC 30 July is obtained by combining the surface analysis, upper-air data and first guess. DA runs at 3-km grid spacing (with five grid points cut from each side of the domain for the first-guess run to reduce lateral boundary errors) are started at 0000 UTC 30 July from the final analysis via the IAU technique.

As mentioned earlier, surface observations are from several agencies: BC ministry of Transportation (MOT), BC Ministry of Water Land and Air Protection (WLAP), BC Ministry of Forests (MOFS), CN Railroad (CNRL), CP Rail (CPRL), Environment Canada (EC) and BC Hydro (HYDR). Those surface stations with a difference between their actual elevation and model topography greater than 500 m are excluded from analysis and verification. Out of the total 134 stations in the DA domain, 20 stations were excluded for this reason.

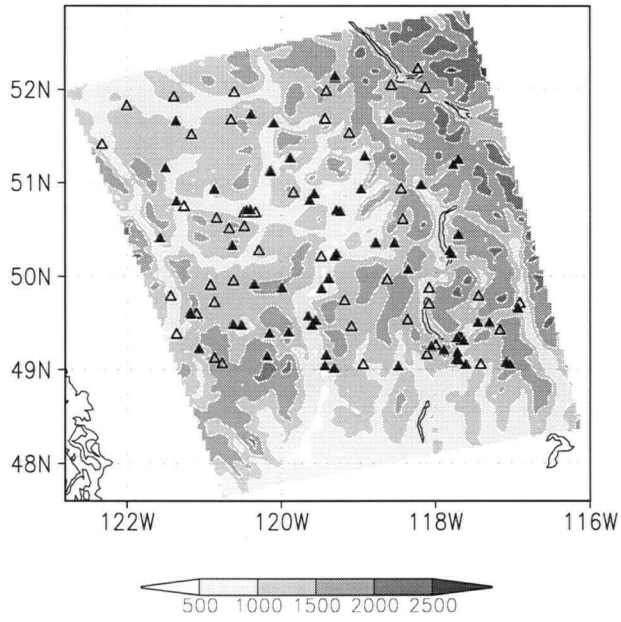

Figure 6.1: Surface weather stations (indicated by triangles) superposed on the model topography (m). Darker shading indicates higher elevations. Open triangles represent station locations with missing temperature observations at the analysis time (0000 UTC 30 July 2003), while closed triangles indicate station locations with available temperature observations at the analysis time.

6.1 Analysis results

Figure 6.1 shows all the surface stations used in analysis. There are 118 surface stations (indicated by open and closed triangles) within the analysis domain. The domain for DA runs is a little bit smaller than the analysis domain, leaving 114 stations within the DA domain for verification. Among them, 65 stations (indicated by closed triangles) reported temperature observations at 0000 UTC 30 July.

Because we use specific humidity as the moisture variable for analysis, the available observations depend on the availability of observed relative humidity, temperature and either surface pressure or sea-level pressure. The derivation of specific humidity from relative humidity is described in section 2.3. The pressure reports including surface pressure and mean sea-level pressure are much fewer than temperature reports. As a result, fewer observations for specific humidity are available, as shown in Fig. 6.2. Observations separated by 100 m or less in the horizontal and vertical are averaged to create a smaller number of "superobservations".

The verification statistics of potential temperature (Table 6.1 and Fig. 6.4) show that all methods give improved analyses compared to the first guess (FSTG) as measured by bias, mean absolute error (mae) and normalized root-mean-square error (nrmse). GAUSS is slightly better than TERR_DIFF, with smaller mae and nrmse. Both MD and MD_MT outperform GAUSS and TERR_DIFF. MD produces lowest bias, mae, whereas MD_MT has lowest nrmse. The improvement of MD_MT over MD is not as large as that for the

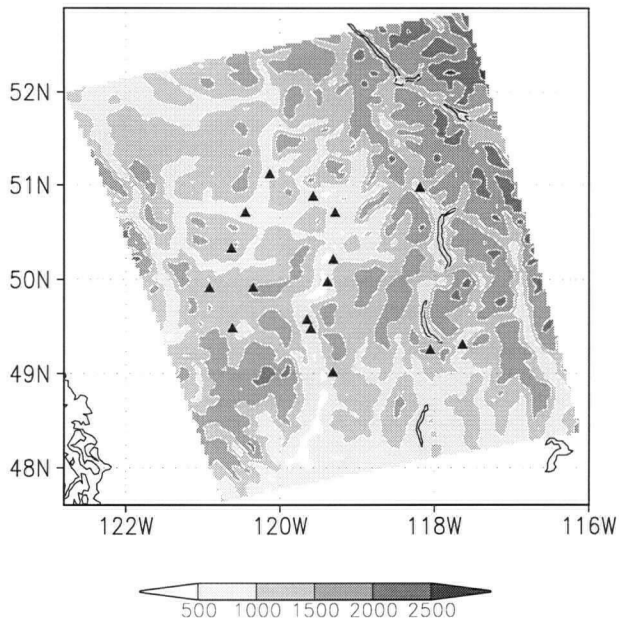

Figure 6.2: Surface station locations (indicated by closed triangles) with available specific humidity observations at the analysis time (0000 UTC 30 July 2003) and the model topography (m). Darker shading indicates higher elevations.

virtual-observation case in section 4.2. A reason for this performance could be that a very small fraction of stations (three out of the 65 stations, see Fig. 6.3) are treated as mountain-top observations in this case, while in the virtual-observation case, one out of the three stations is a mountain-top observation.

Table 6.2 and Fig. 6.5 present the verification statistics of specific humidity. MD, with smaller bias, mae and nrmse, outperforms GAUSS and TERR_DIFF. MD_MT performs the same as MD, as none of specific humidity observations is from the mountain-top stations. The MD approach with coastal refinement is not studied here, because there are no stations in the Okanagan lakes for analysis or verification.

6.2 Results from MC2 data-assimilation runs

As mentioned above, a detailed surface analysis is available at 0000 UTC 30 July 2003. Meanwhile, coarser-resolution upper-air data can be obtained from the Eta analysis available at the same time (see section 5.1.2). These two analyses can then be combined with the first guess to generate a final analysis (see section 5.1). The final analysis increments, obtained by subtracting the first guess from the final analysis, are introduced into the MC2 model via the IAU technique (section 5.2). All data-assimilation runs are started at 0000 UTC 30 July 2003 and are integrated 24 h into the model future. See Chapter 5 for more details about combination schemes, the insertion technique and time-lines of the CTRL and DA runs. Lateral boundary conditions for all DA runs and for the CTRL are from the MC2 4-km output. For all DA runs, surface analyses are from MD_MT.

In the following subsections, impacts of combination schemes and insertion rates used

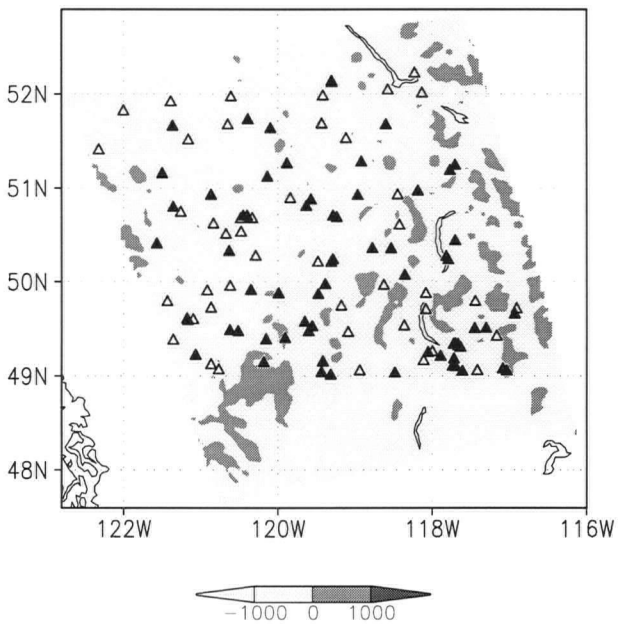

Figure 6.3: Surface weather stations (indicated by triangles) superposed on the difference between the model topography and the approximated heights of BL top (see section 3.5.2). Any station located in the darkly shaded areas will be treated as a mountain-top station. Open triangles represent station locations with missing temperature observations at the analysis time (0000 UTC 30 July 2003), while closed triangles indicate station locations with temperature observations at the analysis time.

Table 6.1: Verification of analyzed potential temperatures in terms of bias, mean absolute error (mae), and normalized root-mean-square error (nrmse) for all reporting verification stations at the analysis time: 0000 UTC 30 July 2003. N equals total number of reporting stations. Nrmse is rmse (root-mean-square error) for each method normalized by the rmse of the first guess (FSTG). For all these statistics, smaller is better.

Method	**N**	**Bias (K)**	**Mae (K)**	**Nrmse**
FSTG	64	-5.2583	7.6869	1.
GAUSS	64	0.7577	2.0990	0.5146
TERR_DIFF	64	0.7121	2.3238	0.5462
MD	64	0.0894	1.5997	0.3906
MD_MT	64	0.1332	1.6102	0.3872

Table 6.2: Same as Table 6.1, but for verification of analyzed specific humidity.

Method	**N**	**Bias (1.0E-4 kg kg-1)**	**Mae (1.0E-4 kg kg-1)**	**Nrmse**
FSTG	16	14.9409	21.9212	1.
GAUSS	16	-3.5951	7.8778	0.6208
TERR_DIFF	16	-4.4802	9.4399	0.6646
MD	16	-3.1810	6.7704	0.5940
MD_MT	16	-3.1810	6.7704	0.5940

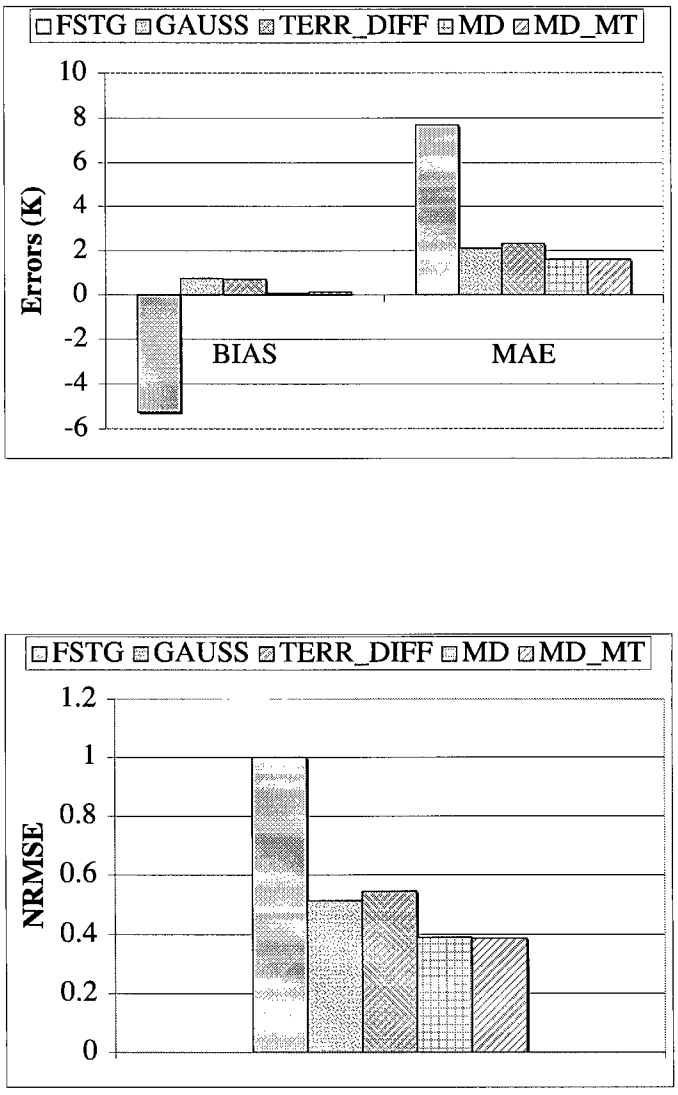

Figure 6.4: Verification of analyzed potential temperatures in terms of bias, mean absolute error (mae), and normalized root-mean-square error (nrmse) for all reporting verification stations at the analysis time: 0000 UTC 30 July 2003. Nrmse is rmse (root-mean-square error) for each method normalized by the rmse of the first guess (FSTG).

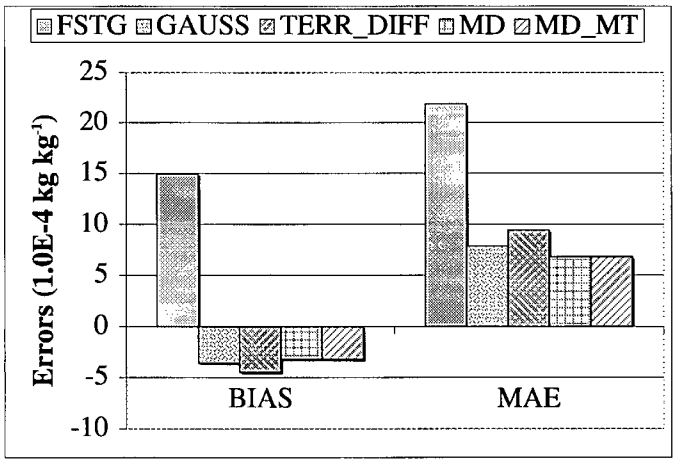

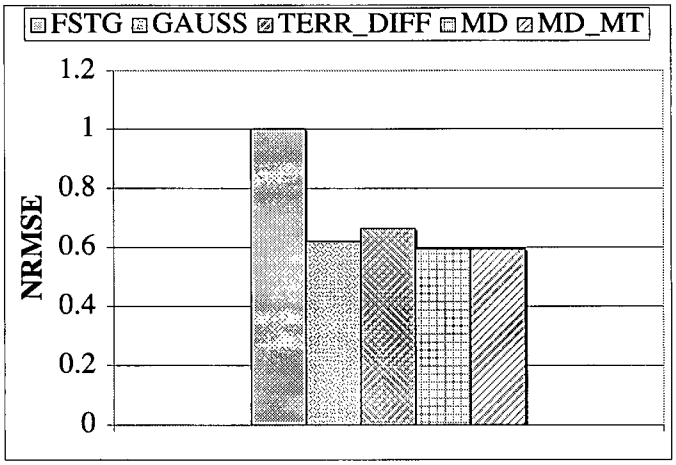

Figure 6.5: Same as Fig. 6.4, but for verification of analyzed specific humidity.

Table 6.3: Experiment design to test different schemes for combining surface and upper-air data.

EXP Name	Surface Analysis	Upper-air Analysis	Combination Scheme
CTRL	No	No	
SIGMDA	Yes	Yes	SIGM
PROFDA	Yes	Yes	PROF
SURFDA	Yes	No	
SF_SIGM	Yes	No	SIGM
SF_PROF	Yes	No	PROF

in IAU on subsequent model forecasts will be assessed when assimilating only temperature observations for the above mentioned case. We will also examine impacts of assimilating different meteorological fields on subsequent model forecasts. Verification of subsequent model forecasts at the lowest model level, against surface observations from the Emergency Weather Net Canada database, is performed during a 24-h forecast period from 0000 UTC 30 July to 0000 UTC 31 July 2003.

6.2.1 Impact of different combination schemes

To assess the impacts of the different combination schemes on subsequent forecasts, six experiments are conducted: one control experiment without assimilation (CTRL) and five other experiments, which assimilate various combinations of the surface and upper-air data (see Table 6.3). Experiment SIGMDA uses the surface analysis increments within the BL and the upper-air analysis increments above BL, where the two analysis increments are merged by the scheme SIGM (section 5.1.3). Experiment PROFDA uses the surface and upper-air data combined by the scheme PROF (section 5.1.3). These two experiments are performed to see which combination scheme is better for subsequent forecasts. Experiment SURFDA uses the surface data at only the lowest model level, and uses the first guess at all higher model levels. This experiment is used to study the effect of assimilating surface observations at only one model level. Experiment SF_SIGM uses the surface analysis only, but the analysis increments at the lowest model level are spread by the scheme SIGM to the whole BL. Experiment SF_PROF is the same as SF_SIGM, except that the surface data

are spread vertically by the scheme PROF. These two experiments are conducted to see if the assimilation of surface data plays a dominant role on subsequent surface forecasts, compared to using surface and upper-air data.

All of the five DA experiments assimilate only potential temperature observations from the surface and/or upper-air data for the 29-30 July 2003 case. For fair-comparison purposes, upper-air data are used at those grid points where the absolute values of the surface potential-temperature analysis increments are greater than 0.0 K. The final analysis increments are incorporated all at once within a single timestep (30-second) window. The subsequent forecasts at the lowest model level are verified against surface observations. Bias, mae and rmse between observations and forecasts are calculated.

Statistical assessments during 1-12 h forecast period in Tables 6.4 and 6.5 suggest that different DA experiments have variable success at predicting near-surface fields.

For potential-temperature forecasts, all of the DA experiments outperform CTRL. By assimilating surface temperature at only the lowest model level, experiment SURFDA produces very little improvement over CTRL. When surface potential temperature analyses are spread upward throughout the whole BL either through SIGM or PROF (namely experiment SF_SIGM or SF_PROF), larger improvement for predicting surface potential temperatures are achieved. By combining the surface and upper-air data, experiments SIGMDA and PROFDA gain slightly larger improvement over CTRL than SF_SIGM and SF_PROF, respectively. The improvement of SIGMDA over SF_SIGM is smaller than that of SF_SIGM over CTRL. Similarly, the improvement of PROFDA over SF_PROF is smaller than that of SF_PROF over CTRL. This implies that the assimilation of surface data plays an important role in reducing the model errors for predicting surface weather parameters. The differences in the errors between SIGMDA and PROFDA are very small. The same conclusions can be drawn from the verification results of surface temperature forecasts (not shown).

Verification results of mean sea-level pressure (SLP) forecasts reveal similar performances of all DA experiments to those indicated by temperature verification. All experiments except SURFDA outperform CTRL. Overall, the improvement of SLP forecasts is smaller than that of potential-temperature forecasts. This is reasonable as temperature observations are directly assimilated into the model. For wind forecasts, all DA experiments underperform CTRL in terms of normalized root-mean-square vector error (nrmsve) due to initial imbalances between mass and wind fields caused by a sudden change in temperature fields. SURFDA has the smallest nrmsve, probably because the assimilated temperature information is lost soon after insertion (as seen from the evolution of nrmse for surface potential temperature, not shown). The differences between nrmsves of all DA experiments except SURFDA are small. For relative humidity (RH) forecasts, all of the DA experiments except SURFDA outperform CTRL in terms of bias, mae, and rmse or nrmse, similar to the SLP statistics.

Verification statistics for 13-24 h forecast period (see Tables 6.6 and 6.5) indicates that all DA experiments produce temperature, wind, SLP and RH forecasts with errors that are close to those from CTRL.

Table 6.4: Verification of surface potential temperature (θ), vector wind ($\mathbf{V}$) and mean sea-level pressure (SLP) forecasts in terms of bias, mean absolute error (mae), root-mean-square error (rmse) and/or normalized rmse (nrmse) for all reporting verification stations (n) during a 12 h forecast period from 0100 UTC 30 to 1200 UTC 30 July 2003. Rmsve stands for root-mean-square vector error. Nrmse (nrmsve) is rmse (rmsve) for each experiment normalized by the rmse (rmsve) of the control run (CTRL). Data assimilation experiments differ in the combination of the surface and upper-air data. For all these statistics, smaller is better.

	1 - 12 h Forecast								
	θ (K) (n = 601)				SLP (hPa) (n = 153)			**V** (m s-1) (n = 506)	
Experiment	**Bias**	**Mae**	**Rmse**	**Nrmse**	**Bias**	**Mae**	**Nrmse**	**Rmsve**	**Nrmsve**
CTRL	-4.8380	5.6661	6.4715	1.	3.7556	3.9732	1.	1.7445	1.
SIGMDA	-4.1647	5.1123	5.9504	0.9195	3.1126	3.5925	0.9329	1.9478	1.1165
PROFDA	-4.1629	5.1785	5.9788	0.9239	3.0049	3.5659	0.9348	1.9958	1.1441
SURFDA	-4.8528	5.6228	6.4421	0.9955	3.7572	3.9703	1.0003	1.7502	1.0033
SF_SIGM	-4.3195	5.2334	6.0702	0.9380	3.2345	3.6122	0.9368	1.9604	1.1238
SF_PROF	-4.3279	5.2882	6.0890	0.9409	3.2109	3.6500	0.9511	1.9682	1.1282

Table 6.5: Verification of surface relative humidity in terms of bias, mean absolute error (mae), root-mean-square error (rmse) and normalized rmse (nrmse) for (left column) the 1-12 h forecast period from 0100 UTC 30 to 1200 UTC 30 July 2003; (right column) the 13-24 h forecast period from 1300 UTC 30 to 0000 UTC 31 July 2003. Data assimilation experiments differ in the combination of the surface and upper-air data. For all these statistics, smaller is better.

	1 - 12 h Forecast					**13 - 24 h Forecast**			
	RH (%) (n = 562)					RH (%) (n = 631)			
Experiment	**Bias**	**Mae**	**Rmse**	**Nrmse**	**Experiment**	**Bias**	**Mae**	**Rmse**	**Nrmse**
CTRL	32.0475	33.0919	38.0858	1.0000	**CTRL**	28.0863	28.6220	32.3712	1.0000
SIGMDA	29.6808	31.3725	36.4135	0.9561	**SIGMDA**	28.7016	29.4102	32.9633	1.0183
PROFDA	30.2433	32.1377	37.1019	0.9742	**PROFDA**	28.3768	29.0807	32.6601	1.0089
SURFDA	32.5957	33.5962	38.4899	1.0106	**SURFDA**	28.3288	28.8262	32.6434	1.0084
SF_SIGM	29.8114	31.6279	36.8775	0.9683	**SF_SIGM**	28.4262	29.1363	32.6861	1.0097
SF_PROF	29.8905	31.6764	36.5784	0.9604	**SF_PROF**	28.3216	29.0408	32.6628	1.0090

Table 6.6: Same as Table 6.4, but for the 13-24 h forecast period from 1300 UTC 30 to 0000 UTC 31 July 2003.

	13 - 24 h Forecast								
	θ (K) (n = 681)				SLP (hPa) (n = 181)			V (m s-1) (n = 585)	
Experiment	**Bias**	**Mae**	**Rmse**	**Nrmse**	**Bias**	**Mae**	**Nrmse**	**Rmsve**	**Nrmsve**
CTRL	-7.1577	7.5398	8.0764	1.	2.7725	3.1285	1.	1.8655	1.
SIGMDA	-7.1416	7.5645	8.1103	1.0042	2.7881	3.1325	1.0025	1.8644	0.9994
PROFDA	-7.1119	7.5345	8.0842	1.0010	2.7700	3.1161	0.9973	1.8619	0.9981
SURFDA	-7.2105	7.5925	8.1292	1.0065	2.8382	3.1736	1.0144	1.8638	0.9991
SF_SIGM	-7.1512	7.5719	8.1191	1.0053	2.7970	3.1385	1.0030	1.8642	0.9993
SF_PROF	-7.1403	7.5683	8.1133	1.0046	2.8012	3.1457	1.0071	1.8582	0.9960

Table 6.7: Experiment design to test different insertion rates in IAU.

EXP Name	Sfc & UA Analysis	Combination Scheme	DA Window	Insertion Rate
CTRL	No			
TH1	Yes	PROF	30 s	30 s
TH2	Yes	PROF	1 h	30 s
TH3	Yes	PROF	1 h	120 s
TH6	Yes	PROF	1 h	1200 s

6.2.2 Impact of insertion rate on model forecasts

Experiments (see Table 6.7) are conducted to assess different data assimilation strategies by varying insertion rate in IAU. Experiment TH1 incorporates temperature analysis increments all at once within a single 30-second time step. Experiment TH2 incorporates temperature analysis increments every 30 seconds over a 1-h DA window. The 1-h DA window is selected because the BL responds to the surface forcing with a time scale of about one hour or less (Stull 1988). In experiment TH3, the temperature analysis increments are introduced into the model integration every 120 seconds over a 1-h DA window. In experiment TH6, the temperature analysis increments are incorporated every 1200 seconds over a 1-h DA window. For all these four DA experiments, the final potential temperature analysis is obtained by using the PROF scheme (see section 5.1.3) for vertical spreading. Therefore, experiment TH1 is identical to PROFDA defined in Table 6.3.

The impact of varying insertion rate on potential-temperature forecasts is much larger than on SLP and wind forecasts (Table 6.8). The 1-12 h error-measures of potential temperature decrease significantly from experiment TH1 to TH2 (or TH3, TH6). This implies that introducing the temperature analysis increments over a 1-h window (and thus smaller magnitude of analysis increments at each time step) reduces data rejection. Data rejection is a common problem in the DA procedure if the observation data are significantly different from the first guess. The differences between the error-measures of experiments TH2, TH3 and TH6 are small. Comparatively, experiment TH6 produces the smallest error measures for temperature and vector wind, probably because the model is less frequently disturbed when analysis increments are introduced every 1200 s instead of every 30 s or 120 s. The bias and mae (but not rmse) of relative humidity from experiment TH6 are also smallest among all the experiments, as shown in Table 6.9.

Table 6.8: Verification of surface potential temperature (θ), wind ($\mathbf{V}$) and mean sea-level pressure (SLP) forecasts in terms of bias, mean absolute error (mae), root-mean-square error (rmse) and/or normalized RMSE (nrmse) for all reporting verification stations (n) during 12 h forecast period from 0100 UTC 30 to 1200 UTC 30 July 2003. Rmsve stands for root-mean-square vector error. Nrmse (nrmsve) is rmse (rmsve) for each experiment normalized by the rmse (rmsve) of the control run (CTRL). Data assimilation experiments differ in the insertion rate in IAU. For all these statistics, smaller is better.

	1 - 12 h Forecast								
	θ (K) (n = 601)				SLP (hPa) (n = 153)			V (m s-1) (n = 506)	
Experiment	**Bias**	**Mae**	**Rmse**	**Nrmse**	**Bias**	**Mae**	**Nrmse**	**Rmsve**	**Nrmsve**
CTRL	-4.8380	5.6661	6.4715	1.	3.7556	3.9732	1.	1.7445	1.
TH1	-4.1629	5.1785	5.9788	0.9239	3.0049	3.5659	0.9348	1.9958	1.1441
TH2	-3.8462	4.8854	5.6791	0.8776	2.6897	3.6274	0.9397	2.0240	1.1602
TH3	-3.8709	4.9097	5.7003	0.8808	2.7039	3.6208	0.9393	2.0229	1.1596
TH6	-3.7522	4.7917	5.6002	0.8654	2.7652	3.5824	0.9356	1.9906	1.1411

Table 6.9: Verification of surface relative humidity in terms of bias, mean absolute error (mae), root-mean-square error (rmse) and normalized rmse (nrmse) for the 1-12 h forecast period from 0100 UTC 30 to 1200 UTC 30 July 2003. Data assimilation experiments differ in the insertion rate in IAU. For all these statistics, smaller is better.

	1 - 12 h Forecast			
	RH (%) (n = 562)			
Experiment	**Bias**	**Mae**	**Rmse**	**Nrmse**
CTRL	32.0475	33.0919	38.0858	1.0000
TH1	30.2433	32.1377	37.1019	0.9742
TH2	29.2943	31.3002	36.1769	0.9499
TH3	29.4600	31.4542	36.3662	0.9549
TH6	29.1937	31.2109	36.2455	0.9517

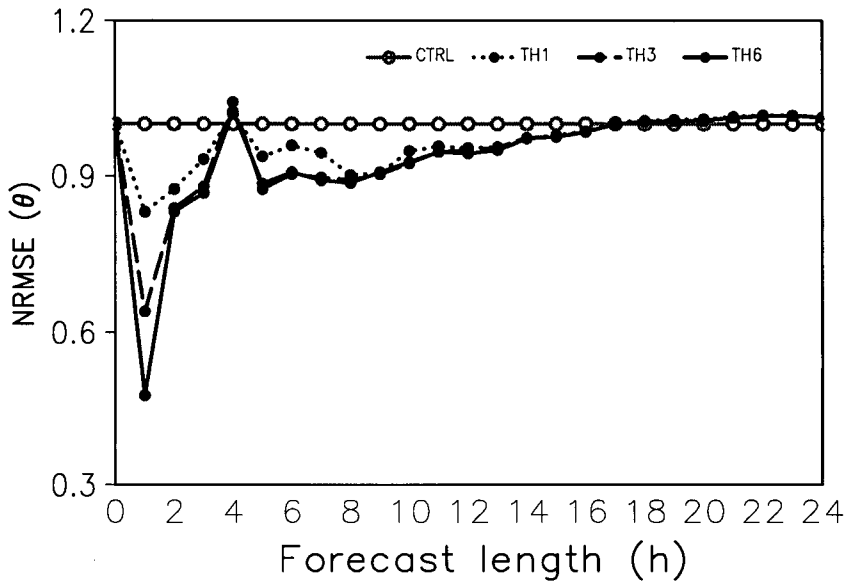

Figure 6.6: Time series of normalized root-mean-square error (nrmse) for surface potential-temperature from experiments CTRL, TH1, TH3, and TH6. Smaller nrmse corresponds to better forecasts.

Figure 6.6 shows nrmse of potential temperature versus forecast hour for experiments CTRL, TH1, TH3 and TH6. The nrmses for these experiments are much smaller than 1.0 (nrmse of experiment CTRL) during the first 12 h (except 4 h) of forecasts, and increase gradually with forecast hour. Finally the nrmse becomes close to 1.0. By applying the analysis increments over a 1-h window rather than all at once, experiment TH3 and TH6 produce much smaller nrmse than experiment TH1 for the first 7 h (except 4 h) of forecasts. Reducing the insertion rate at which the analysis increments are introduced decreases nrmse mainly for the first 1 h of forecasts.

The time series of normalized root-mean-square vector error (nrmsve) for experiments CTRL, TH1, TH3, and TH6 are shown in Fig. 6.7. By assimilating temperatures only, the model tends to produce poorer wind forecasts than CTRL during the first 12 h, due to initial imbalances between the mass and wind fields. During the second 12 h forecast period, all DA experiments and CTRL produce similar forecasts. This could be because the assimilated information propagates out of the domain. Another reason could be that the mass and wind fields are adjusted to be in balance. By applying the temperature analysis increments over a 1-h window rather than all at once (thus reducing initial imbalances), experiments TH3 and TH6 decrease nrmsve effectively for the 1 h forecast as compared to experiment TH1, but increase nrmsve a little bit during the 2-8 h forecast period. Reducing the rate at which the analysis increments are incorporated decreases further nrmsve for the 1 h forecast while reducing the increase of nrmsve for the later forecasts.

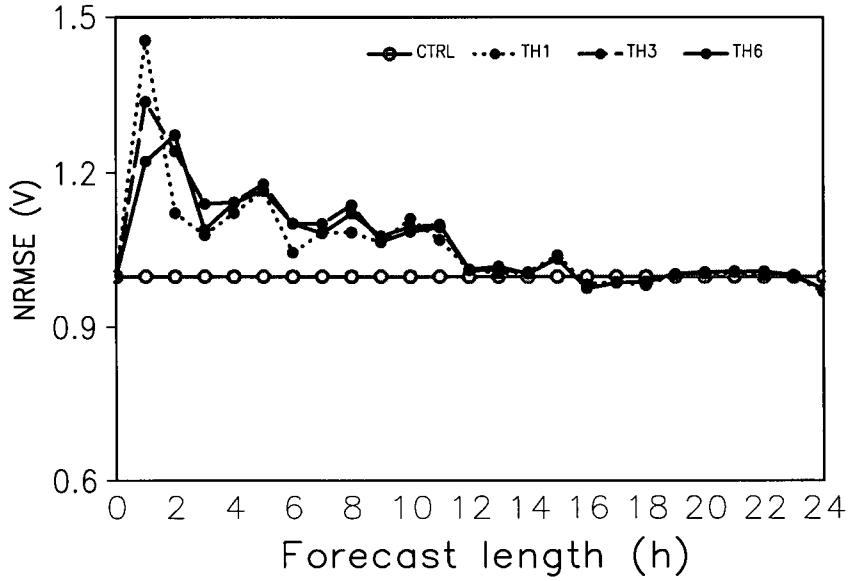

Figure 6.7: Time series of normalized root-mean-square vector error (nrmsve) for surface winds from experiments CTRL, TH1, TH3, and TH6. Smaller nrmsve corresponds to better forecasts.

Table 6.10: Experiment design for assimilating different meteorological fields. Variable T is temperature and qv is specific humidity.

EXP Name	**Sfc & UA Analysis**	**Combination Scheme**	**DA Window**	**Insertion Rate**	**Variables Assimilated**
CTRL	No				
AT	Yes	PROF	1 h	1200 s	T
AQ	Yes	PROF	1 h	1200 s	qv
ATQ	Yes	PROF	1 h	1200 s	T, qv

6.2.3 Impact of assimilating different fields

To study the impact of assimilating different meteorological fields on subsequent model forecasts, three other experiments (Table 6.10) are performed, each of which assimilates temperature only (AT), specific humidity only (AQ), and both temperature and specific humidity (ATQ), respectively. For all these DA experiments, the final analyses of potential temperature and specific humidity are obtained by combining surface and upper-air data using the PROF scheme (section 5.1.3) for vertical spreading; the final analysis increments are incorporated into the MC2 model every 1200 seconds over a 1-h DA window. Therefore, experiment AT is identical to experiment TH6 defined in Table 6.7. Finally, the MC2 model is run to make a 24 h forecast that is verified against subsequent surface observations.

For potential-temperature and SLP forecasts, experiment AQ (assimilating specific humidity only) produces poorer forecasts than CTRL (Table 6.11). The effects on temperature forecasts of assimilating specific humidity can be due to scattered low clouds formed during the forecast period. The forecasts from experiments AT and ATQ are greatly improved compared to the CTRL forecast. By assimilating both temperature and specific humidity, experiment ATQ is improved compared to experiment AT that assimilates temperature only.

All of the DA experiments (AT, AQ and ATQ) give poorer wind forecasts than CTRL. In contrast to the error measures of potential temperature and SLP, nrmsve is the smallest from experiment AQ, and the largest from experiment ATQ. Winds are more sensitive to temperature perturbations than to moisture perturbations.

Surprisingly, assimilating only specific humidity (experiment AQ) slightly decreases bias and mae (but slightly increases rmse) in the forecasts of surface relative humidity (Table 6.12). As a result, experiment ATQ produces slightly larger RH error measures compared to experiment AT, while experiment AT gives the best RH forecasts, with minimum bias, mae, rmse and nrmse (Table 6.12).

However, verification statistics of surface specific humidity (see Table 6.13) show that rmse from experiment AQ is reduced by about 18% from the CTRL experiment. The needed derivation of surface specific humidity from observed surface relative humidity might help to explain the contrasting results between the verification statistics of surface relative humidity and specific humidity. As mentioned in section 2.3, the derivation of specific humidity depends on surface pressure and temperature. When surface pressure is not available, an approximation of surface pressure from mean sea-level pressure is made.

The impact of assimilating different meteorological fields on the diurnal variation of surface temperature is examined at three stations near McLure and three stations in the Okanagan Valley (Fig. 6.8). These stations are chosen because McLure and the Okanagan Valley suffered extensive forest fires in the past few years, for which improved forecasts could have aided fire fighters in saving more of the adjacent homes. The diurnal variation of surface temperature forecasts from experiments AT and AQ is almost the same as experiments ATQ and CTRL, respectively, and therefore not included here.

Figure 6.9 compares surface temperature forecasts (at the lowest model level, which is 5.3 m above model ground) from experiments CTRL and ATQ to the observed surface temperatures at three stations near McLure every 1 h during 24 h forecast period from 0000 UTC (00Z) 30 July to 0000 UTC 31 July 2003. For these three stations, the first guess (from CTRL experiment) underforecasts the surface temperature at the analysis

Table 6.11: Verification of surface potential temperatures (θ), mean sea-level pressure (SLP) and vector wind ($\mathbf{V}$) forecasts in terms of bias, mean absolute error (mae), root-mean-square error (rmse) and/or normalized RMSE (nrmse) for all reporting verification stations (n) during 12 h forecast period from 0100 UTC 30 to 1200 UTC 30 July 2003. Rmsve stands for root-mean-square vector error. Nrmse (nrmsve) is rmse (rmsve) for each experiment normalized by the rmse (rmsve) of the control run. Data assimilation experiments differ in the variables assimilated into the model.

	1 - 12 h Forecast								
	θ (K) (n = 601)				SLP (hPa) (n = 153)			**V** (m s-1) (n = 506)	
Experiment	**Bias**	**Mae**	**Rmse**	**Nrmse**	**Bias**	**Mae**	**Nrmse**	**Rmsve**	**Nrmsve**
CTRL	-4.8380	5.6661	6.4715	1.	3.7556	3.9732	1.	1.7445	1.
AT	-3.7522	4.7917	5.6002	0.8654	2.7652	3.5824	0.9356	1.9906	1.1411
AQ	-4.9213	5.7311	6.5542	1.0128	3.8518	4.0770	1.0214	1.7726	1.0161
ATQ	-3.6882	4.7416	5.5484	0.8574	2.7530	3.5666	0.9236	2.0333	1.1655

Table 6.12: Verification of surface relative humidity in terms of bias, mean absolute error (mae), root-mean-square error (rmse) and normalized rmse (nrmse) for 1-12 h forecast period from 0100 UTC 30 to 1200 UTC 30 July 2003. Data assimilation experiments differ in the variables assimilated into the model.

	1 - 12 h Forecast			
	RH (%) (n = 562)			
Experiment	**Bias**	**Mae**	**Rmse**	**Nrmse**
CTRL	32.0475	33.0919	38.0858	1.0000
AT	29.1937	31.2109	36.2455	0.9517
AQ	31.3868	32.7379	38.4099	1.0085
ATQ	29.6367	31.5080	36.7007	0.9636

Table 6.13: Same as Table 6.12 except for verification of surface specific humidity.

	1 - 12 h Forecast			
	qv (1.0E-4 kg kg-1) (n = 169)			
Experiment	**Bias**	**Mae**	**Rmse**	**Nrmse**
CTRL	18.883	24.465	29.723	1.0000
AT	17.605	24.051	28.801	0.9690
AQ	14.082	19.810	24.249	0.8158
ATQ	18.410	23.517	28.369	0.9544

time (0000 UTC 30 July). By assimilating dense local surface temperature observations, experiment ATQ produces improved forecasts. The improvement in surface temperature from data assimilation decreases greatly from 1 h to 2 h forecast for the three stations. At Kamloops ARPT (top plot of Fig. 6.9), the improvement of ATQ over CTRL is evident in the forecasts from 1 to 17 h (i.e., from 0100 to 1700 UTC 30 July). The improvement at Sparks Lake (middle plot of Fig. 6.9) lasts about 12 hours. The measurement shows a large, sudden decrease in surface temperature at 0400 UTC. Whether this decreasing is caused by local effects or by observation error is unknown. The large drop in surface temperature can also be seen at East Barriere (bottom plot of Fig. 6.9), for which experiment ATQ produces better forecasts than CTRL for only the first three hours and then similar forecasts to CTRL for the later period. The trend of surface-temperature evolution from experiment ATQ are the same as experiment CTRL and almost matches the observed trend.

Time series of observed and forecasted surface temperatures are also shown for three stations located in the populated Okanagan Valley in Fig. 6.10. Similar conclusions can be drawn from Fig. 6.10: the large improvement in surface temperature from experiment ATQ decreases from 1 h to 2 h forecast, but slight improvement lasts about 13 hours. Therefore, assimilation of observations at 0000 UTC (1700 PST) is good to improve forecasts during the night. This implies that assimilation of observations available in the early morning (e.g., 1200 UTC) is needed to improve the daytime forecasts. The trend of observed surface-temperature evolution is well predicted by experiments ATQ and CTRL. However, the difference in the magnitude between the observed and forecasted surface temperature is obvious.

At 0400 UTC, Figs. 6.9 and 6.10 show either a large drop in surface temperature observations for some stations or missing reports for some other stations. This helps to explain the sudden jump of nrmse for surface potential temperature at 4 h forecast in Fig. 6.6.

Generally speaking, after assimilating surface temperature within the BL, experiment ATQ improves surface temperature forecasts in magnitude while keeping the diurnal cycle unaffected.

The difference between the observed and model forecasted surface temperature varies by station, partly because each station is affected by its local weather, and partly because the elevation difference between the observation location and modeled station location varies by station. Table 6.14 summarizes observed station elevations and modeled station elevations for the six stations used here. The modeled station elevations are obtained by interpolating from the elevations at the lowest model level of four neighboring grid points surrounding the station. The difference in the magnitude between the observed and forecasted surface temperature for East Barriere is very small from 0500 to 1400 UTC, even though the elevation difference at that station is the largest among the six stations. This is because of the sudden drop in surface temperature at 0400 UTC and thus lower surface temperature during the following several hours. Penticton ARPT has larger elevation difference than other stations except East Barriere, and hence the difference between the observed and modeled surface temperatures is larger for Penticton ARPT than for other stations (see bottom plot of Fig. 6.10). The model bias in surface temperature caused by elevation difference can be easily removed by Kalman-filter predictor postprocessing (Roeger et al. 2003).

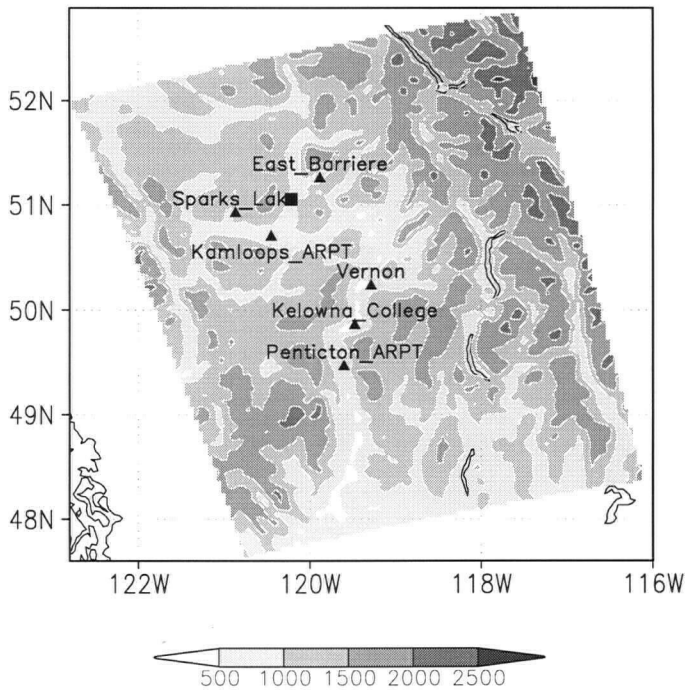

Figure 6.8: Three surface stations (indicated by closed triangles) near McLure (indicated by a closed square) and three in Okanagan valley. The model terrain heights (m) are shown by shading. Darker shading corresponds higher elevations.

Table 6.14: The actual station elevations and the modeled station elevations for various surface stations.

station	Actual Elev (m)	Modeled Elev (m)	Elev error of model (m)
Kamloops ARPT	346.	541.37	195.37
Sparks Lake	1036.	1029.72	-6.28
East Barriere	671.	911.85	240.85
Vernon	556.	486.83	-69.17
Kelowna College	300.	399.40	99.40
Penticton ARPT	344.	568.97	224.97

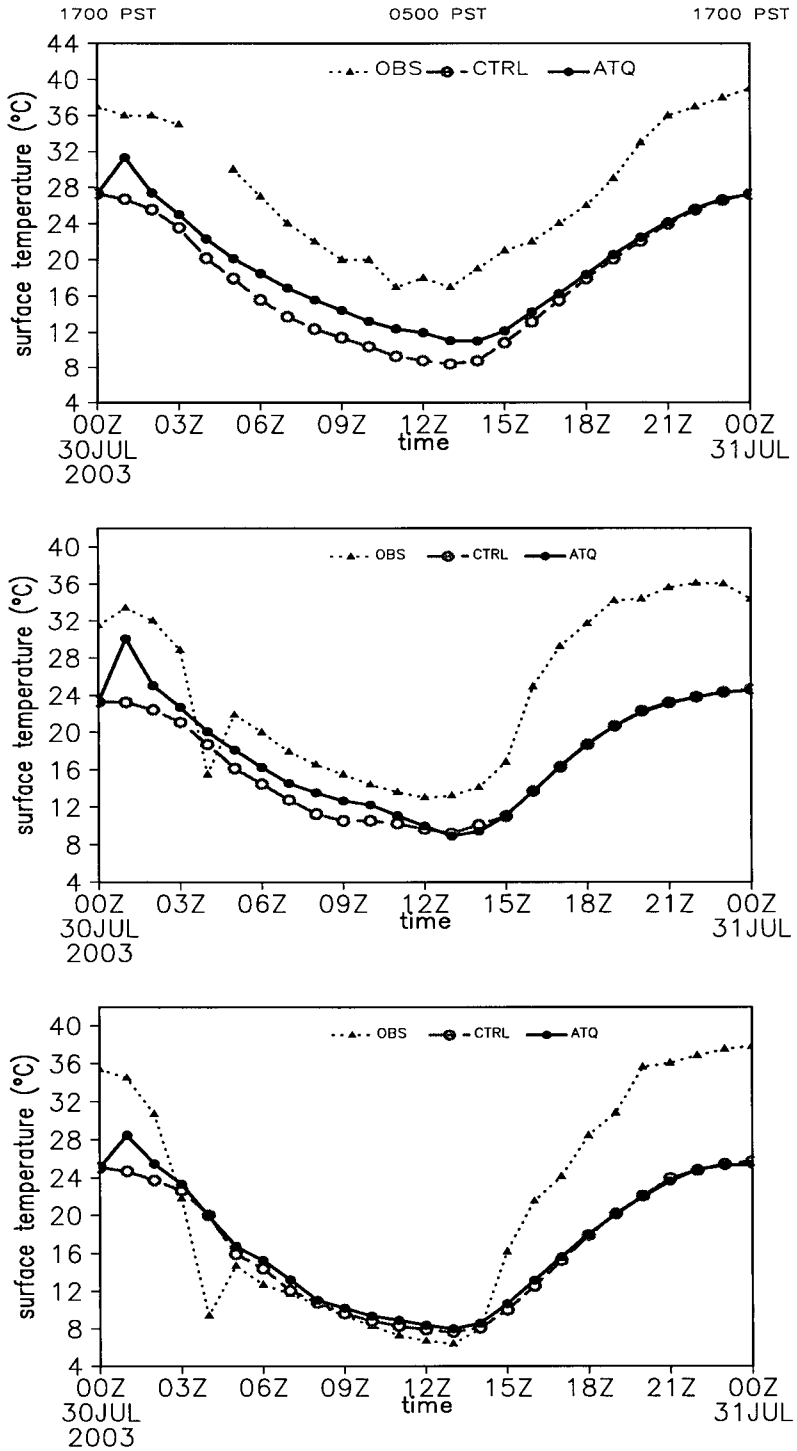

Figure 6.9: Time series of observed surface temperature (dotted line with closed triangles) and the forecast temperature at the lowest model level from the control run (CTRL; dashed line with open circles) and from experiment ATQ (solid line with closed circles) for stations near McLure, BC. (top) Kamloops ARPT; (middle) Sparks Lake; (bottom) East Barriere.

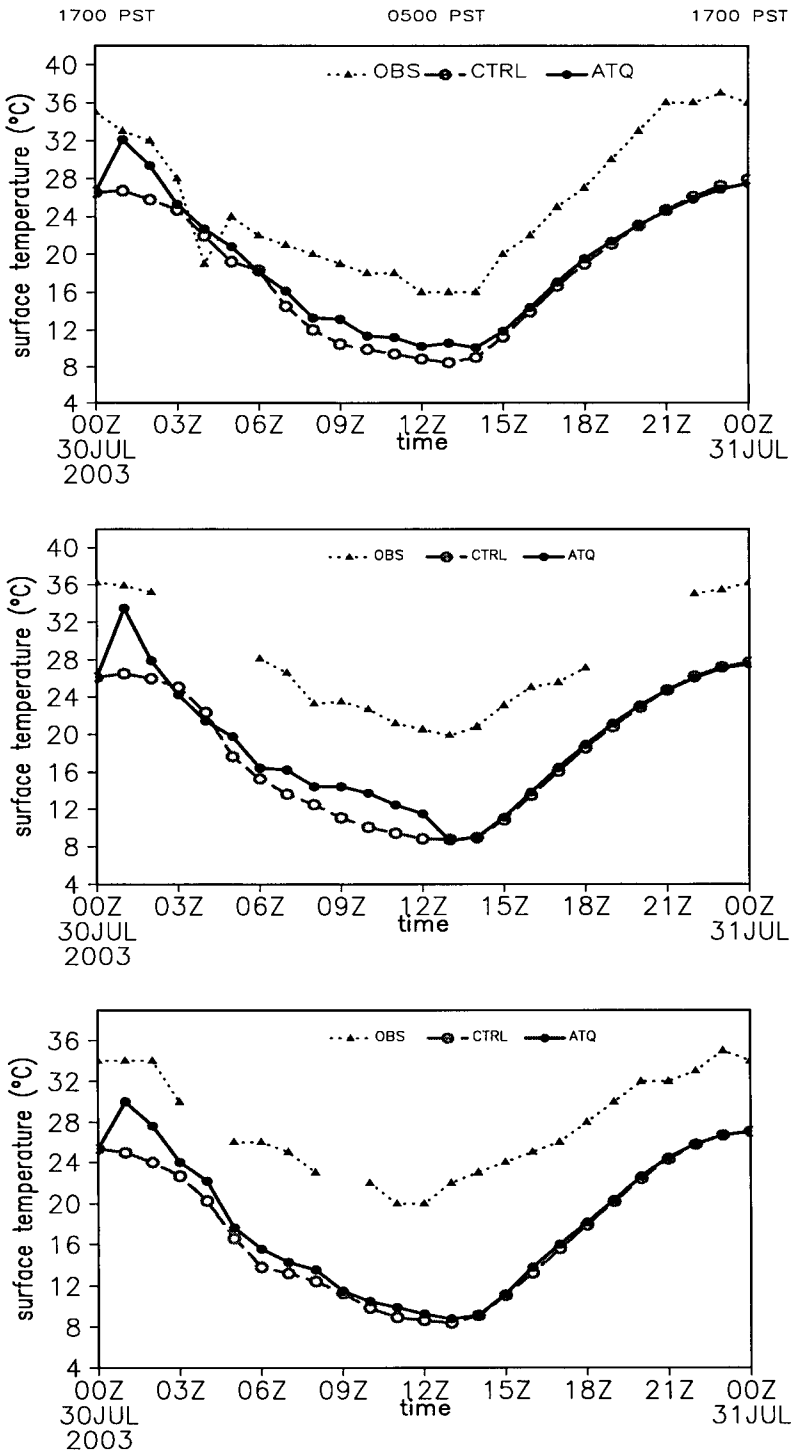

Figure 6.10: Time series of observed surface temperature (dotted line with closed triangles) and the forecast temperature at the lowest model level from the control run (CTRL; dashed line with open circles) and experiment ATQ (solid line with closed circles) for stations in Okanagan Valley, BC. (top) Vernon; (middle) Kelowna College; (bottom) Penticton ARPT.

6.2.4 Summary

This chapter presents results from case study tests of surface data assimilation for the 3-km domain (b) (see Fig. 2.3). The MD approaches (MD and MD_MT) are tested for specific-humidity and potential-temperature analyses, and are compared with GAUSS and TERR_DIFF. Because there are no water stations in the 3-km domain (b), the MD approach after coastline refinement (MD_LSMG) is not studied in this chapter. It is found that both MD and MD_MT outperform GAUSS and TERR_DIFF in potential-temperature and specific-humidity analyses. The improvement of MD_MT over MD is not as large as that for the virtual-observation case in section 4.2. A reason for this performance could be that a very small fraction of stations (three out of the 65 stations) are treated as mountain-top observations in this case, while in the virtual-observation case, one out of the three stations is located at the mountain top.

Various DA experiments are conducted to examine the impacts on subsequent model forecasts of different combination schemes, different insertion rates, and of assimilating different meteorological fields.

Surface information assimilated at only the lowest model level is soon lost at the beginning of the forecast period. Larger improvement over the control (CTRL) run is achieved when surface information is spread upward throughout whole BL. Combining the surface and pseudo upper-air data gives slightly larger improvement over the CTRL forecast than assimilating only surface data but spread upward throughout the whole BL. This implies that assimilation of surface data plays an important role in reducing the model errors of near-surface weather parameters. Experiments that spread surface information by the two combination schemes (SIGM and PROF) behave only slightly differently.

By applying the temperature analysis increments over a 1-h window rather than all at once by using incremental analysis update (IAU), the model decreases nrmse of potential temperature for the first 7 h forecast (and nrmsve of winds for the first 1 h forecast), except for the 4 h forecast (valid at 0400 UTC) when a large sudden drop in surface temperature observations at some stations and missing reports at others are observed. Better skill can be achieved when the final analysis increments are incorporated into MC2 every 1200 s over a 1-h DA window.

By assimilating surface temperature and specific humidity, the forecast quality of those parameters and mean sea-level pressure are better than CTRL. The DA improvement is the largest at 1 h, and gradually decreases with forecast time. However, the DA run gives poorer forecasts of near-surface winds, which are not assimilated into the model.

Chapter 7

Near-real-time operational data-assimilation runs

It is demonstrated in the previous chapters that the mother-daughter (MD) approaches produce better analyses than the other existing analysis methods. In addition, with case study tests during 29-30 July 2003, it is shown in Chapter 6 that a numerical forecast model started with the improved temperature and specific humidity analyses from the MD approach (after mountain-top refinement) makes a better forecast for near-surface temperature, humidity and mean sea-level pressure (SLP), but not for winds.

This chapter further tests the MD approaches (and the methodology of assimilating surface observations) for robustness over a longer period by applying them to a parallel run of the daily operational forecast system. These daily operational data-assimilation parallel runs are started about 12 h after data availability, because limited computer resources require that the primary, real-time, operational runs be finished first. That's why the parallel runs are "near-real-time".

7.1 Descriptions of the near-real-time operational data-assimilation runs

As described in the previous chapters, assimilating dense, local surface observations into a high-resolution NWP model consists of three major components: the anisotropic mesoscale analysis method (Chapter 3), combination of surface and upper-air data, and the incremental analysis updating (IAU) insertion (Chapter 5). In order to perform independent tests for the MD approaches and assimilation strategies of surface observations, all of the three components are incorporated into a daily operational forecasting system using the MC2 model, starting at the end of September 2004.

As mentioned earlier, the MC2 model at UBC is configured with five one-way self-nested grids with horizontal grid spacings of 108, 36, 12, 4, and 2 km. The data-assimilation (DA) run is performed daily for only the finest grid of 2 km. The model time-lines shown in Fig. 7.1 are almost the same as those for the case study tests in the previous chapters (see Fig. 5.4), except for different forecast length and model resolution (a replacement of 3 km by 2 km). The 108-km forecast starts from NCEP Eta analyses at 0000 UTC each day, and provides initial and boundary conditions for the 36-km forecast, which in turn drives the

12-km grid, and so on.

In an operational setting, the grids at 108, 36, 12, and 4 km are actually run into the future beyond Day 3. Limited by computational resources, the primary operational 2-km grid driven by the 4-km output is run for only 27 hours. Hereafter, this primary operational 2-km run is referred to as a control (CTRL) run. This CTRL run is started at model-time 1200 UTC on Day 1 (Fig. 7.1), and provides its 12-h output as a first guess for analyses at 0000 UTC on Day 2 for the parallel DA run.

For the operational DA runs in this chapter, the surface observations of potential temperature and specific humidity from the Emergency Weather Net Canada at 0000 UTC on Day 2 are first analyzed by using the ADAS Bratseth (1986) scheme (Brewster 1996) modified to include the mother-daughter approach after mountain-top refinement (MD_MT) (as previously described in section 3.5.2). The final analyses valid at 0000 UTC are obtained by combining the first guess, surface and upper-air data by using the scheme PROF (see section 5.1.3). Those surface weather stations with a difference between their actual elevation and model topography greater than 500 m are excluded from analysis and verification. Out of the total 305 stations in the DA domain, 22 stations were excluded for this reason. Stencils of different sharing factors at the model grid points are generated for each of the remaining 283 surface stations using method MD_MT, so that there is no need to re-calculate the sharing factors during each day's analysis. In order to compare with the subsequent impacts of data assimilation for the July 2003 case in Chapter 6, method MD_MT is chosen for the operational runs.

The 2-km DA parallel forecast run is started at model-time 0000 UTC on Day 2 and is integrated forward for 15 h. The observation information is assimilated through gradual introduction of the final analysis increments of temperature and specific humidity by using the IAU technique. The DA window is one hour. Boundary conditions for both CTRL and DA forecasts are from the 4-km output. Verification of subsequent forecasts at the lowest terrain-following model level against surface observations is performed during the 15 h forecast period for the DA forecast runs, and are compared with verification of the CTRL forecast runs during the 12-27 h forecast period from 0000 to 1500 UTC on day 2.

Each day, the analysis obtains its first guess from the 12-h output of the CTRL run. This implies that the surface observations are not incorporated into the forecast cycle; thus, each analysis and DA forecast are independent of past observations. This is good for independent tests of the robustness of the DA module. Results for the months of November and December 2004 are given below. Due to a hardware failure of the supercomputer in December 2004, the sample size in December is smaller than that in November.

7.2 Analysis results

Figure 7.2 shows all of 283 surface stations (indicated by open and closed triangles) within the analysis domain. Even though the domain for the DA run is a bit smaller than the analysis domain, stations within the DA domain for verification remain the same. However, the number of observations used in analysis and verification varied from day to day depending on the number of stations actually reporting. Because verification was scheduled to be done one day later than analysis, the number of available reports for verification is larger than that for analysis.

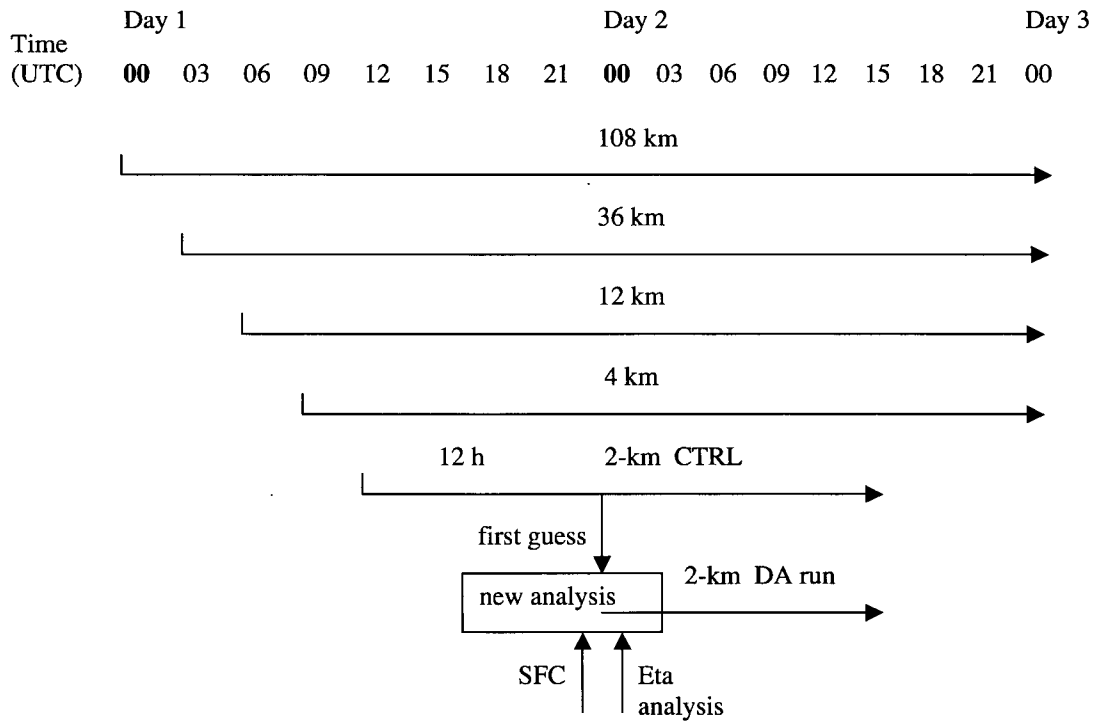

Figure 7.1: Schematic diagram illustrating model time-lines of the operational MC2 self-nested grids including the 2-km data assimilation (DA) run. The 2-km CTRL run is the regular operational 2-km run. MC2 4-km provides boundary conditions for the 2-km CTRL run and the parallel 2-km assimilation run. SFC indicates surface data.

Figure 7.3a shows the number of stations having temperature reports for analysis and verification during November 2004. The difference between the number of available temperature reports for analysis and for verification ranges from 1 to 44 with an average of 24. This makes the verification more independent, as some of observations used in the verification were not used in the analysis. The difference between the number of available specific humidity observations for analysis and for verification are rather small, ranging from 0 to 2 (Fig. 7.3b). It is also apparent that the number of available observations of specific humidity is much smaller than that of temperature on any single day. For example, at 0000 UTC 2 November 2004, 130 stations (indicated by closed triangles in Fig. 7.2) reported temperatures, whereas 36 stations (indicated by closed triangles in Fig. 7.4) had observations of specific humidity. As explained in Chapter 6, there are much fewer observations of specific humidity, because the direct measurement of humidity is relative humidity, but the pressure reports needed for conversion from relative humidity to specific humidity are sparse. The above features of the difference between the number of available temperature (or specific humidity) reports for analysis and for verification are also observed for the month of December (not shown).

Surface analyses of potential temperature and specific humidity are verified against surface observations over two months: November and December. Five analysis methods (defined in Table 4.1) are compared. Method MD_MT was performed every day in near-real-time mode. The other methods were performed later (not near-real-time) for comparison. For method MD_LSMG, 18 out of 283 surface weather stations are identified to be stations over water, based on the land-sea mask input data for the MC2 model at 2-km grid spacing. The parameters used in each analysis method are the same as for the case studies in the previous chapters.

Potential temperature. Table 7.1 summarizes the verification statistics (also see Fig. 7.5) for the month of November, when the analyses were performed at 0000 UTC during the period from 2 November to 1 December 2004. The analyses from all methods have smaller positive biases than the first guess (FSTG). The bias of TERR_DIFF is smaller than those of GAUSS, MD, and MD_MT. But the differences between the biases of the analyses from different methods except MD_LSMG are very small. The mean absolute error (mae) and root-mean-squared error (rmse) of the analysis from each method are largely decreased from those of the first guess. The rmse is reflected in the nrmse (normalized rmse of the analysis by the rmse of the first guess). Even though TERR_DIFF produces smaller bias than all other methods except MD_LSMG, it has the largest mae and nrmse. The mother-daughter approaches (MD, MD_MT, and MD_LSMG) have smaller mae and nrmse than GAUSS and TERR_DIFF similar to the July 2003 case. The mountain-top refinement introduced into the MD approach results in a minor increase of mae and nrmse. This is slightly different from the July 2003 case. Comparatively, the MD approach after coastline refinement (MD_LSMG) has the smallest bias, mae, and nrmse, which is similar to what is found for the February 2003 case. But the improvement of MD_LSMG over MD is smaller, compared to the February 2003 case.

The verification statistics for the month of December (Table 7.2) show similar results to the month of November. One difference is that the first guess now has small negative bias, whereas the analyses from all methods have smaller positive bias. The surface observations at 0000 UTC were analyzed during the period from 2 December 2004 to 1 January 2005.

Specific humidity. The bias, mae, and nrmse of the specific humidity analyses and

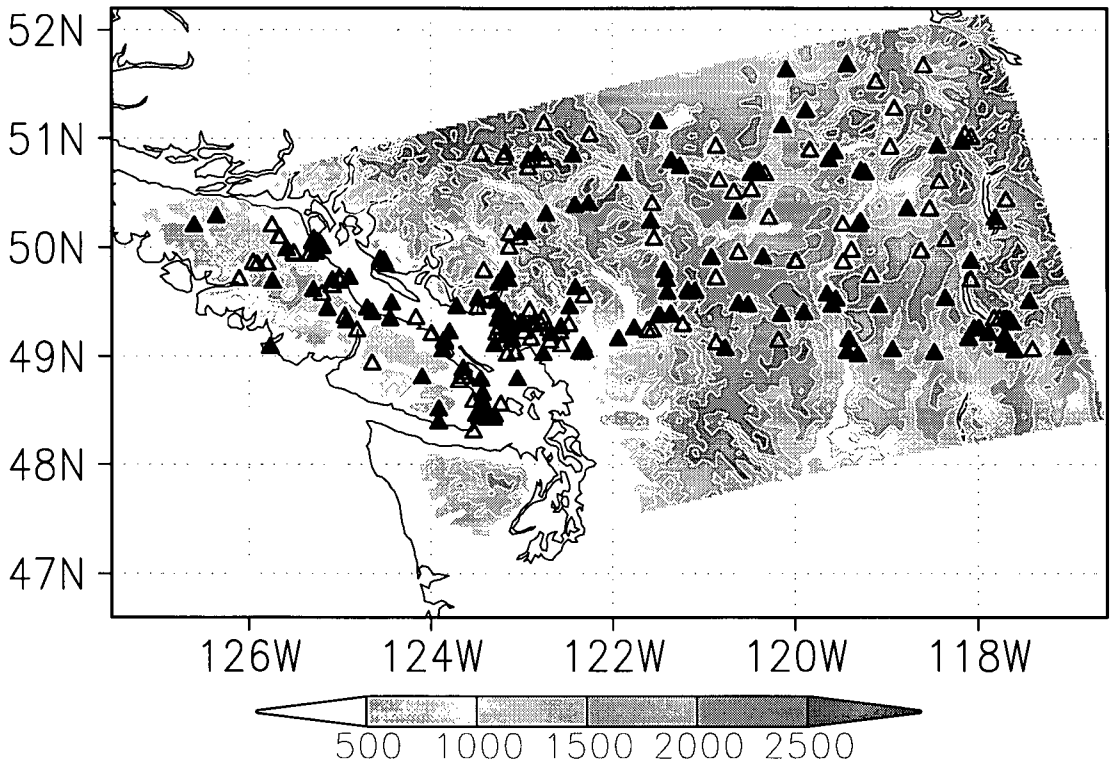

Figure 7.2: Surface weather stations (indicated by triangles) within the Canadian portion of the domain superposed on the 2-km MC2 model topography (m). Darker shading indicates higher elevations. Open triangles represent station locations with missing temperature observations at this one sample analysis time 0000 UTC 2 November 2004, while closed triangles indicate station locations with available temperature observations at that analysis time.

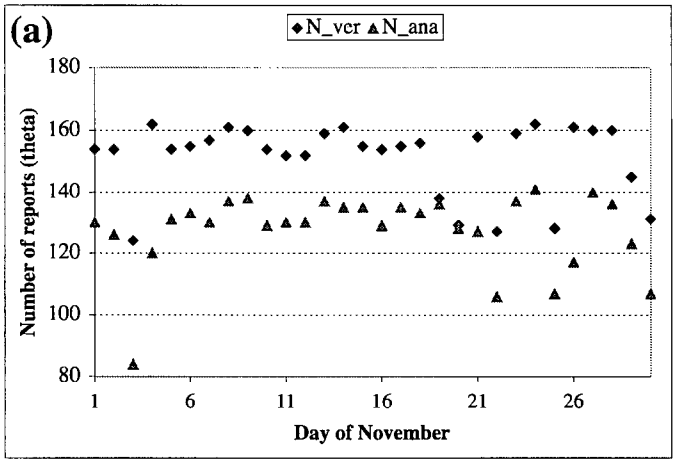

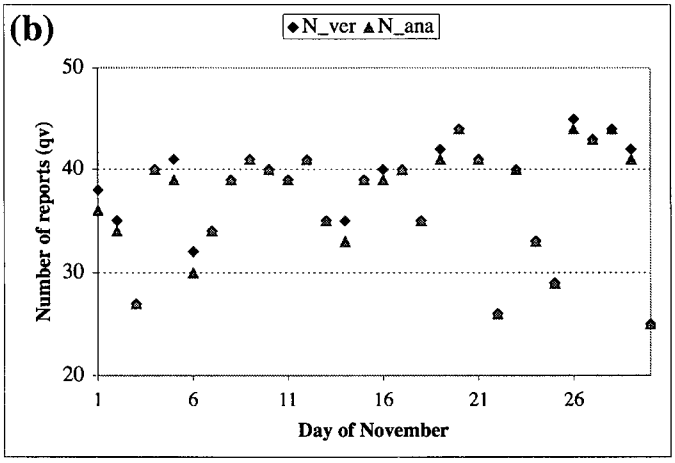

Figure 7.3: Number of stations that had reports of a) potential temperature and b) specific humidity for each day of November 2004. Each day in the x-axis corresponds to "Day 1" in Fig. 7.1. Hence, the number of available reports are actually for a date that is one day later than the date shown in x-axis. Those indicated by triangles are the numbers of reports used in analyses; whereas those marked by diamonds are the numbers of reports used in verification.

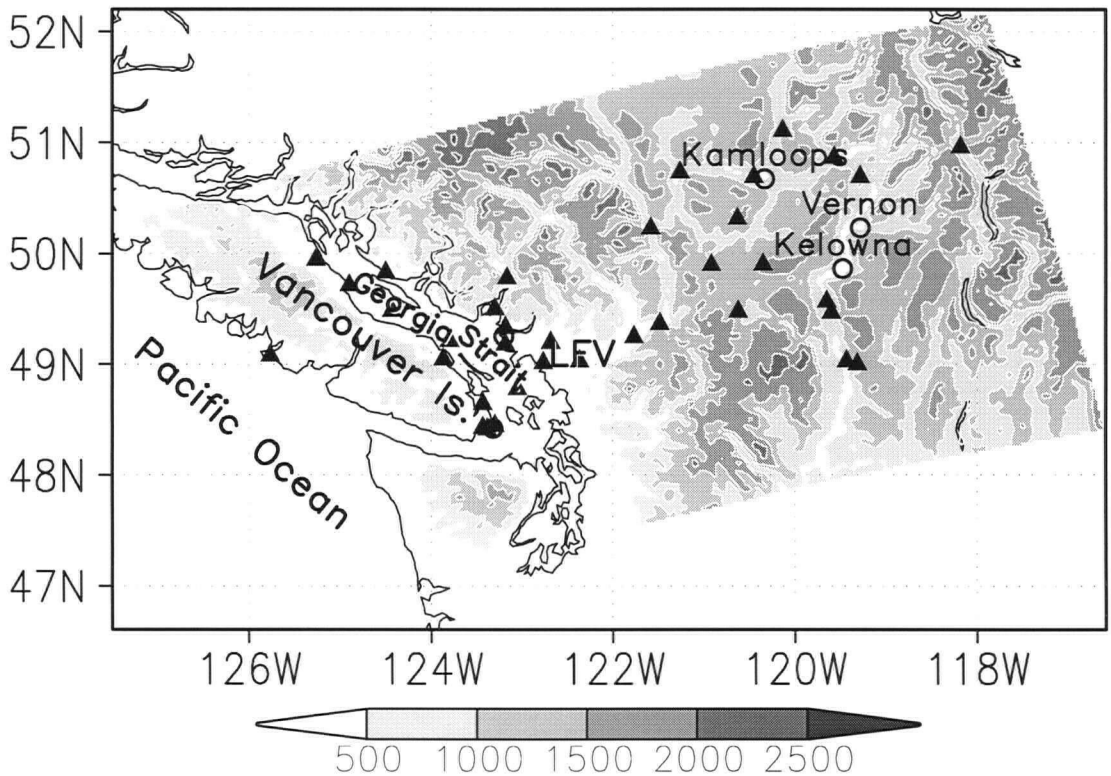

Figure 7.4: Surface station locations (indicated by a closed triangle) with available specific humidity observations at this one sample analysis time 0000 UTC 2 November 2004 and the 2-km MC2 model topography (m). Darker shading indicates higher elevations.

Table 7.1: Verification of analyzed potential temperatures in terms of bias, mean absolute error (mae), and normalized root-mean-square error (nrmse) for all reporting verification stations in November 2004. N equals total number of reporting stations. Nrmse is rmse (root-mean-square error) for each method normalized by the rmse of the first guess (FSTG). For all these statistics, smaller magnitude is better.

Method	**N**	**Bias (K)**	**Mae (K)**	**Nrmse**
FSTG	4537	0.2929	2.2384	1.
GAUSS	4537	0.2858	1.1582	0.6107
TERR_DIFF	4537	0.2609	1.2782	0.6438
MD	4537	0.2843	1.0244	0.5799
MD_MT	4537	0.2843	1.0314	0.5822
MD_LSMG	4537	0.2190	0.9675	0.5630

Table 7.2: Same as Table 7.1, except for December 2004.

Method	**N**	**Bias (K)**	**Mae (K)**	**Nrmse**
FSTG	3364	-0.7103	2.6375	1.
GAUSS	3364	0.2092	1.2775	0.5906
TERR_DIFF	3364	0.1907	1.3834	0.6152
MD	3364	0.1910	1.1532	0.5671
MD_MT	3364	0.1969	1.1643	0.5707
MD_LSMG	3364	0.0812	1.1078	0.5596

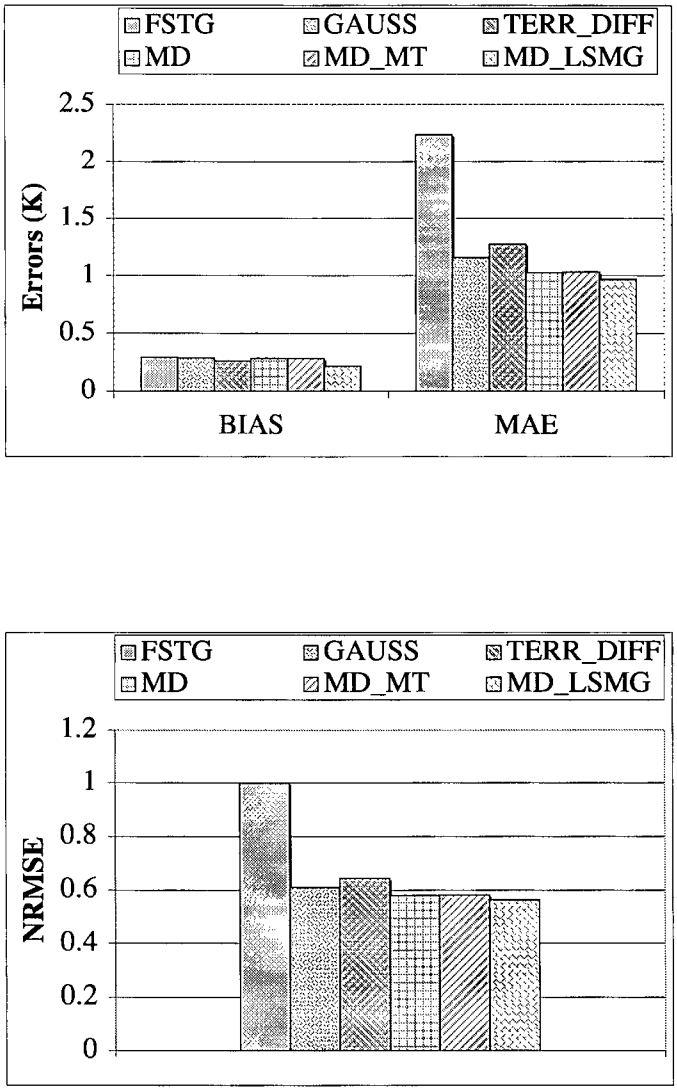

Figure 7.5: Verification of analyzed potential temperatures in terms of bias, mean absolute error (mae), and normalized root-mean-square error (nrmse) for all reporting verification stations in November 2004. Nrmse is rmse (root-mean-square error) for each method normalized by the rmse of the first guess (FSTG).

Table 7.3: Same as Table 7.1, but for verification of analyzed specific humidity in November 2004.

Method	N	Bias (1.0E-4 kg kg-1)	Mae (1.0E-4 kg kg-1)	Nrmse
FSTG	1125	-5.987	7.800	1.
GAUSS	1125	-0.451	1.892	0.292
TERR_DIFF	1125	-0.418	2.443	0.356
MD	1125	-0.169	1.687	0.270
MD_MT	1125	-0.169	1.687	0.270
MD_LSMG	1125	-0.464	1.553	0.247

Table 7.4: Same as Table 7.1, but for verification of analyzed specific humidity in December 2004.

Method	N	Bias (1.0E-4 kg kg-1)	Mae (1.0E-4 kg kg-1)	Nrmse
FSTG	834	-4.205	7.222	1.
GAUSS	834	-0.372	1.711	0.282
TERR_DIFF	834	-0.344	2.113	0.335
MD	834	-0.232	1.543	0.271
MD_MT	834	-0.232	1.543	0.271
MD_LSMG	834	-0.631	1.510	0.275

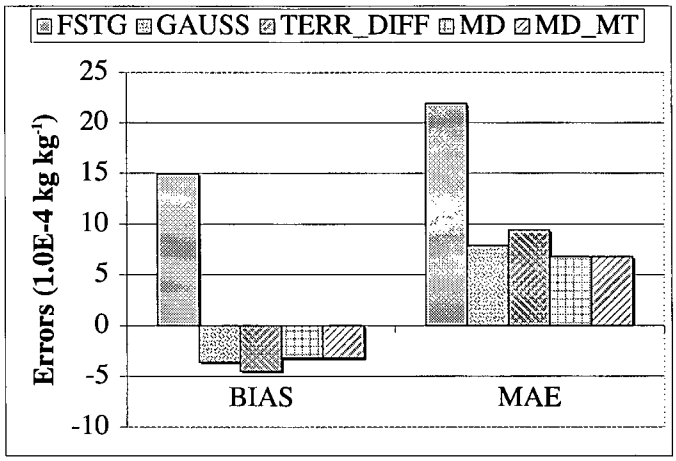

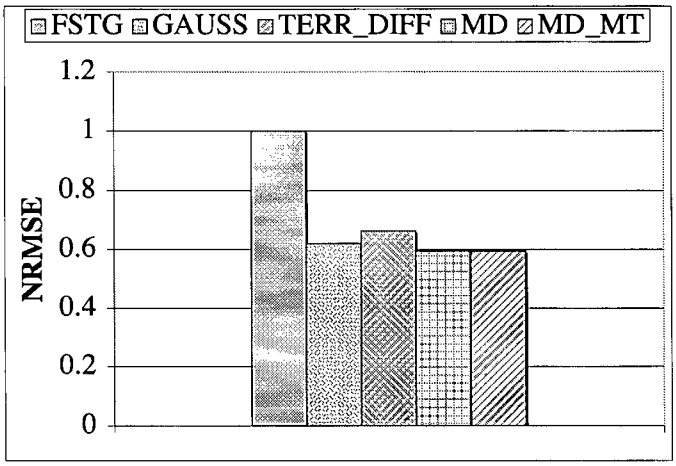

Figure 7.6: Same as Fig. 7.5, but for verification of analyzed specific humidity.

first guess for the month of November are presented in Table 7.3 and Fig. 7.6. The first guess (FSTG) has large negative bias, and large mae. The analysis from each method gives largely reduced magnitude of bias, mae and nrmse compared to the first guess. TERR_DIFF produces slightly smaller magnitude of negative bias but slightly larger mae and nrmse than GAUSS. The MD approaches (MD and MD_MT) produce better analyses with smaller negative-bias magnitude, mae, and nrmse than GAUSS and TERR_DIFF. These findings are the same as for the July 2003 case (Table 6.2). Note the magnitude of the monthly averaged errors is much smaller than that of the errors on a single day in July 2003. As there are no specific humidity observations from mountain-top stations, method MD_MT is equivalent to method MD. Method MD_LSMG gives the smallest mae and nrmse of the specific-humidity analyses, as was also found for potential-temperature analyses.

Similar conclusions can be drawn from the verification statistics of specific humidity analyses for the month of December (Table 7.4). But the magnitude of bias, mae, and nrmse of FSTG in December is correspondingly smaller than that in November. Method MD_LSMG slightly underperforms method MD for the month of December.

7.3 Impacts of data assimilation on subsequent forecasts

As mentioned earlier, daily operational DA forecast runs assimilate temperature and specific humidity observations. The experimental setting for the DA runs is exactly the same as for experiment ATQ during the July 2003 case as described in Chapter 6 (also see Table 6.10). Namely, the final analyses are obtained by combining surface analysis from MD_MT, upper-air analysis, and the first guess by using the scheme PROF; the final analysis increments are incorporated into the MC2 model every 1200 seconds over a 1-h DA window. But the forecast domain and forecast length are different. The MC2 model at 2-km grid spacing is run to make 15 h forecasts that are verified against surface observations and compared with verification statistics from the MC2 CTRL run. Verification results from November and December 2004 are summarized here.

7.3.1 Verification over the full forecast length

This subsection presents the verification summary for different near-surface parameters over the full forecast length from the initial 0 to 15 h forecast period, over all surface stations that reported observations, and over the entire month of November and December 2004, respectively.

Table 7.5 summarizes verification statistics for the month of November. For potential temperature forecasts, the DA run presents slightly larger negative bias than the CTRL run. The magnitude of the biases for both runs are small. The mae and nrmse of the DA run are correspondingly smaller than those of the CTRL run. The monthly averaged improvement in potential temperature forecasts due to data assimilation, as indicated by the value of nrmse, is much smaller compared to the July 2003 case (see experiment ATQ in Table 6.11). A reduction in the improvement of near-surface potential temperature

forecasts due to assimilation of surface observations implies that surface thermal forcing in late Fall may become smaller than in Summer.

Humidity (including relative humidity and specific humidity) forecasts from the DA run are all improved compared to the MC2 CTRL run, in terms of bias, mae, and nrmse. The improvement in humidity forecasts due to data assimilation in November is larger when compared to the July 2003 case (see experiment ATQ in Tables 6.12 and 6.13). The relatively dry July and wet November might help to explain the difference in humidity-forecast performance.

In contrast to the July 2003 case in Chapter 6 (see experiment ATQ in Table 6.11), assimilating temperature and specific humidity does not improve the forecast quality of mean sea-level pressure (SLP) for the month of November. Instead, SLP forecasts from the DA run are verified to be close to those from the CTRL run.

For wind forecasts, root-mean-squared vector error (rmsve) of the DA forecasts is slightly smaller than that of the CTRL forecasts. The nrmsve of the DA forecasts is less than 1.0 but very close to 1.0. This implies that assimilating temperature and specific humidity does not disturb the wind fields very much. This finding is different from the July 2003 case. One reason for the difference in wind-forecast performance may be related to the magnitude of surface potential temperature improvement. When the improvement of surface potential temperature is large (i.e., the July 2003 case), the initial imbalances between mass and wind fields due to a sudden change in temperature fields are also large and can not be removed by the IAU technique. However, when the improvement of surface potential temperature is small (implying that surface thermal forcing introduced by new observations is small), the initial imbalances are also small and can be suppressed when the analysis increments are gradually introduced into the model by the IAU technique.

Verification statistics for the month of December are summarized in Table 7.6. The DA forecast run produces potential temperature, humidity (including relative humidity and specific humidity) forecasts of higher skill than the CTRL run. The improvement in potential temperature for the month of December is slightly larger than that for November, but is much smaller compared to the July 2003 case. The relative humidity forecasts from the DA forecast run are less improved in December than in November.

Similar to the November case, the SLP forecasts are neither improved nor degraded much in the DA run compared to the CTRL run. As can be seen from Table 7.6, the SLP nrmse for the DA forecast run is slightly larger than 1.0 but very close to 1.0. Similar performance is found for vector-wind forecasts in December.

For better view of the DA improvement over CTRL for different near-surface parameters, the nrmses (or nrmsve for vector winds) are also shown in Fig. 7.7.

7.3.2 Verification by forecast hour

Performance of the DA run compared with the CTRL run over the full forecast length from 0 to 15 h for November and December 2004 was examined in the previous subsection. This subsection further evaluates the performance of the DA forecast run by examining the nrmse (for scalars) or nrmsve (for vectors) for each of the forecast hours.

The hourly rmse or rmsve for each forecast variable from the CTRL and DA run were calculated over all the reported surface stations and over the entire month of November

Table 7.5: Verification statistics of near-surface parameters produced by the MC2 control (CTRL) and data-assimilation (DA) runs. The verification parameters include potential temperature, relative humidity, specific humidity, mean sea-level pressure, and vector winds. The statistics are calculated over the 15 h forecast period and for all the observation-forecast pairs over all stations that reported during the month of November. The units for each variable are included for bias and mae (or rmsve). The nrmse or nrmsve is unitless.

		Bias		**Mae**		**Nrmse**	
Variable	**N**	**CTRL**	**DA**	**CTRL**	**DA**	**CTRL**	**DA**
θ (K)	55230	-0.4263	-0.5244	2.2855	2.1596	1.0000	0.9592
RH (%)	31954	-3.2686	-0.7176	10.8270	9.6447	1.0000	0.9117
qv (1.0E-4 kg kg-1)	13290	-5.1481	-3.4751	7.4598	6.3903	1.0000	0.8861
SLP (hPa)	14172	1.2401	1.3159	2.2397	2.2566	1.0000	1.0043

		Rmsve		**Nrmsve**	
Variable	**N**	**CTRL**	**DA**	**CTRL**	**DA**
V (m s-1)	43823	2.6962	2.6925	1.0000	0.9986

Table 7.6: Same as Table 7.5, except for the month of December.

		Bias		Mae		Nrmse	
Variable	**N**	**CTRL**	**DA**	**CTRL**	**DA**	**CTRL**	**DA**
θ (K)	37532	-1.2295	-1.2269	2.7094	2.4955	1.0000	0.9350
RH (%)	21198	2.6845	3.1267	10.6121	10.2724	1.0000	0.9827
qv (1.0E-4 kg kg-1)	10056	-4.0527	-3.5805	7.4361	6.4127	1.0000	0.8875
SLP (hPa)	10878	-0.5464	-0.5475	3.3603	3.3347	1.0000	1.0023

		Rmsve		Nrmsve	
Variable	**N**	**CTRL**	**DA**	**CTRL**	**DA**
V (m s-1)	29961	2.9353	2.9557	1.0000	1.0070

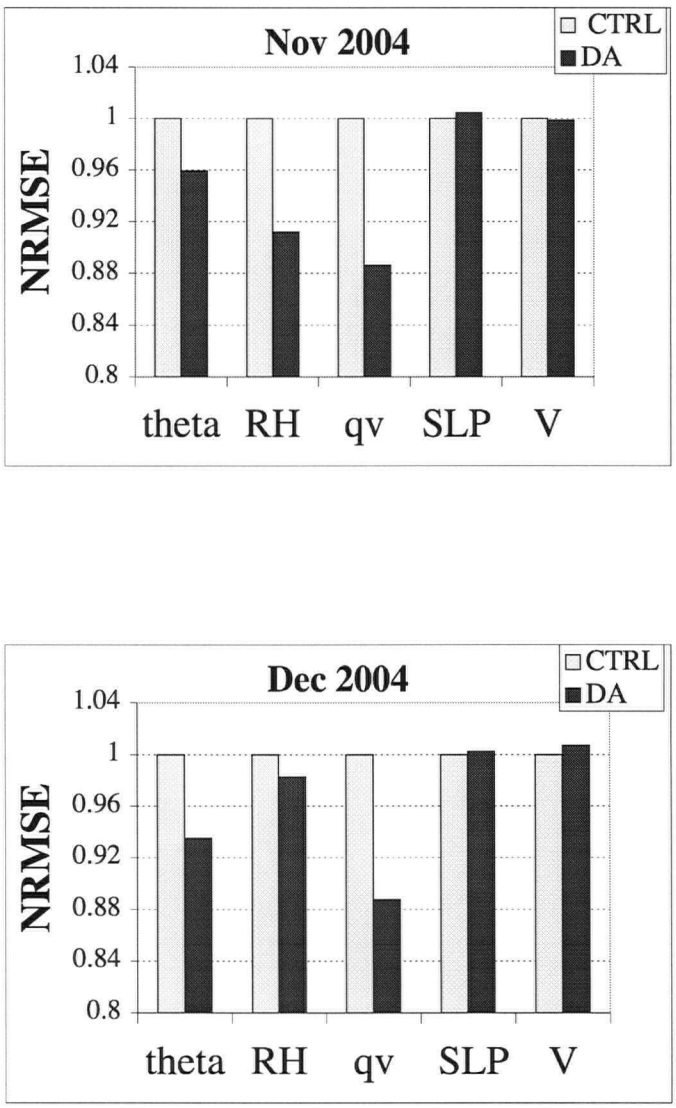

Figure 7.7: The normalized root-mean-square errors (nrmses) of near-surface parameters produced by the MC2 control (CTRL) and data-assimilation (DA) runs. The verification parameters include potential temperature (theta), relative humidity (RH), specific humidity (qv), mean sea-level pressure (SLP), and vector winds (V). The statistics are calculated over the 15 h forecast period and for all the observation-forecast pairs over all stations that reported during the month of: top) November; bottom) December.

and December, respectively. The nrmse (nrmsve) is the rmse (rmsve) of the DA forecast run normalized by the CTRL rmse (rmsve).

Time series of monthly averaged nrmse of surface potential temperature for November is shown in the top panel of Fig. 7.8. A rapid drop in nrmse of the DA run from 1.0 (nrmse of the CTRL run) is apparent at 1 h forecast, as new observation information is introduced into the model within the 1-h DA window using the IAU technique. Then, the nrmse of the DA run increases gradually with forecast hour. At the end of the forecast period (15 h), nrmse is close to 1.0 but still less than 1.0. This implies that the DA forecast at 15 h is still a better match to the observations than the CTRL forecasts. The time series of potential-temperature nrmse for December (see the bottom panel of Fig. 7.8) shows the same pattern as for November, but December has smaller nrmse than November throughout the forecast period.

The improvement of the DA forecasts over the CTRL forecasts decreases with forecast time. These findings are similar to what are found for the July 2003 case. As the verification is carried out for all the surface stations within the forecast domain, the gradual decrease in the improvement (namely increase in the nrmse) of the DA forecasts can be partly attributed to the effects of boundary conditions. Another reason for the decrease in the improvement can be related to the model error that returns after assimilating the observations.

It was demonstrated in section 6.2.1 that assimilating only surface observations but spreading the single-level information upward within the whole BL could result in improved forecasts of near-surface parameters. Even though hourly Eta model analyses are not available, assimilating surface observations for several continuous hours might achieve better forecast quality for a longer forecast period. This could form a part of future work.

The nrmse of surface relative humidity (RH) for November is shown in the top panel of Fig. 7.9. Similar to the performance of the potential temperature forecasts, the nrmse is the smallest at 1 h, and then gradually increases with forecast hours. This means that the improvement in the RH forecasts due to data assimilation is the largest at 1 h, and then gradually decreases with forecast hours. The increase with forecast time in the nrmse of RH for November is correspondingly slower than that in the nrmse of potential temperature. Unlike the RH verification in November, the RH verification in December (see the bottom panel of Fig. 7.9) shows small improvement in the DA forecast at 1 h and gradual decrease in the improvement with time.

The DA forecasts of specific humidity in both November and December are better than the CTRL forecasts (Fig. 7.10). Similar to the potential-temperature forecasts, the nrmse of specific humidity is the smallest at 1 h and then increases gradually with forecast time.

By assimilating temperature and specific humidity only, the model gives slightly degraded SLP and wind forecasts at the first several forecast hours for both November and December (Figs. 7.11 and 7.12). The deviation of the DA wind forecasts from the CTRL wind forecasts for November and December 2004 is much smaller than for the July 2003 case. Near the end of the forecast period, the SLP and wind forecasts from the DA forecast run are very similar to those from the CTRL run. As mentioned in Chapter 6, this could be caused by two factors: part of the assimilated information propagates out of the domain; the mass and wind fields are adjusted to be in balance.

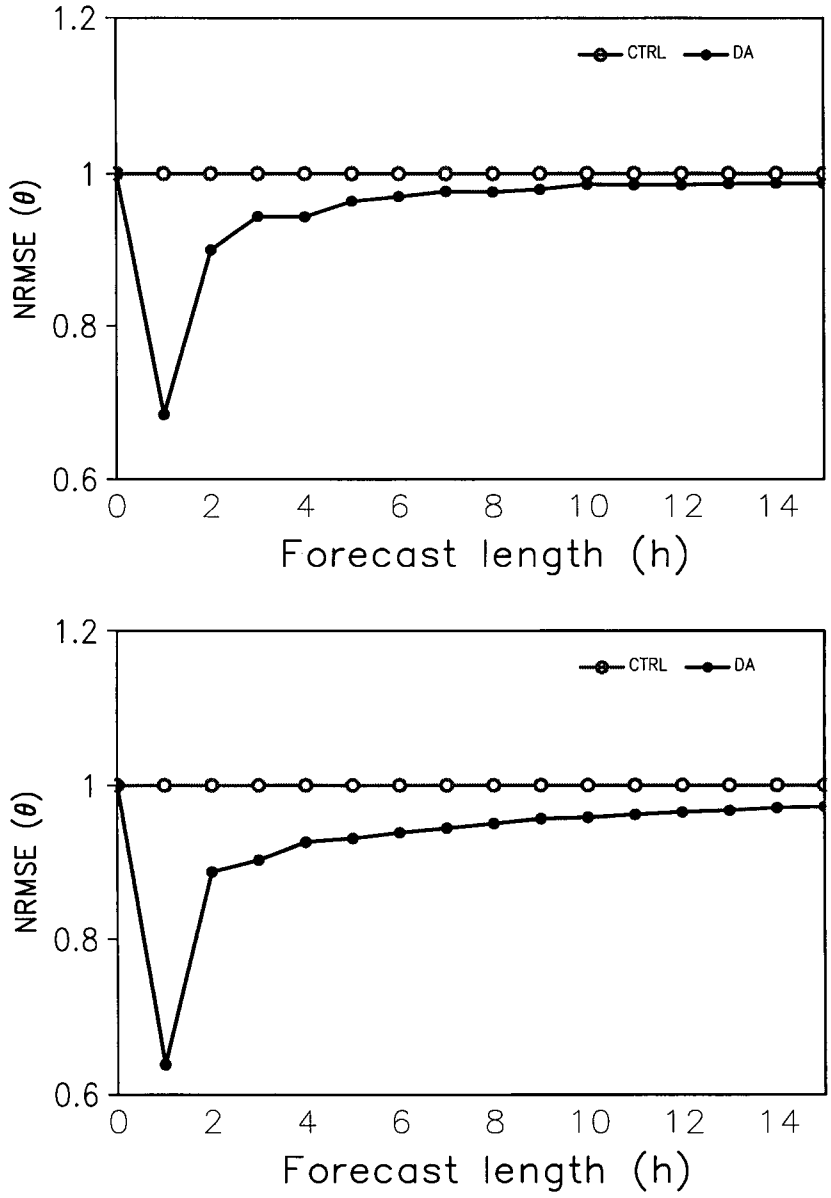

Figure 7.8: Time series of monthly averaged normalized root-mean-square error (nrmse) for surface potential temperature from the CTRL and DA runs: (top) November; (bottom) December.

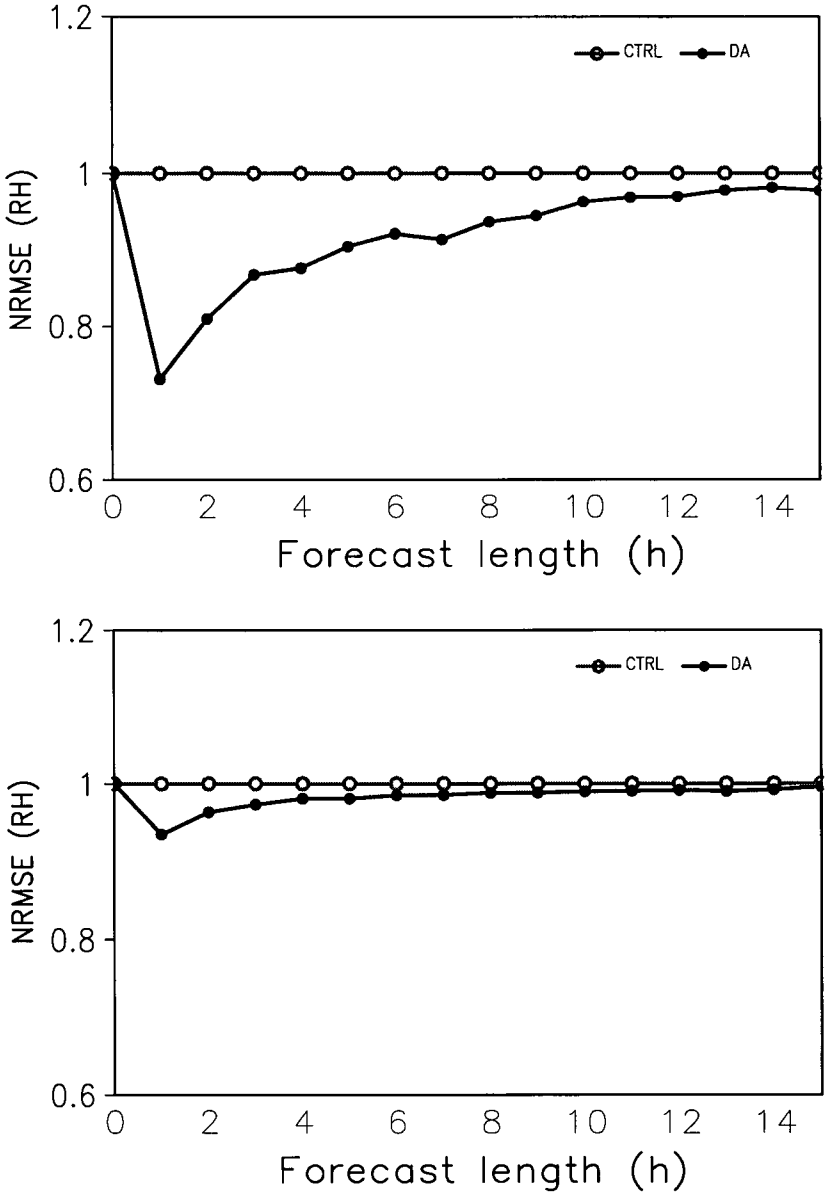

Figure 7.9: Time series of monthly averaged normalized root-mean-square error (nrmse) for surface relative humidity from the CTRL and DA runs: (top) November; (bottom) December.

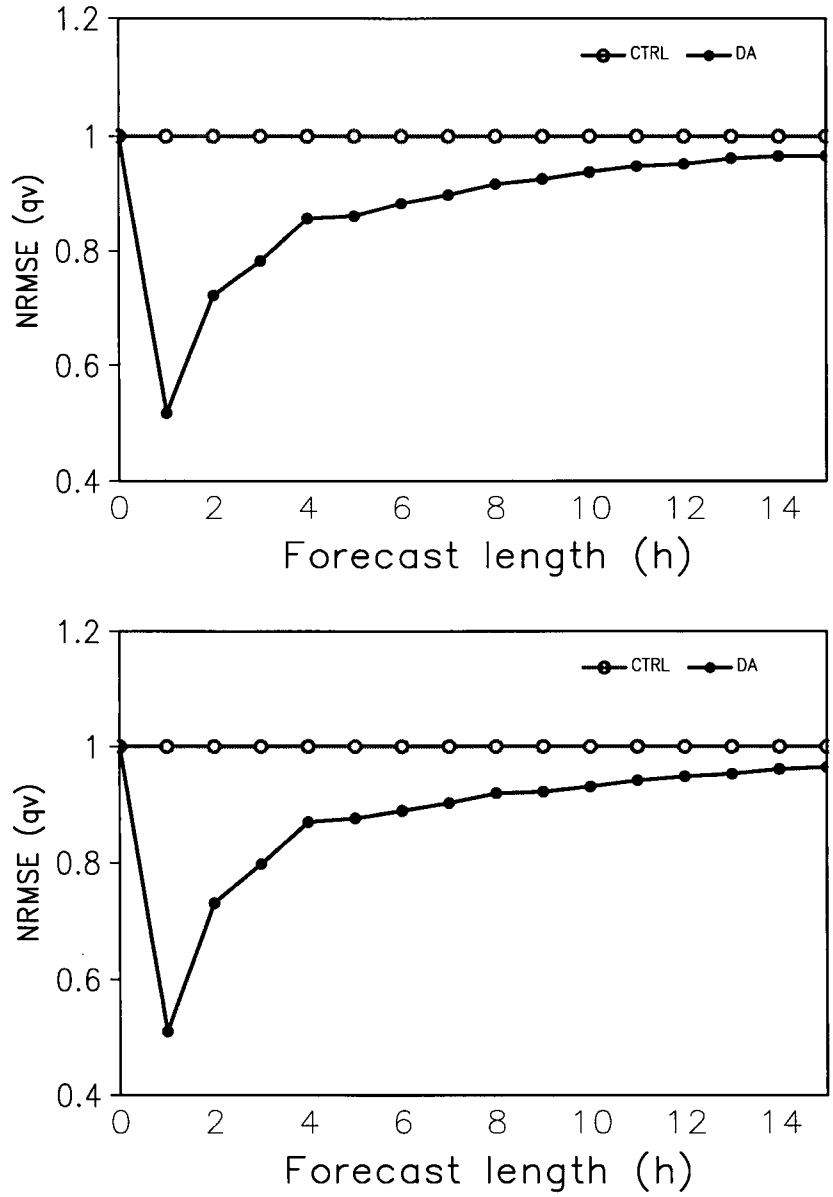

Figure 7.10: Time series of monthly averaged normalized root-mean-square error (nrmse) for surface specific humidity from the CTRL and DA runs: (top) November; (bottom) December.

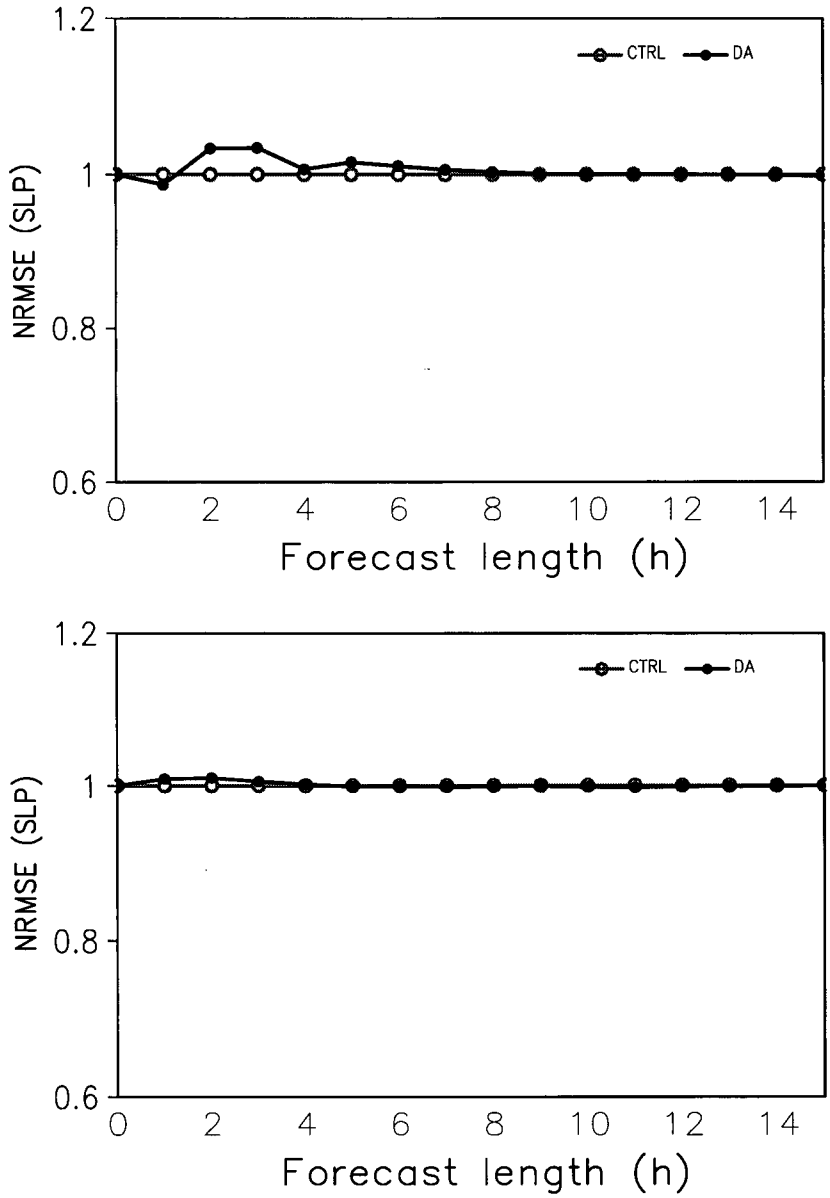

Figure 7.11: Time series of monthly averaged normalized root-mean-square error (nrmse) for mean sea-level pressure from the CTRL and DA runs: (top) November; (bottom) December.

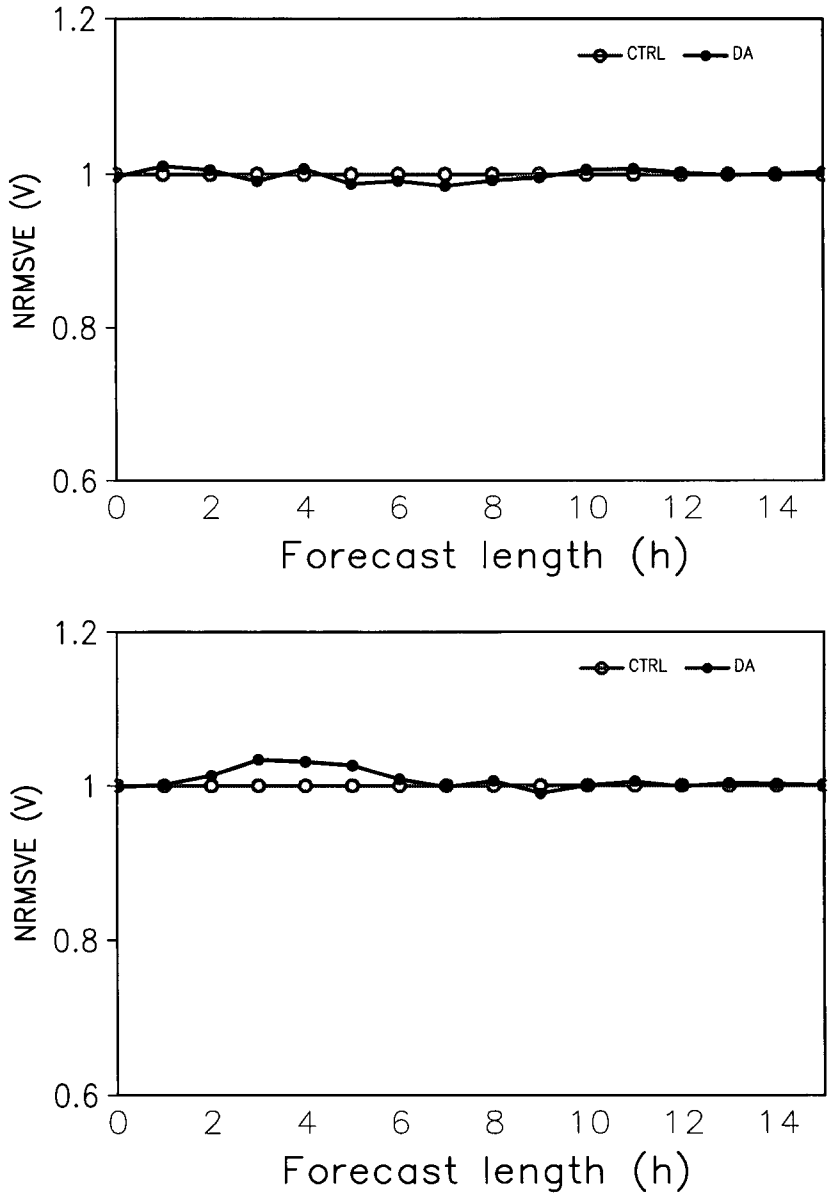

Figure 7.12: Time series of monthly averaged normalized root-mean-square vector error (nrmsve) for surface vector wind from the CTRL and DA runs: (top) November; (bottom) December.

7.4 Summary and conclusions

This chapter presents the verification results of near-real-time, operational data analysis and data-assimilation parallel runs for late Fall and early Winter of November and December 2004. The parameters used in each analysis method are the same as for the case studies in the previous chapters. The analysis results here further confirm that the MD approaches achieve better analysis quality than GAUSS and TERR_DIFF, and that the MD approach after coastline refinement (MD_LSMG) verifies the best. The improvement of the MD approaches over GAUSS and TERR_DIFF and the improvement of MD_LSMG over the original MD approach in November and December are not as large as for case studies in the previous chapters. The case studies are dominated by one flow regime, whereas there are many different flow regimes in November or December.

One uncertainty with the MD approach lies in the specification of the free parameters (a, b, $zref1$, and $zref2$). Fine-tuning of these free parameters over different seasons could produce an analysis that maximizes the gain of applying the MD approach.

The mountain-top refinement introduced into the MD approach did not improve the analyses for the two months studied here compared to the original MD approach, and therefore needs further examination in the future.

The results from the operational DA forecast runs in this chapter confirm that the forecasts improve for the directly assimilated variables, such as temperature and humidity. The improvement of the DA forecast run over the CTRL run is the largest at 1 h, and gradually decreases with forecast time, but lasts until the end of the forecast period (15 h). These findings are similar to what are found for the July 2003 case. In contrast to the July 2003 case, the model tends to produce only slightly degraded SLP and wind forecasts at the first few hours, compared with the forecasts from the CTRL run.

In conclusion, it is confirmed that the MD approach performs better than GAUSS and TERR_DIFF in horizontally spreading surface observations in mountainous regions having circuitous valleys. The coastline refinement introduced into the MD approach helps to produce analyses that better match observations. Compared to the MC2 CTRL run, the parallel MC2 DA forecast run, started from the new analysis obtained by combining surface and upper-air data, produces better forecasts for those near-surface parameters directly assimilated into the model.

Chapter 8

Summary and Discussion

This chapter first summarizes the methodology for analysis and assimilation of surface observations in complex terrain. The key findings related to case studies and near-real-time operational runs are then summarized. Finally, discussion and recommendations for future research are presented.

8.1 Summary of the methodology

Steadily growing computer power allows the resolution of numerical weather prediction (NWP) models to be increased correspondingly. Such resolution is particularly important for mountainous regions like British Columbia (BC). Better use of the available atmospheric data in a high-resolution NWP model is one of crucial factors for improving the quality of model forecasts. The need to improve initial conditions for high-resolution NWP models and the availability of dense, local surface observations in mountainous BC motivate this research.

Assimilating surface observations into a high-resolution NWP model in this thesis involves three major components: horizontal spreading, vertical spreading, and data insertion.

The isotropic assumption typically used in the background error correlation model for horizontally spreading observations is not valid for mountainous terrain. In this dissertation, a technique is developed to create a new anisotropic background error correlation model for use in horizontally spreading surface weather observations in complex terrain with circuitous valleys. The technique is called the mother-daughter (MD) approach and is based on the first-order boundary-layer characteristics in mountainous terrain. In the MD approach, the amount of information transferred from one grid point (the mother) to all neighboring grid points (the daughters) depends on their relative elevation differences. The daughters become mothers and further share information with their neighboring grid points. This iterative method allows valley information to follow valleys around ridges, while reducing spread up over the ridge top. Similarly, this method keeps ridge-top information on the ridge, while suppressing spread down into the valleys.

Two refinements are introduced into the MD approach of horizontal spreading. The first refinement includes an additional factor to account for the land-sea anisotropy. The second refinement is introduced to treat mountain-top observations differently from valley

observations, so that mountain-top information can be spread to neighboring mountain tops.

Regarding vertical spreading, surface observations (and thus surface analyses) are available at only one terrain-following level. Meanwhile, major operational centers generate 3-D meteorological analysis at coarser resolution on a daily basis by assimilating many types of in-situ and remotely sensed measurements. This thesis outlines a method for adding the value of dense local surface observations to the existing 3-D analyses at a coarser resolution. The method assumes that the surface observations are important in describing the atmospheric state vertically within the atmospheric boundary layer (BL), whereas the coarse 3-D analyses from major operational centers are important in providing information for the atmospheric state above the BL. Under these assumptions, two schemes (SIGM and PROF) are proposed to vertically spread the surface information upward to the BL top. In the scheme SIGM, the analysis increments at the lowest model level are assumed to be applied throughout the whole BL. Sigmoidal functions for surface and 3-D analysis increments are designed separately. In the scheme PROF, the analyzed potential temperature and specific humidity at the lowest model level are assumed to be mixed uniformly within the BL, so that the potential temperature and specific humidity analyses at the lowest model level are applied to the whole BL. The BL top for this scheme is determined by using a profile method. Above the BL top, the two schemes use the first guess from a previous high-resolution MC2 forecast and incorporate as pseudo-observational data the 3-D analysis from major operational centers.

Finally, the incremental analysis updating (IAU) is implemented to insert the final analysis increments (the differences between the final analysis and the first guess) into the MC2 model.

8.2 General conclusions

In Chapter 4, the MD approaches were tested and compared with two existing methods using virtual and real observations for mountainous and coastal terrains in southwestern BC. The two existing methods examined include the original method (GAUSS) in the ADAS (ARPS5.0.0 Beta8), and the method (TERR_DIFF) developed by Miller and Benjamin (1992). In Chapter 6, the MD approaches were further tested and compared with GAUSS and TERR_DIFF using real observations for a different domain in mountainous BC. A variety of numerical experiments were carried out to investigate the impacts of assimilating surface observations using different strategies on subsequent forecasts of near-surface parameters. In Chapter 7, the MD approaches (and the methodology of assimilating surface observations) were tested in near-real-time mode over two months. The key findings in this dissertation are summarized here.

- The spatial structure of background error correlations created by the MD approach is anisotropic. The MD approach can better account for both elevation differences and valley differences in the analysis of observation increments over mountainous regions with circuitous valleys than GAUSS and TERR_DIFF.

- The one-time, initial computational cost of the MD approach is more expensive than that of either GAUSS or TERR_DIFF, because of the need to calculate the sharing

factors (SFs). However, for any fixed set of the free parameters, the resulting SFs can be saved as a fixed file, and can be applied unchanged for each day's analysis. The computational cost for the application of the SFs during each day's analysis is similar to that for either GAUSS or TERR_DIFF.

- The MD approach after coastline refinement performs better than the original MD approach in maintaining thermal contrast across coastlines for the case examined. This is further confirmed by the near-real-time operational tests.

- The MD approach after mountain-top refinement (MD_MT) behaves better than the original MD approach (MD) for the cases examined. Based on the results from the near-real-time operational runs, overall performance of MD_MT is found to be similar to that of MD.

- Surface information assimilated at only the lowest model level is soon lost during the forecast. Better skill in predicting near-surface potential temperature than the control (CTRL) forecast is achieved when surface information is spread upward throughout the whole BL.

- Combining the surface and upper-air data gives slightly larger improvement over the CTRL forecast than assimilating only surface data within the whole BL. The skill of subsequent near-surface potential temperature forecasts by applying the two combination schemes is found to be very similar.

- By applying the temperature analysis increments over a 1-h DA window by using the IAU technique rather than all at once, the DA forecast run has better skill in predicting near-surface potential temperatures for the first several forecast hours.

- By assimilating surface temperature and specific humidity, the model improves the forecast quality of near-surface temperature and moisture parameters compared to the CTRL forecast. The improvement of the DA forecast run over the CTRL run is the largest at 1 h, and gradually decreases with forecast hours, but lasts more than 12 hours before becoming close to the CTRL run. However, the DA forecast run tends to give poorer forecasts of near-surface winds, which were not assimilated into the model.

8.3 Discussion

The MD approach was developed under the intravalley and intervalley decorrelation assumptions. Nonetheless, one can imagine scenarios where the observation in one valley might happen to be well correlated with the air state in a neighboring valley. During a fair-weather event with strong solar heating, the BL could be deeper than the mountain-ridge height, allowing turbulence to mix air between the two valleys. Or during strong synoptic forcing, high winds and intense turbulence could inject similar air into both valleys and/or homogenize the air in both. For these situations, running the forecast model AFTER initialization will mix the air in neighboring valleys due to resolved advection and

parameterized turbulence, even if the initialization spreads the observations only within one valley.

The surface winds are not analyzed and assimilated into the MC2 model in this thesis. The MD approach developed in this thesis might not be suitable for the analysis of surface winds in complex terrain, unless the approach is further refined to account for the relationship between valley orientation and observed wind directions. As a result, the sharing factors have to be calculated during each analysis time. Even if the surface winds are successfully analyzed and assimilated, the near-surface wind forecasts started from a new, better wind analyses might not be better than the forecasts without assimilating surface winds due to the current limitation of grid resolution. The surface winds in complex terrain are highly influenced by surrounding landscapes. A grid spacing less than 2 km will be needed.

One uncertainty with the MD approach lies in the specification of the free parameters (a, b, $zref1$, and $zref2$). Sensitivity tests on the MD free parameters were performed for the February 2003 case (see Appendix C). A subset of available observations were analyzed using various values of the free parameters, and the resulted analyses were verified against the remaining observations. The normalized root-mean-square errors (nrmses) are found to be far more sensitive to $zref2$ than to $zref1$, and the nrmse sensitivity to $zref2$ shows a daily-cycle, corresponding to the characteristics of the BL. This implies that one could automate detecting decorrelated weather versus well-mixed events by using observed BL depth (if available) as the value for $zref2$ during daily analyses. Unfortunately, the observations of BL depth are usually not available at most weather stations. The precise estimation of BL depth remains a big problem though. Further experiments will be required to investigate the sensitivities for other times and locales. The optimum values of the free parameters might be dependent on weather, season, and topography.

For GAUSS and TERR_DIFF, a shorter correlation length scale (R_h) could be used to successfully reduce the intervalley spreading from a disconnected neighboring valley (see Appendix C). However, this strategy also reduces the potentially good intravalley spreading. In addition, it might be hard to find a universal R_h in highly variable terrain. The MD approach suppresses intervalley spreading while allowing intravalley spreading over a longer distance. This approach automatically accounts for the elevations of surface stations and analysis grid points.

To use the MD approach in mountainous terrain, fine-resolution NWP models (i.e., $\Delta x < 5$ km) are recommended, for two reasons. First, the SF is a function of the elevations of analysis grid points, thus there is a need to resolve all important ridges and valleys. Second, the quality of the analyses in data-sparse ridges or valleys depends strongly on the quality of the first guess from the NWP models.

The results from the MD approach after coastline refinement might be further improved if the land/sea breeze frontal location is used to define the edges of the land mask, rather than the actual coastline. However, determining the position of a sea/land breeze front increases the complexity, and requires that the SFs be recomputed during every analysis. The case examined and near-real-time operational tests show encouraging results for the proposed approach, even with land-water contrasts fixed at the coastlines. More studies for different seasons can be done to further elaborate the coastline refinement.

The schemes for vertical spreading of surface information proposed in this dissertation are simple but computationally efficient and practical for daily operational applications.

More advanced and costly scheme could use an ensemble Kalman filter method. In a parameterized 1-D planetary boundary layer (PBL) model, Hacker and Snyder (2004) investigated the potential use of the EnKF in vertically spreading the surface observations and found that assimilating surface observations can improve the modeled PBL state.

Even with high-resolution NWP models and accurate initial conditions, mesoscale model forecast errors will remain due to model deficiencies (e.g., poor model physics) and the inherent limit of mesoscale predictability. Improving the mesoscale model physics (e.g., microphysical schemes and boundary-layer parameterizations) and evaluating short-term high-resolution ensembles are next challenges in improving mesoscale NWP.

8.4 Recommendations for future research

The steps in bringing local surface weather observations in mountainous BC into a high-resolution NWP model have been accomplished successfully. The results show positive impacts on subsequent forecasts of near-surface parameters that are directly assimilated into the model. Based on the findings from this dissertation, recommendations for future research are given as follows.

- Fine-tuning of the free parameters in the MD approach over different seasons could produce an analysis that maximizes the gain by using the MD approach. If computational resources are not a concern, one can also re-calculate the sharing factors for the MD approach during the analysis each day using a $zref2$ value that equals the estimated BL depth. Other issues related to further development and application of the MD approach include its sensitivity to the model resolution or to different locales.

- It is demonstrated in section 6.2.1 that assimilating only surface observations but spreading the single-level surface information upward within the whole BL could result in improved forecasts of near-surface parameters. Even though the 3-D Eta model analyses are not available hourly, future work could be done to assimilate hourly surface observations for several continuous hours in order to achieve better quality for a longer forecast.

- Future investigations could include the analysis of surface winds in complex terrain and the incorporation of winds, together with temperature and specific humidity, into the NWP model.

- One could also verify the DA forecasts against observations, and compare the DA forecasts with the CTRL forecasts in three dimensions.

References

Alapaty, K., N. L. Seaman, D. S. Niyogi, and A. F. Hanna, 2001: Assimilating surface data to improve the accuracy of atmospheric boundary layer simulations. *J. Appl. Meteor.*, **40**, 2068–2082.

Arnold, C. P. and C. H. Dey, 1986: Observing systems simulation experiments: Past, present, and future. *Bull. Amer. Meteor. Soc.*, **67**, 687–695.

Asselin, R. A., 1972: Frequency filter for time integrations. *Mon. Wea. Rev.*, **100**, 487–490.

Barnes, S. L., 1964: A technique for maximizing details in numerical weather map analysis. *J. Appl. Meteor.*, **3**, 396–409.

Barwell, B. R. and A. C. Lorenc, 1985: A study of the impact of aircraft wind observations on a large-scale analysis and numerical weather prediction system. *Quart. J. Roy. Meteor. Soc.*, **111**, 103–129.

Benjamin, S. G., 1989: An isentropic mesoα-scale analysis system and its sensitivity to aircraft and surface observations. *Mon. Wea. Rev.*, **117**, 1586–1603.

Benjamin, S. G., K. A. Brewster, R. Brummer, B. F. Jewett, T. W. Schlatter, T. L. Smith, and P. A. Stamus, 1991: An isentropic three-hourly data assimilation system using ACARS aircraft observations. *Mon. Wea. Rev.*, **119**, 888–906.

Benoit, R., J. Cote, and J. Mailhot, 1989: Inclusion of a TKE boundary layer parameterization in the Canadian regional finite element model. *Mon. Wea. Rev.*, **117**, 1726–1750.

Benoit, R., M. Desgagne, P. Pellerin, S. Pellerin, Y. Chartier, and S. Desjardins, 1997: The Canadian MC2: A semi-Lagrangian, semi-implicit wide band atmospheric model suited for fine-scale process studies and simulation. *Mon. Wea. Rev.*, **125**, 2382–2415.

Bergeron, G., R. Laprise, D. Caya, A. Robert, M. Giguere, R. Benoit, and Y. Chartier, 1994: Formulation of Mesoscale Compressible Community (MC2) model. *Internal Report from Cooperative Centre for Research in Mesometeorology*, 165 pp.

Bloom, S. C., L. L. Takacs, A. M. da Silva, and D. Ledvina, 1996: Data assimilation using incremental analysis updates. *Mon. Wea. Rev.*, **124**, 1256–1271.

Bouttier, F., 1993: The dynamics of error covariances in a barotropic model. *Tellus*, **45A**, 408–423.

Bouttier, F. and P. Courtier, 1999: Data assimilation concepts and methods. *ECMWF traning course notes, available at http://www.ecmwf.int/newsevents/training/rcourse_notes/DATA_ASSIMILATION*, 58 pp.

Bratseth, A. M., 1986: Statistical interpolation by means of successive corrections. *Tellus*, **38A**, 439–447.

Brewster, K., 1996: Application of a Bratseth analysis scheme including Doppler radar data. Preprints, *15th Conf. on Weather Analysis and Forecasting*, Boston, MA, Amer. Meteor. Soc., 92–95.

— 2003a: ADAS-ARPS data assimilation using incremental analysis updating. *Available from author*, CAPS/University of Oklahoma, 4 pp.

Brewster, K. A., 2003b: Phase-correcting data assimilation and application to storm-scale numerical weather prediction. Part II: Application to a severe storm outbreak. *Mon. Wea. Rev.*, **131**, 493–507.

CAPS, 1995: ARPS version 4.0 user's guide. Supplement 1: 3-D analysis with ARPS data assimilation system: ADAS version 2.3. Center for Analysis and Prediction of Storms, University of Oklahoma, 100 E. Boyd, Suite 1110, Norman OK 73071 [available at http://www.caps.ou.edu/arps/adas.doc.html].

Case, J. L., J. Manobianco, T. D. Oram, T. Garner, P. F. Blottman, and S. M. Spratt, 2002: Local data integration over east-central Florida using the ARPS Data Analysis System. *Wea. Forecasting*, **17**, 3–26.

Ciliberti, C. M., J. D. Horel, and S. M. Lazarus, 1999: An analysis of a cold frontal passage over complex terrain in northwest Utah. Preprints, *Eighth Conf. on Mesoscale Processes*, Boulder, CO, Amer. Meteor. Soc., 459–462.

— 2000: Sensitivity experiments with a high resolution data assimilation scheme. Preprints, *Ninth Conf. on Mountain Meteorology*, Aspen, CO, Amer. Meteor. Soc., 413–416.

Colle, B. A. and C. F. Mass, 1998: Windstorms along the western side of the Washington Cascade Mountains. Part I: A high-resolution observational and modeling study of the 12 February 1995 event. *Mon. Wea. Rev.*, **126**, 28–52.

— 2000: High-resolution observations and numerical simulations of easterly gap flow through the Strait of Juan de Fuca on 9-10 December 1995. *Mon. Wea. Rev.*, **128**, 2398–2422.

Daley, R., 1991: *Atmospheric data analysis*. Cambridge Atmospheric and Space Science Series, Cambridge University Press, Cambridge, 457 pp.

Davis, C., T. Warner, E. Astling, and J. Bowers, 1999: Development and application of an operational, relocatable, mesogamma-scale weather analysis and forecasting system. *Tellus*, **51A**, 710–727.

De Wekker, S. F. J., M. Kossmann, and F. Fiedler, 1997: Observations of daytime mixed layer depths over mountainous terrain during the TRACT field campaign. *12th AMS Symposium on Boundry Layers and Turbulence*, Vancouver, BC, Canada, Amer. Meteor. Soc., 498–499.

De Wekker, S. F. J., D. G. Steyn, and S. Nyeki, 2004: A comparison of aerosol-layer and convective boundary-layer structure over a mountain range during STAAARTE '97. *Bound.-Layer Meteor.*, **113**, 249–271.

Deardorff, J. W., 1978: Efficient prediction of ground surface temperature and moisture with inclusion of a layer of vegetation. *J. Geophys. Res.*, **83**, 1889–1903.

Delle Monache, L., X. Deng, Y. Zhou, H. Modzelewski, G. Hicks, T. Cannon, R. B. Stull, and C. di Cenzo, 2004a: Air quality ensemble forecast over the Lower Fraser Valley, British Columbia, Canada. *In Proceedings of 27th NATO/CCMS International Technical Meeting on Air Pollution Modelling and its Application*, Oct. 25-29, 2004, Banff, Alberta, 306–309.

— 2004b: Ensemble air quality forecasts over the Lower Fraser Valley, British Columbia: a summer 2004 case study. *In Proceedings of 13th Conference on the Applications of Air Pollution Meteorology with the Air and Waste Management Association*, Aug. 22-26, Vancouver, BC, Amer. Meteor. Soc..

Desroziers, G., 1997: A coordinate change for data assimilation in spherical geometry of frontal structures. *Mon. Wea. Rev.*, **125**, 3030–3038.

Doyle, J. D., 1997: The influence of mesoscale orography on a coastal jet and rainband. *Mon. Wea. Rev.*, **125**, 1465–1488.

Ferrier, B., Y. Lin, D. Parrish, M. Pondeca, E. Rogers, G. Manikin, M. Ek, M. Hart, G. DiMego, K. Mitchell, and H.-Y. Chuang, 2003: Changes to the NCEP Meso Eta Analysis and Forecast System: Modified cloud microphysics, assimilation of GOES cloud-top pressure, assimilation of NEXRAD 88D radial wind velocity data. *NWS Technical Procedures Bulletin [Available at http://wwwt.emc.ncep.noaa.gov/mmb/tpb.spring03/tpb.htm]*.

Fouquart, Y. and B. Bonnel, 1980: Computations of solar heating of the earth's atmosphere: a new parameterization. *Contrib. Atmos. Phys*, **53**, 35–62.

Fritsch, J. M. and C. F. Chappell, 1980: Numerical prediction of convectively driven mesoscale pressure systems. Part I: Convective parameterization. *J. Atmos. Sci.*, **37**, 1722–1733.

Gal-Chen, T. and R. Somerville, 1975: On the use of a coordinate transformation for the solution of the Navier-Stokes equations. *J. Comput. Phys.*, **17(2)**, 209–228.

Garand, L. and J. Mailhot, 1990: The influence of infrared radiation on numerical weather forecasts. Proceedings of *the Seventh Conference on Atmospheric Radiation*, Jul. 23-27, San Francisco, CA, Amer. Meteor. Soc., J146–J151.

Garratt, J. R., J. C. Wyngaard, and R. J. Francey, 1982: Winds in the atmospheric boundary layer - prediction and observation. *J. Atmos. Sci.*, **39**, 1307–1316.

Gauthier, P., P. Courtier, and P. Moll, 1993: Assimilation of simulated wind lidar data with a kalman filter. *Mon. Wea. Rev.*, **121**, 1803–1820.

Hacker, J. and C. Snyder, 2004: Assimilation of fixed screen-height observations in a parameterized PBL. *A community meeting on real-time and retrospective mesoscale objective analysis: An analysis of record summit*, June 29-30, Boulder, CO, USWRP.

Haltiner, G. J. and R. T. Williams, 1980: *Numerical Prediction and Dynamic Meteorology*. John Wiley & Sons, Inc., second edition.

Hessler, G., 1984: Experiments with statistical objective analysis techniques for representing a coastal surface temperature field. *Bound.-Layer Meteor.*, **28**, 375–389.

Hollingsworth, A. and P. Lonnberg, 1986: The statistical structure of short-term forecast errors as determined from radiosonde data. Part I: The wind field. *Tellus*, **38A**, 111–136.

Horel, J., T. Potter, L. Dunn, W. J. Steenburgh, M. Eubank, M. Splitt, and D. J. Onton, 2002: Weather support for the 2002 Winter Olympic and Paralympic Games. *Bull. Amer. Meteor. Soc.*, **83**, 227–240.

Houtekamer, P. L. and H. L. Mitchell, 1998: Data assimilation using an ensemble Kalman filter technique. *Mon. Wea. Rev.*, **126**, 796–811.

— 2001: A sequential ensemble Kalman filter for atmospheric data assimilation. *Mon. Wea. Rev.*, **129**, 123–137.

Ioannidou, L. and M. A. Pedder, 1999: Three-dimensional applications of a successive corrections analysis scheme to mesoscale observations. *Mon. Wea. Rev.*, **127**, 236–251.

Kalnay, E., 2003: *Atmospheric Modeling, Data Assimilation and Predictability*. Cambridge University Press, Cambridge, 341 pp.

Kalthoff, N., H.-J. Binder, M. Kossmann, R. Vogtlin, U. Corsmeier, F. Fiedler, and H. Schlager, 1998: Temporal evolution and spatial variation of the boundary layer over complex terrain. *Atmos. Environ.*, **32**, 1179–1194.

Kossmann, M., R. Vogtlin, U. Corsmeier, B. Vogel, F. Fiedler, H.-J. Binder, N. Kalthoff, and F. Beyrich, 1998: Aspects of the convective boundary layer structure over complex terrain. *Atmos. Environ.*, **32**, 1323–1348.

Krishnamurti, T. N. and L. Bounoua, 1996: *An Introduction to Numerical Weather Prediction Techniques*. CRC Press, 293 pp.

Lanzinger, A. and R. Steinacker, 1990: A fine mesh analysis scheme designed for mountainous terrain. *Meteor. Atmos. Phys.*, **43**, 213–219.

Laprise, R., D. Caya, G. Bergeron, and M. Giguère, 1997: The formulation of the André Robert MC2 (Mesoscale Compressible Community) model. *Atmos.-Ocean Special*, **35**, 195–200.

Laroche, S., P. Gauthier, J. St-James, and J. Morneau, 1999: Implementation of a 3D variational data assimilation system at the Canadian Meteorological Center. Part II: The regional analysis. *Atmos.-Ocean*, **37**, 281–307.

Lazarus, S. M., C. M. Ciliberti, J. D. Horel, and K. Brewster, 2002: Near-real-time applications of a mesoscale analysis system to complex terrain. *Wea. Forecasting*, **17**, 971–1000.

Lenschow, D. H., B. B. Stankov, and L. Mahrt, 1979: The rapid morning boundary-layer transition. *J. Atmos. Sci.*, **36**, 2108–2124.

Liu, H. and M. Xue, 2005: Retrieval of moisture from slant-path water vapor observations of a hypothetical gps network using a three-dimensional variational scheme with anisotropic background error. *Mon. Wea. Rev.*, Conditionally accepted.

Liu, H., M. Xue, R. J. Purser, and D. F. Parrish, 2005: Retrieval of moisture from gps slant-path water vapor observations using 3dvar with recursive filters. Extended abstract, *17th Conf. on Numerical Weather Prediction*, Aug. 1-5, Washington DC, Amer. Meteor. Soc., 14B.6.

Mass, C. F. and Y.-H. Kuo, 1998: Regional real-time numerical weather prediction: Current status and future potential. *Bull. Amer. Meteor. Soc.*, **79**, 253–263.

Mass, C. F., D. Ovens, K. Westrick, and B. A. Colle, 2002: Does increasing horizontal resolution produce more skillful forecasts? *Bull. Amer. Meteor. Soc.*, **83**, 407–430.

McQueen, J. T., R. R. Draxler, and G. D. Rolph, 1995: Influence of grid size and terrain resolution on wind field predictions from an operational mesoscale model. *J. Appl. Meteor.*, **34**, 2166–2181.

Miller, P. A. and S. G. Benjamin, 1992: A system for the hourly assimilation of surface observations in mountainous and flat terrain. *Mon. Wea. Rev.*, **120**, 2342–2359.

Mitchell, H., C. Charette, C. Chouinard, and B. Brasnett, 1990: Revised interpolation statistics for the Canadian data assimilation procedure: their derivation and application. *Mon. Wea. Rev.*, **118**, 1591–1614.

Mitchell, K. E., E. Rogers, D. Parrish, Y. Lin, G. DiMego, M. Ek, D. Lohmann, B. Ferrier, F. Mesinger, P. Shafran, and W. Wu, 2003: Regional Data Assimilation at NCEP: Recent advancements in the assimilation of precipitation, clouds, water vapor, soil moisture and snowpack. *83rd AMS conference on Observing and Understanding the Variability of Water in Weather and Climate*, Feb. 9-13, Long Beach, CA, Amer. Meteor. Soc..

Myrick, D. T., J. D. Horel, and S. M. Lazarus, 2004: Local adjustment of the background error correlation for surface analyses over complex terrain. *Wea. Forecasting*, Accepted.

Nelson, J. A., 1999: The Eta data assimilation. *WR-Tech. Attachment 99-14 [Available at http://www.wrh.noaa.gov/wrh/99TAs/9914/index.html]*.

Parrish, D. and J. Derber, 1992: The National Meteorological Center's spectral statistical interpolation analysis system. *Mon. Wea. Rev.*, **120**, 1747–1763.

Parrish, D., J. Purser, E. Rogers, and Y. Lin, 1996: The regional 3d variational analysis for the Eta model. Preprints, *11th Conf. on Numerical Weather Prediction*, Norfolk, VA, Amer. Meteor. Soc., 454–455.

Purser, R. J., W.-S. Wu, D. F. Parrish, and N. M. Roberts, 2003: Numerical Aspects of the Application of Recursive Filters to Variational Statistical Analysis. Part II: Spatially Inhomogeneous and Anisotropic General Covariances. *Mon. Wea. Rev.*, **131**, 1536–1548.

Rabier, F., H. Jarvinen, E. Klinker, J. F. Mahfouf, and A. Simmons, 2000: The ECMWF operational implementation of four dimensional variational assimilation. Part I: Experimental results with simplified physics. *Quart. J. Roy. Meteor. Soc.*, **126**, 1143–1170.

Rao, P. A., H. E. Fuelberg, and K. K. Droegemeier, 1999: High-resolution modeling of the Cape Canaveral area land-water circulations and associated features. *Mon. Wea. Rev.*, **127**, 1808–1821.

Robert, A. J. and E. Yakimiw, 1986: Identification and elimination of an inflow boundary computational solution in limited area model integrations. *Atmos.-Ocean*, **24**, 369–385.

Roeger, C., R. Stull, D. McClung, J. Hacker, X. Deng, and H. Modzelewski, 2003: Verification of mesoscale numerical weather forecasts in mountainous terrain for application to avalanche prediction. *Wea. Forecasting*, **18**, 1140–1160.

Rogers, E., M. Baldwin, T. Black, K. Brill, F. Chen, G. DiMego, J. Gerrity, G. Manikin, F. Mesinger, K. Mitchell, D. Parrish, and Q. Zhao, 1997: Changes to the NCEP operational "Early" Eta analysis/forecast system. *NWS Technical Procedures Bulletin No. 447, NOAA/NWS, Washington, DC*.

Rogers, E., T. Black, W. Collins, G. Manikin, F. Mesinger, D. Parrish, and G. DiMego, 2000: Changes to the NCEP Meso Eta Analysis and Forecast System : Assimilation of satellite radiances and increase in resolution. *NWS Technical Procedures Bulletin No. 473, NOAA/NWS, Washington, DC*.

Ruggiero, F. H., G. D. Modica, and A. E. Lipton, 2000: Assimilation of satellite imager data and surface observations to improve analysis of circulations forced by cloud shading contrasts. *Mon. Wea. Rev.*, **128**, 434–448.

Ruggiero, F. H., K. D. Sashegyi, A. E. Lipton, R. V. Madala, and S. Raman, 1999: Coupled assimilation of geostationary satellite sounder data into a mesoscale model using the bratseth analysis approach. *Mon. Wea. Rev.*, **127**, 802–821.

Ruggiero, F. H., K. D. Sashegyi, R. V. Madala, and S. Raman, 1996: The use of surface observations in four-dimensional data assimilation using a mesoscale model. *Mon. Wea. Rev.*, **124**, 1018–1033.

Sashegyi, K. D., D. E. Harms, R. V. Madala, and S. Raman, 1993: Application of the Bratseth scheme for the analysis of GALE data using a mesoscale model. *Mon. Wea. Rev.*, **121**, 2331–2350.

Stauffer, D. R., N. L. Seaman, and F. S. Binkowski, 1991: Use of four-dimensional data assimilation in a limited-area mesoscale model. Part II: Effects of data assimilation within the planetary boundary layer. *Mon. Wea. Rev.*, **119**, 734–754.

Stull, R. B., 1988: *An Introduction to Boundary Layer Meteorology*. Kluwer Academic, 666 pp.

— 1992: A theory for mixed-layer-top levelness over irregular topography. Preprints, *the 10th Symposium on Turbulence and Diffusion*, Portland, OR, Amer. Meteor. Soc., 92–94.

— 1993: Review of non-local mixing in turbulent atmospheres: Transilient turbulence theory. *Bound.-Layer Meteor.*, **62**, 21–96.

Stull, R. B.: 1998a, Studies of mountain climates, and a theory for mixed-layer-top levelness over complex topography. Tech. Rep. WFRT-98-001, Geophysical Disaster Computational Fluid Dynamics Center, University of British Columbia, 6339 Stores Rd., Vancouver, BC V6T 1Z4, Canada.

Stull, R. B., 1998b: Transilient turbulence theory: A nonlocal description of convection. *Buoyant Convection in Geophysical Flows*, Kluwer Academic Publishers, 253–264.

— 2000: *Meteorology for Scientists and Engineers,* 2nd ed. Brooks/Cole, 502 pp.

Sundqvist, H., E. Berge, and J. E. Kristjansson, 1989: Condensation and cloud parameterization studies with a mesoscale numerical weather prediction model. *Mon. Wea. Rev.*, **117**, 1641–1657.

Talagrand, O., 1997: Assimilation of observbations, an introduction. *J. Met. Soc. Japan Special Issue 75*, **1B**, 191–209.

Tanguay, M., A. Robert, and R. Laprise, 1990: A semi-implicit semi- lagrangian fully compressible regonal forecast model. *Mon. Wea. Rev.*, **118**, 1970–1980.

Thépaut, J.-N., P. Courtier, G. Belaud, and G. Lemaitre, 1996: Dynamical structure functions in a four-dimensional variational assimilation: A case study. *Quart. J. Roy. Meteor. Soc.*, **122**, 535–561.

Vrhovec, T., 1990: Analysis of mesometeorological temperature fields. *Meteor. Atmos. Phys.*, **43(1 – 4)**, 235–240.

Wilks, D. S., 1995: *Statistical Methods in the Atmospheric Sciences*. Academic Press, 467 pp.

Xue, M., K. Brewster, D. Weber, K. W. Thomas, F. Kong, and E. Kemp, 2002: Real-time storm-scale forecast support for IHOP 2002 at CAPS. Preprints, *15th Conf. on Numerical Weather Prediction and 19th Conf. on Weather Analysis and Forecasting*, Aug. 12-16, San Antonio, TX, Amer. Meteor. Soc..

Xue, M., K. K. Droegemeier, and V. Wong, 2000: The advanced regional prediction system (ARPS) - A multi-scale nonhydrostatic atmospheric simulation and prediction model. Part I: Model dynamics and verification. *Meteor. Atmos. Phys.*, **75**, 161–193.

Xue, M., D.-H. Wang, J.-D. Gao, K. Brewster, and K. K. Droegemeier, 2003: The Advanced Regional Prediction System (ARPS), storm-scale numerical weather prediction and data assimilation. *Meteor. Atmos. Phys.*, **82**, 139–170.

Yakimiw, E. and A. Robert, 1990: Validation experiments for a nested grid-point regional forecast model. *Atmos.-Ocean*, **28**, 466–472.

Yee, S. Y. K. and A. J. Jackson: 1988, Blending of surface and rawinsonde data in mesoscale objective analysis. AFGL Tech. Rep. 88-0144, Air Force Geophysics Laboratory, Hanscom AFB, Massachusetts, 31 pp, [NTIS ADA203984].

Yoo, H.-D., K. K. Droegemeier, K. Brewster, S.-Y. Lee, and C.-H. Cho, 2002a: Impact of Radar data assimilation on the Chorwon-Yonchon 1996 heavy rainfall event: Preliminary results. Preprints, *The 3rd Joint Korea-US Workshop on Storm and Meso-Scale Weather Analysis and Prediction*, 21-22 February 2002, Boulder, Colorado.

— 2002b: Impact of Radar data assimilation on the numerical prediction of heavy rainfall in Korea. Preprints, *19th Conf. on Weather Analysis and Forecasting and 15th Conf. on Numerical Weather Prediction*, Aug. 12-16, San Antonio, TX, Amer. Meteor. Soc..

Appendix A

The Eta analysis

The Eta is NCEP's mesoscale NWP model, which derives its name from its vertical coordinate known as the "eta" or "step-mountain" coordinate. The Eta has been running operationally at NCEP since 1993 (Rogers et al. 1997). Initial analysis was firstly based on optimal interpolation (OI) using a first guess from the Global Data Assimilation System (GDAS). The Eta Data Assimilation System (EDAS), which was run as a 12-h pre-forecast data assimilation with 3-h OI analysis updates, began in October 1995. Since then, the EDAS has been continuously under development. According to Mitchell et al. (2003), several major milestones in the EDAS development included a) replacement of OI analysis with the 3D-Var (Parrish et al. 1996) analysis on 9 February 1998, b) introduction of fully continuous EDAS cycling on 3 June 98, c) assimilation of hourly 4-km radar/gage precipitation analyses on 24 July 2001.

EDAS with 3D-Var assimilates many types of in-situ and remotely-sensed observations, including rawinsondes, dropwinsondes, wind profilers, aircraft winds, satellite cloud-drift winds, ACARS temperature data, surface land temperature/wind/moisture, oceanic surface data (ships and buoys), GOES and TOVS-1B radiance data, SSM/I oceanic surface winds, radar/gage precipitation analyses, VAD wind profiles, NEXRAD 88D radial winds and GOES cloud top pressure, etc (Nelson 1999; Rogers et al. 2000; Ferrier et al. 2003).

As mentioned in section 2.1, the coarsest grid of the MC2 model is directly driven by the Eta model analysis and forecasts. The upper-air information for data assimilation at 3 km (or 2 km) are also extracted as virtual "soundings" from the Eta model analysis (see section 5.1.2). This Eta data is used in this work to generate pseudo upper-air data because it includes the influences from all data sources mentioned above.

The availability of NCEP Eta model output has been restricted to the initial 6-h, and then to 3-h time intervals on grids of degraded resolution by limited Internet bandwidth. Output of polar-stereographic grid "104" with a 90.7-km grid spacing true at 60 °N created from the operational NCEP Eta model forecast are continuously accessible via anonymous ftp in real-time mode. The grid 104 covers a large domain including all of North America and extends west over the Pacific ocean to approximately the date line. The Eta analysis is available on 38 pressure levels from 5.0 to 100.0 kPa every 2.5 kPa.

Effective 25 January 2005, the Eta model has been renamed the North American Mesoscale (NAM) model. This thesis keeps using the name of "Eta" because all numerical experiments performed in this work use the model's analysis/forecast before 25 January 2005.

Appendix B

The Barnes method

The Barnes (1964) scheme is an empirical version of the successive correction method (SCM), as expressed below:

$$f_i^{\nu} = f_i^{\nu-1} + \frac{\sum_{k=1}^{n} w_{ik}(f_k^o - f_k^{\nu-1})}{\sum_{k=1}^{n} w_{ik}} \tag{B.1}$$

where f_i^{ν} is the analysis value at the analysis grid point i, $f_i^{\nu-1}$ is a background field or value of the previous pass at the analysis grid point i, f_k^o is the data value at a data point k, and $f_k^{\nu-1}$ is the estimate of the previous pass at the data point k. The weights w_{ik} are given by an empirical Gaussian function:

$$w_{ik} = exp(-\frac{r_{ik}^2}{R_{\nu}^2}) \tag{B.2}$$

where r_{ik} is the distance between the analysis grid point and the data point, R_{ν} is a parameter determining the shape of the weights. All the data points within a square influence region centered on an analysis grid point are used in this study. The radius of the circle inscribed in the square is five times value of the shape factor (R_{ν}), implying that the lower limit of the weight function being on the order of 10^{-11}. A single pass scheme is used to smooth topography in this work.

Appendix C

Sensitivity Tests

This appendix provides a sensitivity analysis of MD_LSMG (the mother-daughter approach after coastline refinement) to different values of the free parameters for the real-observation case (3-4 February 2003) from section 4.3. The potential-temperature analysis and verification observations remain the same as in Chapter 4. This single case is insufficient to determine the optimal values of the free parameters. However, it does indicate some sensitivity characteristics.

First vary $zref1$ and $zref2$ from 250 to 3000 m every 250 m, while holding $a = 2$ and $b = 2$. Recall that $zref1$ and $zref2$ are the maximum effective BL heights through which surface observations are felt.

Figure C1 shows normalized root-mean-square errors (nrmses) versus $zref1$ and $zref2$ for 0000 UTC (1600 PST) and 1200 UTC (0400 PST) 4 February 2003. At both 0000 UTC and 1200 UTC, nrmses are less than 1.0 for any values of $zref1$ and $zref2$ within the range 250-3000 m. Thus, the analyses agree with the observations better than the first guess. Nrmse is not sensitive to $zref1$ when $zref1 > 750$ m, or $zref2 < 500$ m. This is because the elevation differences between a mother grid point (GP) and its immediate daughter GPs are usually small. Nrmse is far more sensitive to $zref2$ than to $zref1$, as $zref2$ defines the maximum effective height above the observation, and because the elevation differences between the observation and the analysis GPs vary considerably.

Figure C1 shows different features at 0000 and 1200 UTC. In late afternoon (0000 UTC), nrmse shows small sensitivity to $zref1 > 750$ m and $zref2 > 750$ m. In early morning (1200 UTC), lower nrmse is confined to a narrow band from $zref1 = 500$ to 3000 m and from $zref2 = 1000$ to 1250 m. Similar sensitivity tests from 0100 to 1100 UTC indicate a transition at 0200 UTC (not shown). The behaviors correspond to the characteristics of the evolving BL.

Then vary a and b from 0.5 to 4.0 every 0.5 for 1200 UTC 4 February 2003. For these experiments, $zref1 = 2250$ m and $zref2 = 1000$ m, which were the best values from the previous tests. As shown in Fig. C2, $a = 2$ and $b = 2$ (or $a = 1$ and $b = 2.5$) yield lower nrmses.

Using the circuitous travel distance (CTD) in the mother-daughter (MD) approach effectively limits the region of influence in complex terrain (section 4.1). GAUSS and TERR_DIFF ROI (radius of influence) sensitivity tests are performed by varying horizontal correlation length scale R_h (used to calculate ROI in the ADAS) from 100 to 10 km every 10 km for the first and second Bratseth passes. For each test, the third Bratseth pass

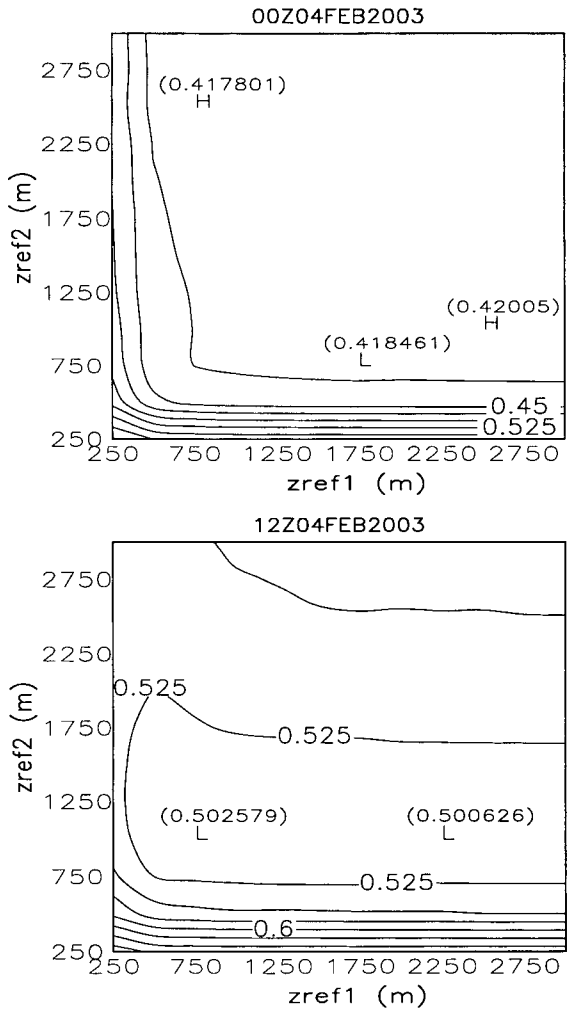

Figure C1: Nrmse of analyses vs $zref1$ and $zref2$ when a=2 and b=2. Contour interval is 0.025 K. (top) Late afternoon (0000 UTC 4 Feb 2003); (bottom) Early morning (1200 UTC 4 Feb 2003). Smaller nrmse is better.

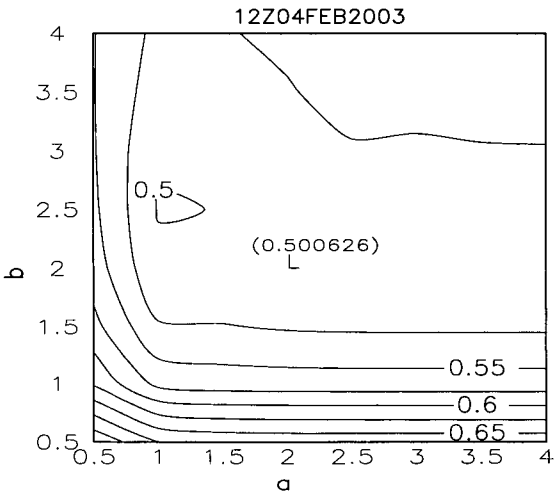

Figure C2: Nrmse of analyses (1200 UTC 4 Feb 2003) vs a and b when $zref1$=2250 m and $zref2$=1000 m, which were the best values for 1200 UTC from Fig. C1. Contour interval is 0.025 K. Smaller nrmse is better.

reduces R_h by 70%, while the fourth and fifth passes reduce R_h by 70% from the third pass.

For the virtual-observation case (see section 4.2.2), rmse decreases rapidly with decreasing R_h for both GAUSS and TERR_DIFF (Fig. C3), as the correction from o1 becomes negligible in the Lillooet River Valley. When R_h = 20 km, a minimal rmse for potential temperature is found to be 0.3385 K for GAUSS and 0.4105 K for TERR_DIFF. The rmse with R_h = 20 km is reduced about 37% for GAUSS and 24% for TERR_DIFF from the first guess. While such small values of R_h successfully reduce intervalley spreading, they do so at the expense of reducing the potentially good intravalley spreading. The MD approach avoids this problem.

Similar tests are performed for the February 2003 real-observation case (see section 4.3). Figure C4 shows nrmses versus R_h used in the first and second Bratseth passes for 1200 UTC 4 February 2003. For both GAUSS and TERR_DIFF, nrmses are less than 1.0. Nrmse shows small sensitivity to R_h when $R_h > 40$ km, while relatively large sensitivity when $R_h < 40$ km. A minimal nrmse is found at R_h = 20 km for GAUSS and at R_h = 10 km for TERR_DIFF. Identical tests are performed for 0000 UTC (Fig. C5). Different from the 1200-UTC results, R_h = 100 or 90 km produces lower nrmses for both GAUSS and TERR_DIFF.

The ROI sensitivity for the February 2003 real-observation case is much smaller than that for the virtual-observation case. This is not surprising, considering only two observations in the two adjacent valleys were used for the virtual-observation case. These results indicate that a prescribed R_h does not work everywhere in highly variable terrain. An R_h that depends on the elevations of surface stations and analysis GPs might help to improve the analyses from GAUSS and TERR_DIFF. In complex terrain, an effective R_h might not only depend on the average station separation, but also on the geographic regions, seasons and weather.

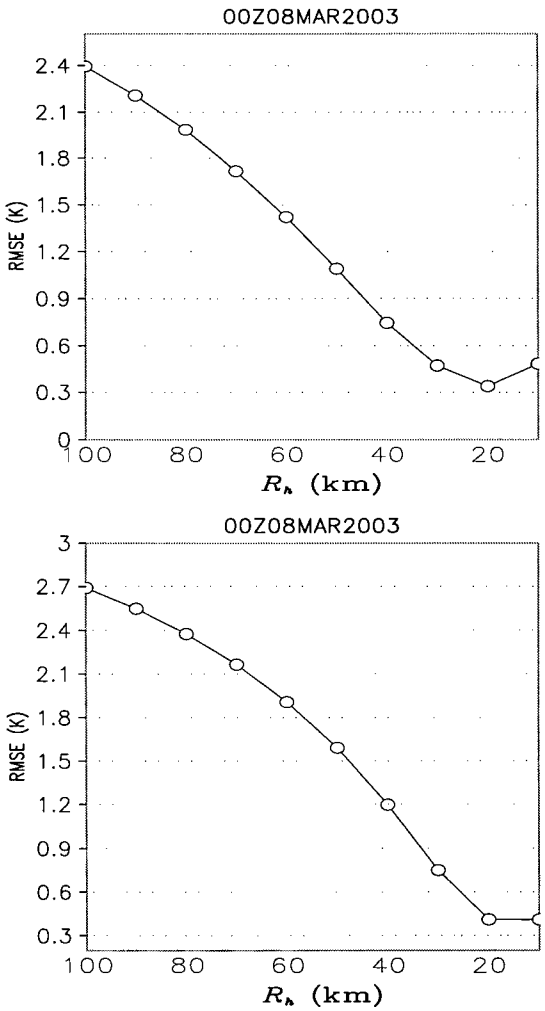

Figure C3: Rmse of analyses (0000 UTC 8 Mar 2003) vs R_h used in the first and second Bratseth passes. The third Bratseth pass has a R_h that is reduced by 70% from the second pass, while the fourth and fifth Bratseth passes have a R_h that is reduced by 70% from the third pass. (top) GAUSS; (bottom) TERR_DIFF. Smaller rmse is better.

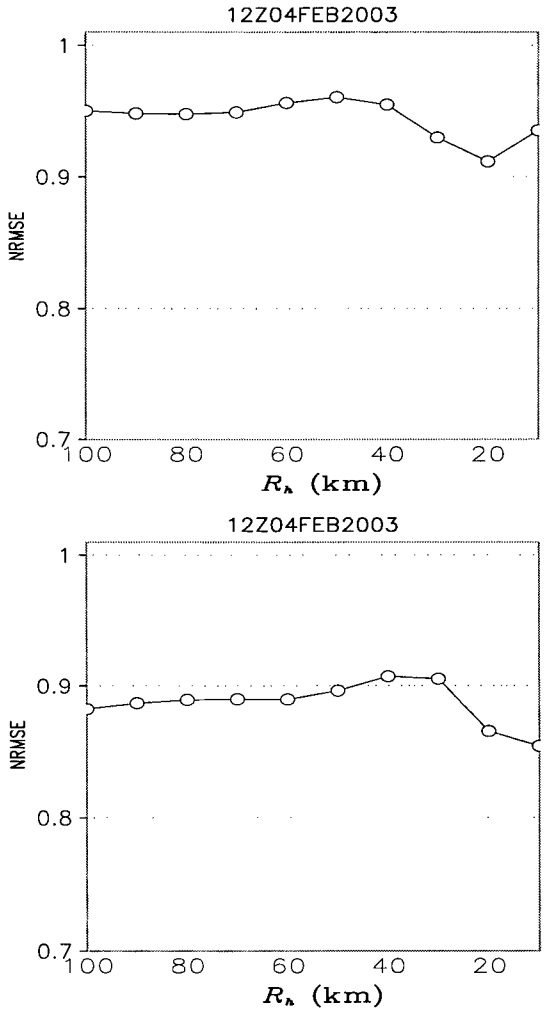

Figure C4: Nrmse of analyses (1200 UTC 4 Feb 2003) vs R_h used in the first and second Bratseth passes. The third Bratseth pass has a R_h that is reduced by 70% from the second pass, while the fourth and fifth Bratseth passes have a R_h that is reduced by 70% from the third pass. (top) GAUSS; (bottom) TERR_DIFF. Smaller nrmse is better.

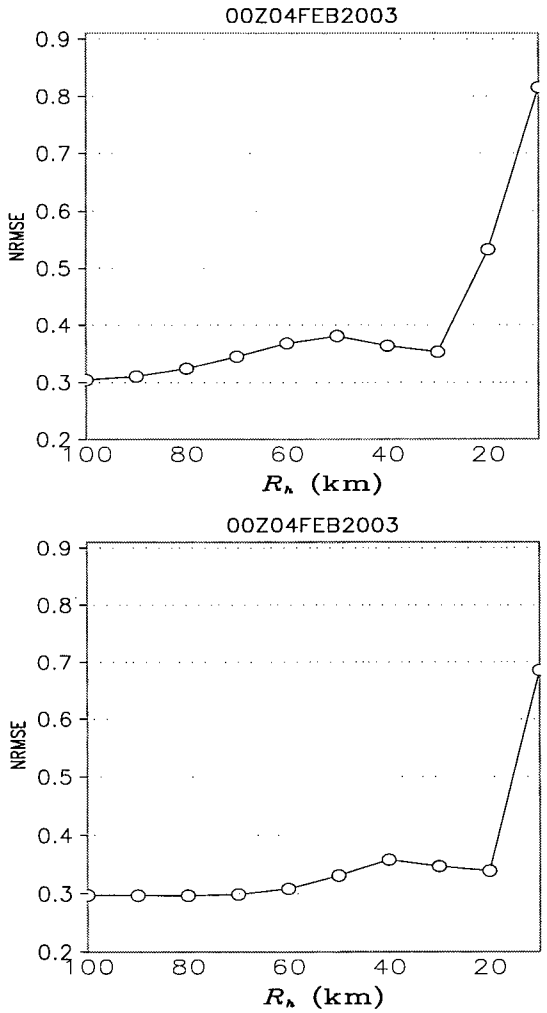

Figure C5: Same as Fig. C4, but for 0000 UTC 4 February 2003. (top) GAUSS; (bottom) TERR_DIFF. Smaller nrmse is better.